UiT
THE ARCTIC UNIVERSITY OF NORWAY

FACULTY OF SCIENCE AND TECHNOLOGY

Department of Geology

An integrated seismic and well data study of shallow fluid accumulations in Snøhvit, SW Barents Sea

—

Andreas Arntzen

EOM-3901 Master`s Thesis in Energy, Climate and Environment

July 2018

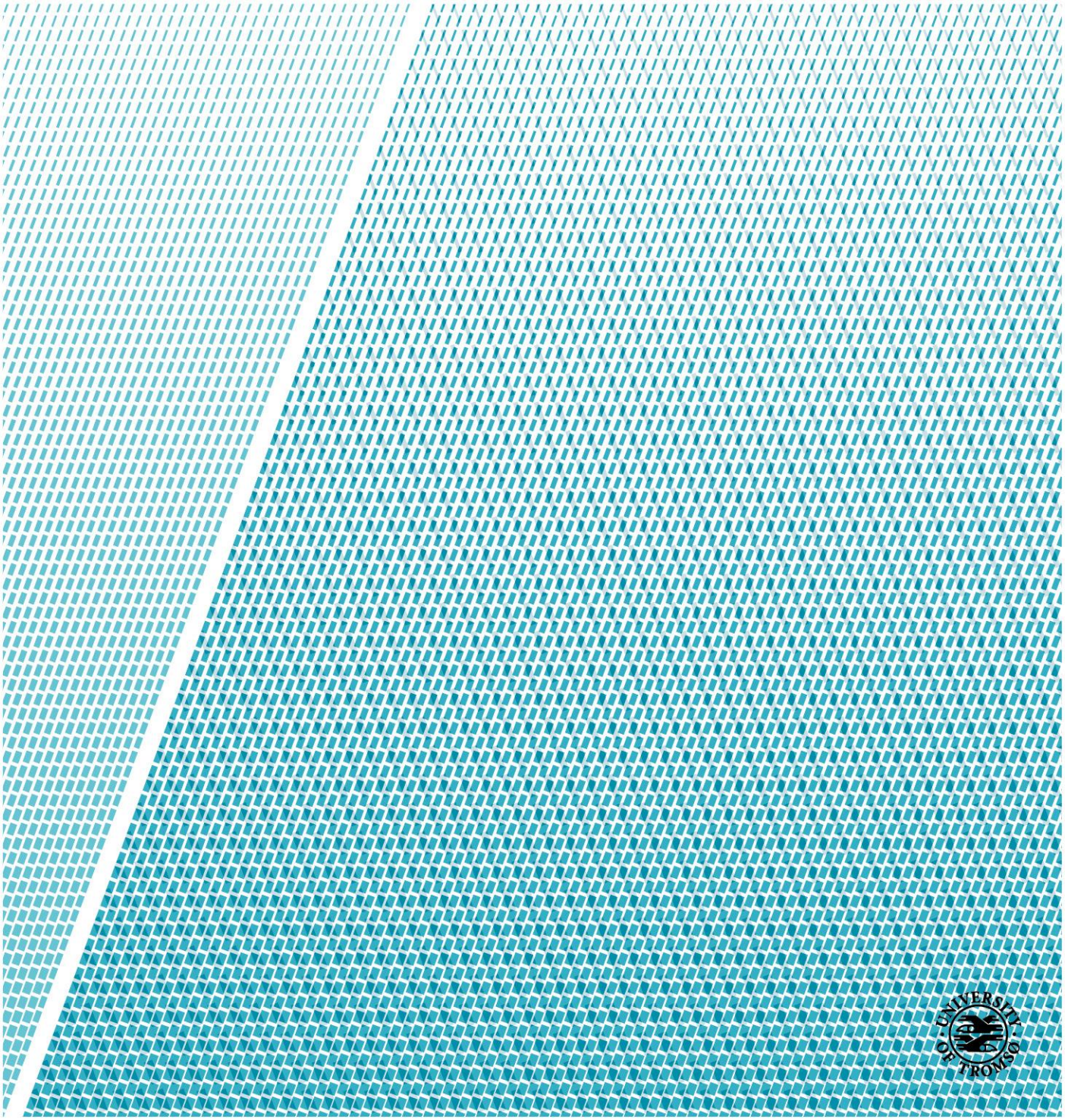

Abstract

In the vicinity of the Snøhvit hydrocarbon reservoir in the Hammerfest Basin a number of fluid flow phenomena occur, e.g. free gas accumulations, pockmarks and potential indicators of gas hydrates.The presence of shallow gas may cause major blowouts during drilling. To reduce the risk, it is important to locate the shallow gas and gas hydrates. CO_2 has been injected into the Snøhvit reservoir since 2008, even though there has been proven leakage from the reservoir. Leakage of CO_2 from the reservoir, through the overburden reaching the seabed is a significant environmental risk. Therefore, it is important obtain a detailed understanding to processes controlling fluid flow, how deep-seated faults can act as conducts for fluid migration, as well as the origin of the shallow gas and gas hydrates located above the reservoir.

Newly released 3D seismic data shows the upper few 100s meters of the overburden at Snøhvit in much more detail than previous known, due to reprocessing. In this thesis the migration mechanisms of fluids are described in detail together with seismic indications of shallow gas and gas hydrates. Further, pockmarks, gas chimneys and high amplitude anomalies were mapped out and discussed in relation to deep seated faults penetrating the reservoir. A conceptual model was carried out explaining the origin of the shallow gas above the Snøhvit field in relation to the geological history in the area and how faults play an important part. It was found that the cycles of glacial loading and unloading during the Cenozoic have caused extensive fracture developments, leading to migration of gas from the reservoir to form shallow accumulations of gas and gas hydrates with suitable pressure and temperature conditions.

A simpe analytical model was used to determine the leak off factor of two faults located close to the F-2 CO2 injector, and to study which parameters might affect the migration of CO2 from the reservoir through a faoult and into overlying sand, thereby explore more about the risk of storing CO_2 in the Snøhvit reservoir today. The leak off factor calculated in this study was found to be very low. The main parameters driving leakage through faults seem to be the reservoir permeability, fault permeability and reservoir thickness. The risk of injection into a low permeable reservoir with an overlaying high permeable sand was highlighted. It is also shown that the fault permeability becomes less important if the overlaying sand has low permeability and hence low flow potential.

The risk of CO_2 leakage can be mitigated with a better understanding of the drive mechanisms of fluid migration and origin of shallow gas and gas hydrates. Monitoring the fluid flow of the injected CO_2 in the reservoir by 4D-seismic is also important together with measurements of the pressures and total volume of the injected CO_2. This is essential for the widespread implementation of carbon capture and storage.

Acknowledgement

Så sitter jeg her da, noen få timer før innlevering av masteroppgaven og formulerer acknowledgement. Det blir litt rart, og ta med tannbørsten og dyna hjem, snakke med folk og tenke på noe annet enn grunn gass og tidsepoker. Prosessen har vært krevende, men også lærerik. Ikke bare det siste semesteret, men hele studieoppholdet.

Det hele startet med en Harstad-basert kollokvie-gruppe på 3, med felles sosial angst. Så jeg starter der, med å takke Andreas og Mats for at dere lærte bort verdifulle egenskaper som prokrastinering, skippertak og kunsten med kontinuasjonseksamen, før dere forlot etter 1.5 år. Å være alene på ei kollokviegruppe var selvsagt enkelt, men jeg skylder likevel resten av klassen en stor takk for hjelp til umulige innleveringer og invitasjoner til sosiale settinger. Det har jeg satt pris på, til tross for en proffkarriere i Fløya som ofte kom i veien, enten i form av dugnad, trening eller buss til Skjervøy eller Alta.

Takk til kontekontoret på rødbrakka, for saklige og mindre saklige diskusjoner, for en perfekt kaffe og for støtte i kantina når den var full av folk.

Så til familien, som har gjort en til dels krevende studiehverdag mye enklere. Takk til Marit som det siste året har stilt opp som den studievennen jeg har manglet siden kollokviegruppa gikk i oppløsning. Og til Kristine for å være et forbilde og en stor inspirasjon for å stå løpet ut. Takk til mamma og pappa for at jeg alltid kan komme til dere hvis det er noe, og for ordtaket: «Det er viktigere å vise god karakter, enn å ha gode karakterer».

Til slutt vil jeg takke veileder Andreia for at du tok på deg denne umulige oppgaven, og for at du hjalp meg til et sluttresultat jeg kan være stolt over.

Andreas
Tromsø, Juli 2018

Table of Contents

1 Introduction

1.1 Objective

Around the petroleum fields in the Hammerfest Basin located southwest in the Barents Sea **(Figure 1-1),** a number of fluid flow phenomena appear. Migration of hydrocarbons in the subsurface leaves imprints in the seismic, such as pockmarks (Alan Judd et al., 2007; Rise et al., 2015), amplitude anomalies (Løseth et al., 2009), seismic pipes and gas chimneys (Løseth et al., 2009; Vadakkepuliyambatta et al., 2013). Due to newly released 3D seismic data covering the overburden of the deep reservoir, these indicators of shallow gas accumulations and possible gas hydrates can be observed in much more detail than before. In this study, any distinct amplitude feature above the Kolmule formation will be investigated as a potential shallow gas accumulation.

The focus of this master thesis is to map and interpret fluid flow features observed in the seismic data above the Snøhvit field. The objective is to provide a better understanding of the processes controlling fluid flow, the provenance of the gas and the interplay between shallow fluid accumulations and deep hydrocarbon reservoirs.

Providing knowledge about the geological events that took place in the SW Barents Sea and the relation between glacial events and the complex petroleum systems in the area, has also been focused on. Previous studies show that the hydrocarbons in the Barents Sea has been strongly influenced by periods of uplift and erosion during Cenozoic times, associated with the tectonic opening of the Norwegian-Greenland Sea and the many glacial events in the same period (Dimakisa et al., 1998; Dorè et al., 1996).

Uplift and erosion has been assumed to cause leakage and migration of hydrocarbons from proven reservoirs into shallower sediments, accumulated as shallow gas (Tasianas et al., 2016), trapped as gas-hydrates with right pressure and temperature conditions (Duran et al., 2013a) or even spilled into the ocean through the seabed with possible formation of pockmarks (Duran et al., 2013b).

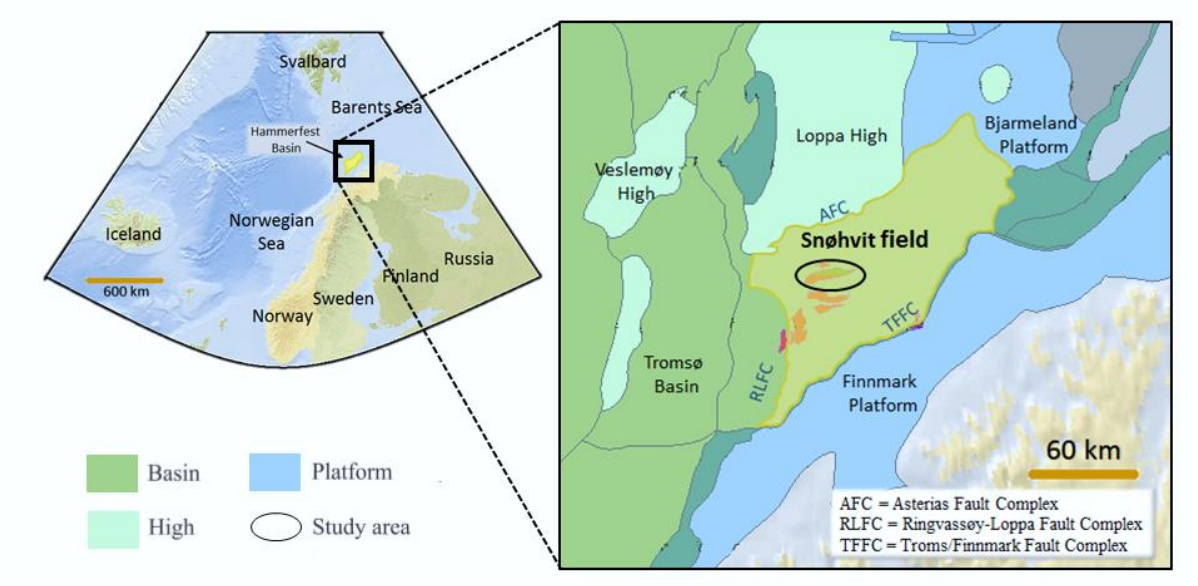

Figure 1-1 Study area in the southwestern Barents Sea. Location of the Hammerfest Basin (black square), with a closer view of the petroleum fields within the basin. Modified from (NPD, 2017).

1.2 Motivation

Deeper understanding of the generation and migration history of shallow gas and gas hydrates, to predict where it is located, is necessary for many reasons. Most important, occurrence of shallow gas and gas hydrates can pose a potential hazard during drilling exploration, providing constrains for basin modelling. Drilling from offshore rigs into accumulations of hydrocarbon pockets may cause major blowouts due to pressure conditions (Andreassen et al., 2007; Davis, 1992; Kanestrøm et al., 1990; Schroot et al., 2003; Sills et al., 1992). The ability to map the prevalence of shallow gas and gas hydrates in high detail is crucial in order to reduce the risk of drilling. In addition, seeping gas into the ocean has been discussed to have a potential impact on benthic and marine ecosystems, as well as being a contributor to climate change (Davis, 1992; J. Hansen et al., 2000; M Hovland et al., 1988).

From a more commercial point of view, the presence of shallow gas may also indicate a functioning petroleum system in the actual area, with deeper and larger hydrocarbon reserves (Andreassen et al., 2007; Schroot et al., 2003). The recent consideration of shallow gas accumulations as a future economical resource (e.g. Peon gas field) (Carstens, 2005) also contributes to the importance of subsurface fluid flow investigation.

In |addition, the understanding of depleted hydrocarbon fields with reliable trapping mechanisms is also gaining worldwide attention, due to the potential of carbon dioxide capture and storage (CCS) (Benson et al., 2008; Herzog et al., 2004; Metz, 2005; Steeneveldt et al., 2006). This technique comprises the separation and entrapment of CO_2 from industrial processes and the injection into geological reservoirs, keeping it away from the atmosphere for a considerable amount of time. Knowing that over 60 % of the global CO_2 emissions potentially can be stored in the subsurface (Benson et al., 2008), this process is a great contributor to reduce the emissions of anthropogenic greenhouse gases (GHS) (Herzog et al., 2004).

CO_2 has been injected into the Snøhvit reservoir since 2008 (O. Hansen et al., 2011), despite the fact that there has been proven leakage from the reservoir (Tasianas et al., 2016). Leakage of CO_2 from the reservoir through the overburden, reaching the seabed is a significant environmental risk. Therefore, it is important to get a detailed understanding of the processes controlling fluid flow, how deep-seated faults can act as conducts for fluid migration and the origin of the shallow gas located above the reservoir.

2 Theoretical framework

2.1 Physical principles related to fluid flow

2.1.1 Porosity and permeability

The flow of subsurface fluids is strongly related to the percentage or fraction of open space within sediments, termed porosity (ϕ). This is further divided in two subgroups, classified as primary and secondary porosity. Warren et al. (1963) define the former as the porosity at deposition and lithification, and the latter as the porosity occurring after the sediments have gone through physical and chemical processes during compaction and burial. Normally, the porosity decreases with increasing depth as the rock gets more compacted and cemented (Schmidt et al., 1979). Also, the connection between the pores in porous sediments are required for transmitting fluids, determined by the permeability (Berndt, 2005). That means, fluid flow through subsurface media is depending on rock properties and sufficient connected pore space to allow fluid flow at different pressures. The permeability is primarily a function of grain size and sorting, the same variables influencing porosity (Beard et al., 1973). Even though the permeability is strongly correlated to porosity, highly porous rocks can have little or no permeability.

2.1.2 Darcy's law

Henry Darcy formulated in 1856 the law that describes the behavior of fluid that flow through a porous media (Hubbert, 1940). The equation includes the permeability of the medium, the pressure gradient and the viscosity of the fluid **(Figure 2-1)** and is named after Darcy himself.

$$Q = -\frac{kA\,(P_b - P_a)}{\mu L} \qquad \textbf{(Equation 2-1)}$$

Q is total discharge (m^3/s), k is the permeability (m^2), A is the cross-sectional area (m^2), $Pb-Pa$ is the pressure difference (Pa), μ is the viscosity of the fluid (Pa·s) and L (m) the distance where the pressure change take place.

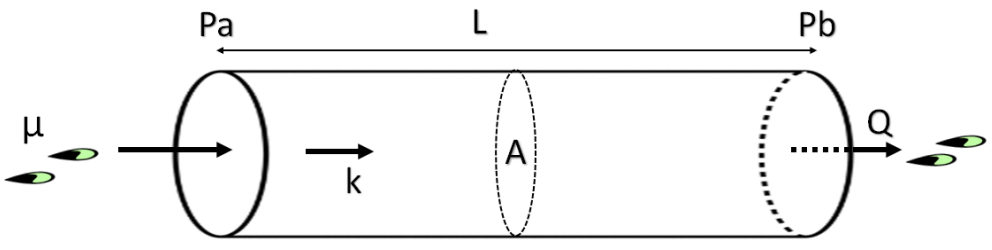

Figure 2-1 Illustration of all the parameters included in Darcy's law, modified after description from (Hubbert, 1956).

The migration of fluids is pressure related, driven by the pressure gradient from areas with high pressure to areas with lower pressure, indicated with the negative sign in **Equation 2.1.** The permeability is a function of the material type, and the fluid viscosity controls how the fluid responds to the change in pressure (Selley et al., 2015). Darcy's equation is valid when the pore space is filled with only one fluid phase and when there is no chemical reactions between the grains and the fluid (Berndt, 2005). The formula indicates that fluid flow favors a short migration pathway with high permeability and large pressure difference. It also shows that a low viscous fluid flow easier than one with high viscosity (Selley et al., 2015).

2.1.3 Capillary pressure

Fluids in the subsurface are in many cases a mixture of many compounds. Consequently, they respond differently to temperature and pressure, and the flow of fluids are not only constrained by Darcy's law, but also by the fluids ability to exceed the capillary entry pressure, given by;

$$P_C = \frac{2i\cos\theta}{r} \qquad \textbf{(Equation 2-2)}$$

i = Interfacial tension of the liquid, θ = angle of contact between the fluids and the capillary tube and r = radius of the interface

2.1.4 Pressure

Describing the general pressure resulting from rock overburden in the crust is strongly related to the hydrostatic or lithostatic model in an area. The hydrostatic pressure is the pressure experienced by any fluids at rest in a continuous fluid-column. The pressure gradient is connected to the compaction history, increasing the pressure as new sediments accumulate on top. This causes compacted material with reduced porosity and permeability, and the pore pressure will equal the hydrostatic pressure if the permeability allow sufficient flow during compaction (Berndt, 2005).

$$P = pgh + P_a \qquad \textbf{(Equation 2-3)}$$

P = pore pressure (bar), p = density of pore water (kg/m^3), g = gravitational constant (9.81 m/s^2), h = height of fluid column (m), P_a = atmospheric pressure (1 atm)

Lithostatic pressure together with pore fluid pressure will affect how the sediments respond to compaction in terms of diagenetic properties of the rock (Berndt, 2005). When the pressure surpass the hydrostatic pressure, the fluids become over-pressured **(Figure 2-2),** which is common in the subsurface where fluids have been trapped in the pore spaces during burial (Berndt, 2005). To obtain hydrostatic pressure, the pressure must be high enough to fracture the rock, and release the over-pressure.

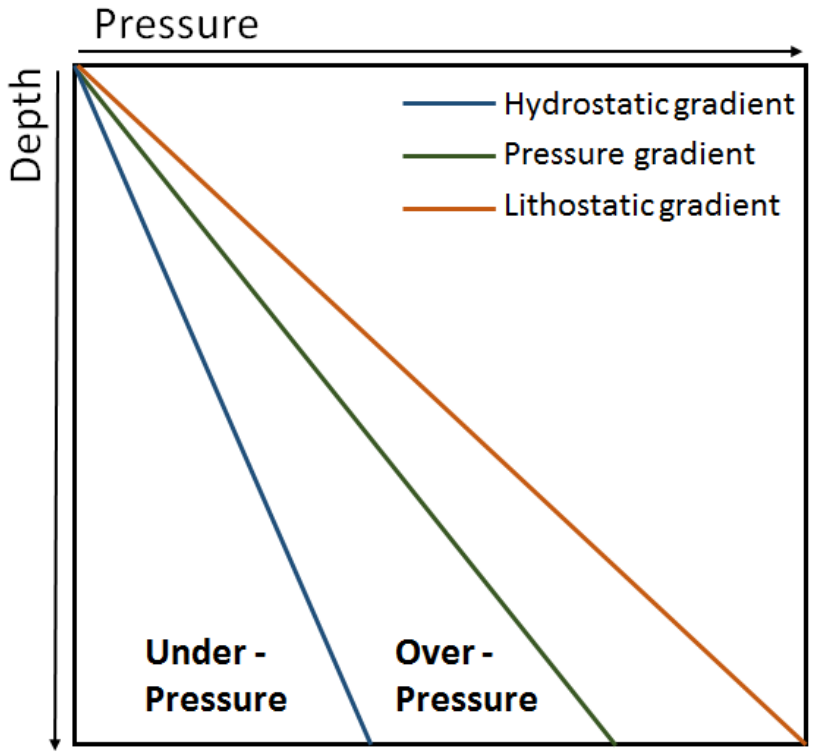

Figure 2-2 Schematic diagram illustrating how different pressure gradients increase during burial. The pressure relation under or above the hydrostatic pressure are associated with under-pressure and over-pressure respectively. Modified from (Moore, 1989)

2.2 Petroleum systems

Since the early 70s, the concept of petroleum systems has been discussed by several geologists (Demaison et al., 1991; Dow, 1974; Magoon, 1988; Alain Perrodon, 1983; A Perrodon, 1992), trying to understand the mechanisms of hydrocarbon generation, migration and accumulation. According to Magoon (1988), a petroleum system combines all the geological aspects and processes that are necessary for the existence of oil and gas deposits in nature. These elements are described in this section and include a mature, organic-rich source rock, expulsion and secondary migration, high-quality reservoir and a functioning trapping mechanism (Magoon et al., 1999). To obtain a petroleum system that works, all these elements must occur relative to each other in time and space (Magoon, 1988; Magoon et al., 1994)

2.2.1 Generation of hydrocarbons

The origin of hydrocarbons in the subsurface is mainly microbial or thermogenic, both being derived from the decomposition of organic matter in anoxic environments (Buller et al., 2005; Claypool et al., 1974; Davis, 1992; Earle, 2015; Floodgate et al., 1992; Rice et al., 1981). As organic material rarely makes it through the tough, high-energy environment associated with deposition of coarse material, the formation of gas occurs in fine-grained source rocks (Floodgate et al., 1992). Due to chemical reactions, only molecules from hydrogen and carbon survive, thereby the name: hydrocarbons.

Microbial and thermogenic gas are referred to as biogenic processes, and make up the largest portion of commercial gas both worldwide and in this study area. Gas produced by chemical reactions from inorganic mantel materials is identified as abiotic gas (Apps et al., 1993; Etiope et al., 2013; Jenden et al., 1993) and will not be discussed further in this thesis. There are several types of gas in the subsurface, but the only gas thought to have a profitable quantity is methane, CH_4 (Davis, 1992; Floodgate et al., 1992). The biogenic generation of hydrocarbons occurs at different depths, with different temperature and pressure conditions **(Figure 2-3).** Microbial methane is generated from microbial (bacteria and ache) degradation of organic matter in shallow sediments during the early stages of diagenesis (Rice et al., 1981; Tissot et al., 1984). The thermogenic methane originates from deeper source rocks with higher temperatures (Davis, 1992; Floodgate et al., 1992). As the depth of burial increases with time, the organic-rich source rock matures, augmenting the possibility of hydrocarbon generation (Floodgate et al., 1992). The evolution of this maturation is subdivided into three stages, classified as diagenesis, catagenesis and metagenesis (Rice et al., 1981) **(Figure 2-3).** Temperatures between 60-120º are known as the "golden zone", being the optimum zone for petroleum generation (Buller et al., 2005; Nadeau, 2011) **(Figure 2-3).** Although these types of biogenic methane are formed at different depths, both types of gas may be found within the shallow gas interval, due to sedimentation and migration (Davis, 1992; Floodgate et al., 1992).

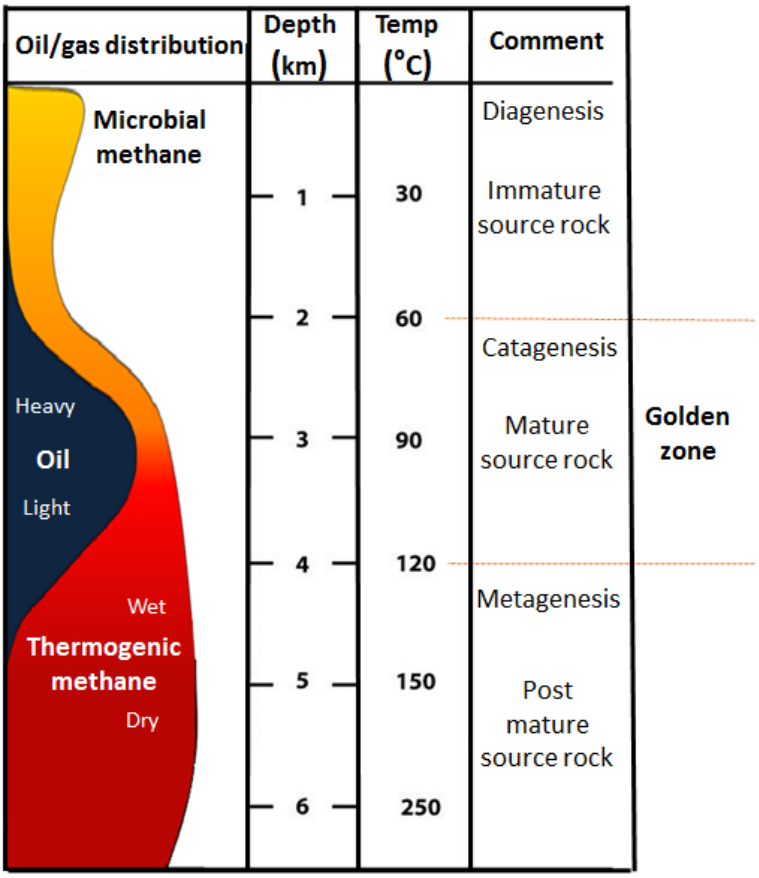

Figure 2-3 Different temperature conditions for microbial gas, oil and thermogenic gas. Modified from: (Earle, 2015; Alain Perrodon, 1983; Rice et al., 1981)

2.2.2 Migration mechanisms

The mechanisms of hydrocarbon migration can be very complex, but briefly explained, these are the movement of fluids in the subsurface. There are three main types of migration, termed primary, secondary and tertiary migration (Bjørlykke, 2010; Floodgate et al., 1992; Gussow, 1954; Peters et al., 2012; Schowalter, 1979; Tissot et al., 1984).

Gussow (1954) defines primary migration as "the expulsion of petroleum from a source rock into adjacent rocks" **(Figure 2-4).** The hydrocarbons migrate through dense, impermeable source rocks with low porosity (e.g. clay or shale), into neighboring rocks being permeable carrier beds, e.g. sandstones or limestone. This is a complex process, including the interactions between water, petroleum and rock matrix.

Secondary migration is understood as the subsequent flow of hydrocarbons within these porous and more permeable rock units (Schowalter, 1979) **(Figure 2-4).** The driving mechanism for secondary migration are buoyancy, capillary pressure and hydrodynamics (Schowalter, 1979). Buoyancy, the main process, is associated with the relation between the density of hydrocarbons and water (Tissot et al., 1984). The greater the density differences, the greater the buoyancy force (Hindle, 1997). Capillary pressure **(2.1.3),** acting as a resistance force (Schowalter, 1979), increases with decreasing pore-throat size, and migration is restrained if the capillary pressure exceeds the buoyancy (Hindle, 1997). Hydrodynamics is controlled by the two opposing forces mentioned above (England et al., 1987), but is by some categorized as less important (Pegaz-Fiornet et al., 2012).

Tertiary migration occurs if the hydrocarbons escape from the trap and remigrate through seepage or leakage due to faulting or fracturing (Tissot et al., 1984) **(Figure 2-4).**

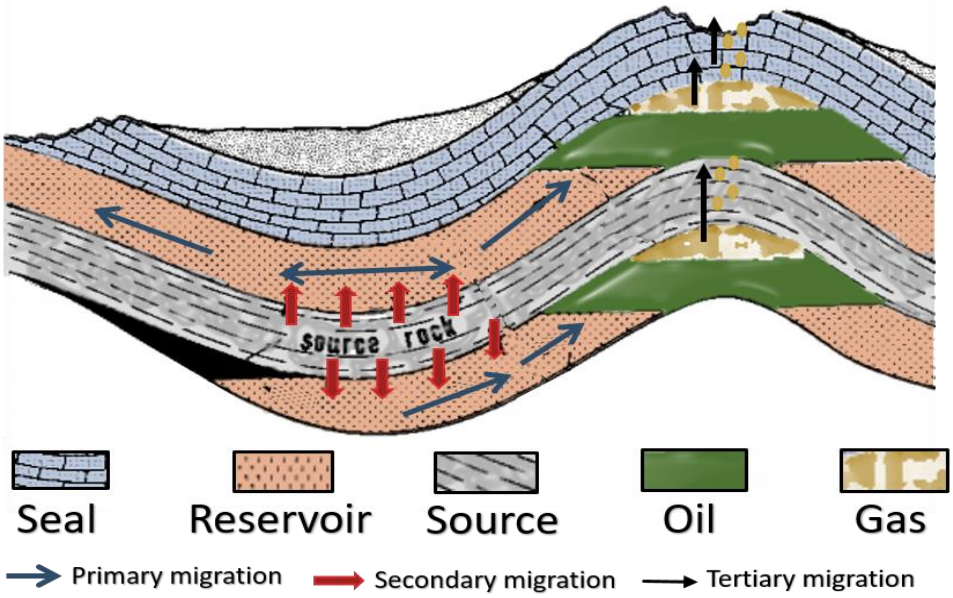

Figure 2-4 Primary, secondary and primary migration of petroleum from dense source rock, into permeable carrier beds ending in accumulation of oil and gas in a structural, anticline trap with leakage. Modified from (Tissot et al., 1984)

The hydrocarbons might leak through the edge of the reservoir (named spill point) **(Figure 2-5a.),** and migrate along with a fault plane or as gas chimneys (2.6.2) in upper, permeable layers. From there it can accumulate as shallow gas, or seep through the seabed to create pockmarks **(Figure 2-5b),** discussed later (2.6.4).

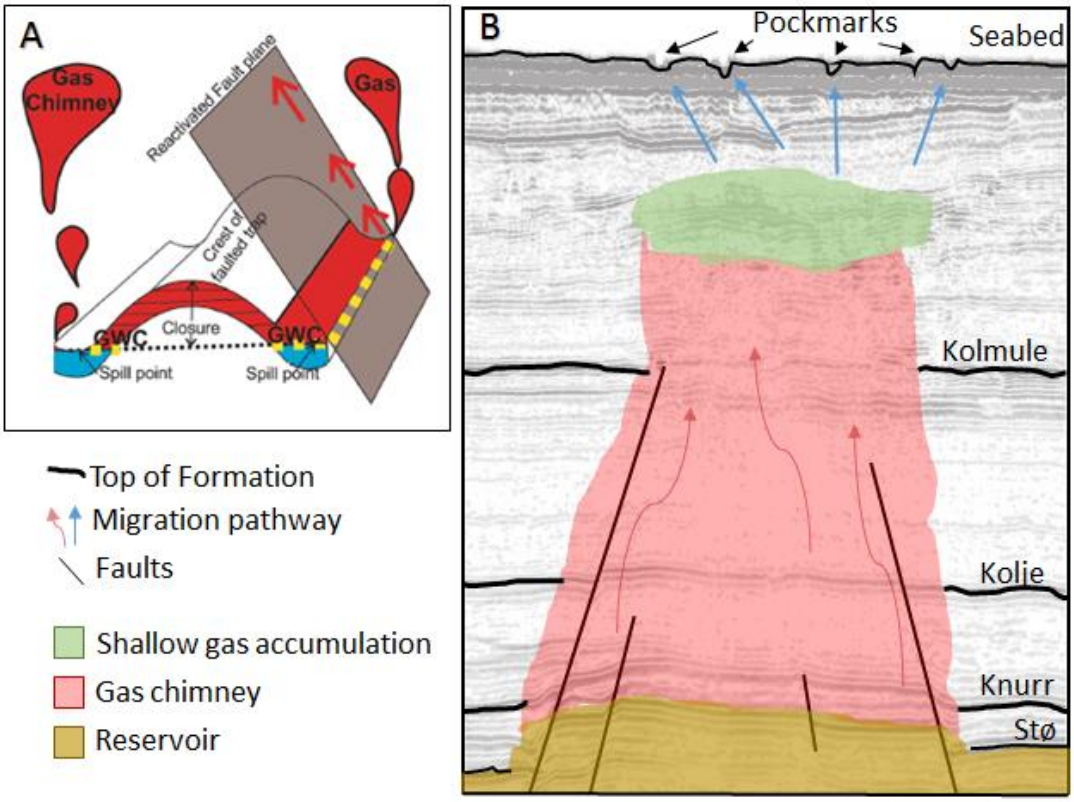

Figure 2-5 A: Sketch of hydrocarbon leakage trough the spill point of an anticline trap, creating gas chimneys and migration along a fault plane. Figure modified from(Tasianas et al., 2016). **B:** Illustration of possible fluid migration pathway from the seismic, with faults creating leakage in the reservoir. Large gas chimney forms, with accumulation of gas in the shallow sediments. Further migration causing leakage on the seabed and the formation of pockmarks.

2.2.3 Accumulation of fluids

Hydrocarbons generated from the source rock in an active petroleum system migrate into a trap and are preserved if the petroleum charge is greater than the sum of escaped hydrocarbons (Magoon et al., 1994). Hydrocarbon accumulation depends on the timing between the previously described mechanisms in the petroleum system (source rocks, migration pathways and reservoirs) and a solid sealing/cap rock (normally a low permeable mud rock or shale) (Buller et al., 2005; Magoon et al., 1999).

There are many ways to stop the migration of fluids, and the different trapping mechanisms are often categorized as either: 1) structural traps **(Figure 2-6A),** related to structural deformation of sediments (e.g. fault or anticline traps), 2) stratigraphic traps **(Figure 2-6B),** formed by depositional features (e.g. pinch-out, unconformity, reef or erosion traps) or 3) a combination of these (Biddle et al., 1994; Selley et al., 2015).

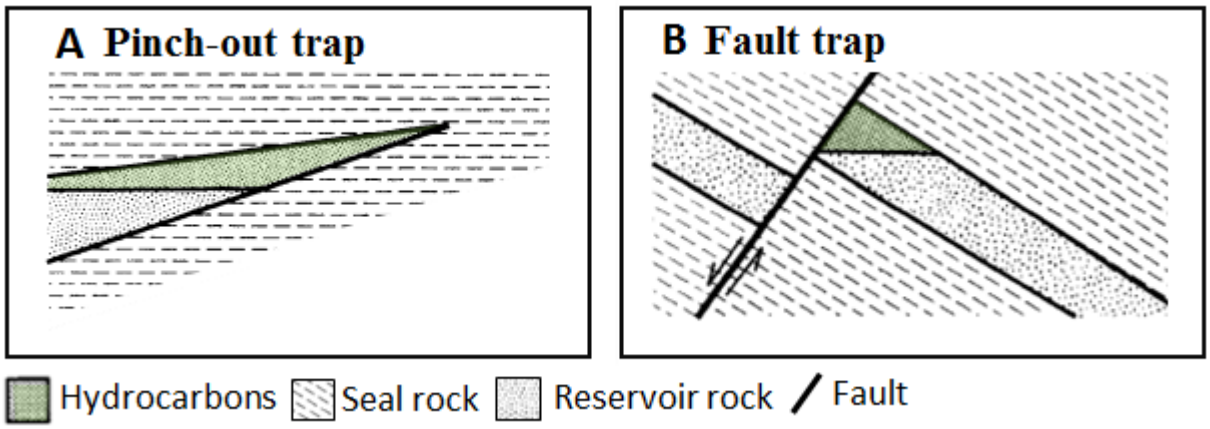

Figure 2-6 Stratigraphic and structural trap represented by **A)** pinch-out trap and **B)** fault trap. Modified from Biddle et al. (1994)

There is consensus among geologists that fluids trapped in a reservoir tend to accumulate in separate layers, with gas at the top, oil in the middle and water at the bottom **(Figure 2-7)** – due to density differences (Earle, 2015; Gussow, 1954; Schowalter, 1979; Selley et al., 2015). As stated by Gussow (1954) and illustrated in **Figure 2-7A**, hydrocarbons traveling vertically into a series of functioning trapping mechanisms are bound to accumulate sequentially, beginning with the filling of the lowest structure. If this is filled to its spill point, gas rise to the top, with only oil leaking into the next trap **(Figure 2-7Ai).** With proceeding migration, oil is continuously spilling updip, making the first trap completely gas filled, with no potential of accumulating any more oil **(Figure 2-7Aii).**

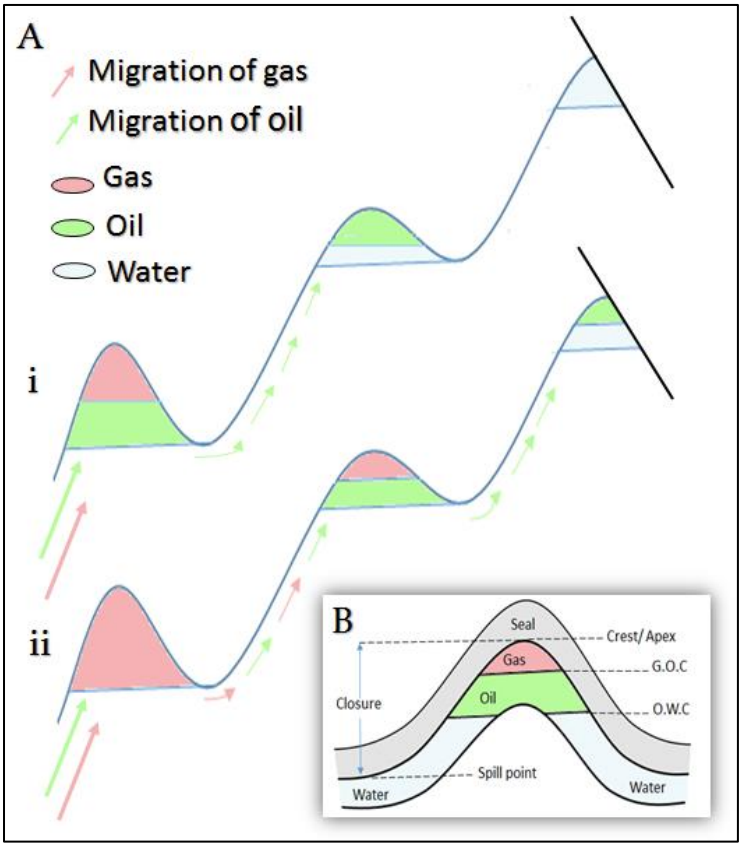

Figure 2-7 A Accumulation trends of hydrocarbons in interconnected trapping mechanisms. **A i)** Accumulation starts in the first trap, containing gas at the top, with leaking oil beneath. The second trap has oil accumulations, but no gas gap and the third trap is dry. **A ii)** Further migration leads to the accumulation of both oil and gas updip, with the first trap filled only with gas. The second trap has a gas gap and spills oil to the third, (fault) trap, where no further migration occurs. After (Gussow, 1954)
B shows a cross section of a anticline trap, including the most important elements. Modified from (Selley et al., 2015)

2.3 Shallow gas and gas hydrates

Accumulations of trapped gas located in the uppermost part of the stratigraphy is termed shallow gas, and is a worldwide phenomenon. The actual depth of the gas, in order to be termed "shallow", is defined differently. Some describe it as any gas event occurring before the so-called Blowout Preventer (BOP) is installed (P. S. A. N.-. PSA, 2007), which is a massive device placed at the seafloor to prevent the uncontrolled flow of fluids during well drilling operations (ndla, 2017). Due to the probability of gas escaping the casing in the shallow and poorly consolidated sediments, the BOP is not installed until the well has reached a certain depth (Solheim et al., 1987). Others define the shallow gas using a specific depth, typically the first 1000 meters within the subsurface (Davis, 1992; Floodgate et al., 1992; Grinrod et al., 1988; Solheim et al., 1987). In this study, as mentioned, all high amplitude anomalies above the upper Cretaceous Kolmule is interpreted as potential accumulations of shallow gas.

The formation of gas hydrates has been discussed by several scientists (Bryan, 1974; Floodgate et al., 1992; R. Hyndman et al., 1992a; R. D. Hyndman et al., 1992b; Kvenvolden, 1993; Kvenvolden et al., 1980; Pecher et al., 1996; Shipley et al., 1979; Sloan, 1998; Solheim et al., 1987), and the definition is quite similar: crystalline, ice-like compounds of water and gas (often methane) occurring at high pressures and low temperatures. The discovery of gas hydrates was made at the beginning of the 19th century (Miller, 1974), and the phenomenon was later accused to cause blocking of pipelines (Hammerschmidt, 1934). Since then it has been a nightmare to the hydrocarbon industry, purposing a hazard to drilling operation (Solheim et al., 1987). To prevent formation of gas hydrates in exploration related mechanisms, the hydrocarbon industry spends about one billion US dollars every year (Makagon, 2010).

Gas hydrates are commonly located in areas with active seepage, expressed in relation to the bottom-simulating reflection (BSR) (R. Hyndman et al., 1992a; Kvenvolden et al., 1980). This is defined as the base of the gas hydrate stability zone (GHSZ) (Kvenvolden, 1993b), which refers to the area where hydrates tend to accumulate (Solheim et al., 1987). Shipley et al. (1979) explains how the BSR mimic the seafloor reflection in the seismic (with reversed polarity) and thus cut across other reflections. The strong BSR reflection is a result of the sudden change in acoustic impedance **(2.5.1)** on the sediment interface between gas hydrates and underlying free gas (Alan Judd et al., 2007). Sediments containing gas hydrates may prevent seepage of fluids on the seafloor, as they often act as a sealing for migrating gas. Hydrocarbons trapped beneath the hydrate stability zone is often referred to as free gas (Alan Judd et al., 2007), and Floodgate et al. (1992) also discuss the possibility for destabilized gas hydrates as a potential source of this shallow gas accumulations. Knowing that 1 cubic meter of gas hydrates may contain up to 170 m^3 of free gas (Kvenvolden, 1993b), this is not a bad assumption.

A bathymetry map, provided by Vadakkepuliyambatta et al. (2017) indicates alternating GHSZ throughout the Barents Sea, and propose different stability zones for various gas compositions **(Figure 2-8).** Notice how the Hammerfest Basin react on gas composition regarding thickness of GHSZ.

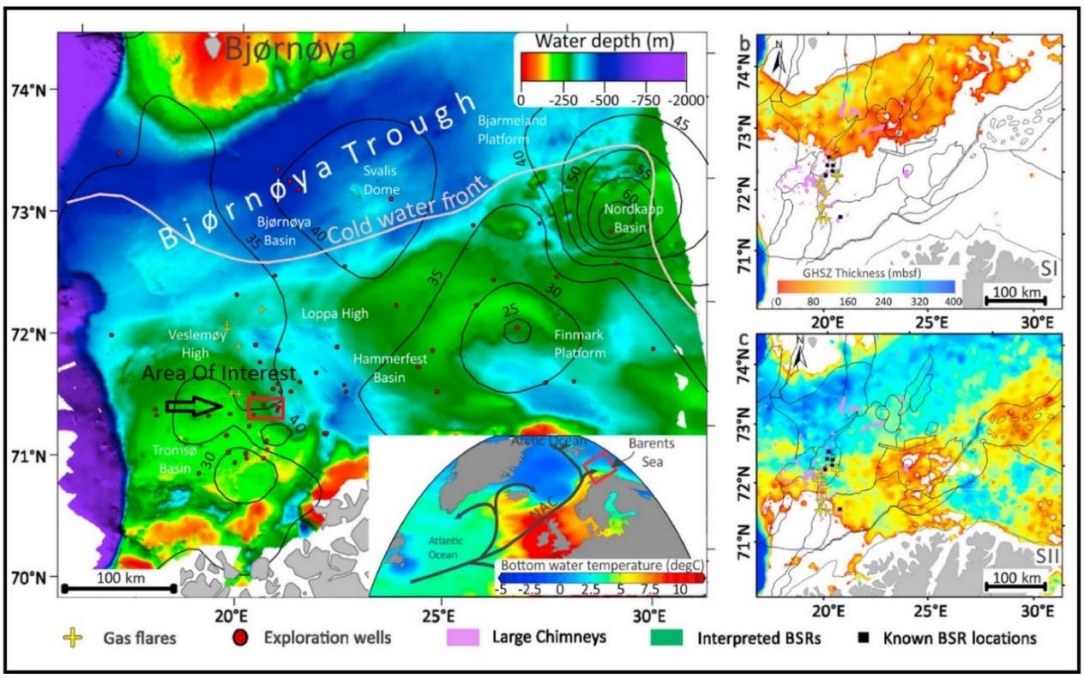

Figure 2-8 Bathymetry of the SW Barents Sea, showing interpreted BSRs, including wells and bottom water temperatures. Snøhvit area (with high density of BSR) marked with red square. Maps on the right hand side include modeled gas hydrate stability zones for SI (100% methane) (top corner) and SII (96% methane + 3% ethane + 1% propane) (bottom corner). Modified from (Vadakkepuliyambatta et al., 2017)

The influence on glaciers in Hammerfest Basin, regarding the stability of hydrates is shown in **Figure 2-9**. Ostanin et al. (2013) suggests pressure, bottom water temperature, gas composition, geothermal gradient and water salinity as the main factors controlling the GHSZ, and this also reveals increased GHSZ with increased gas composition.

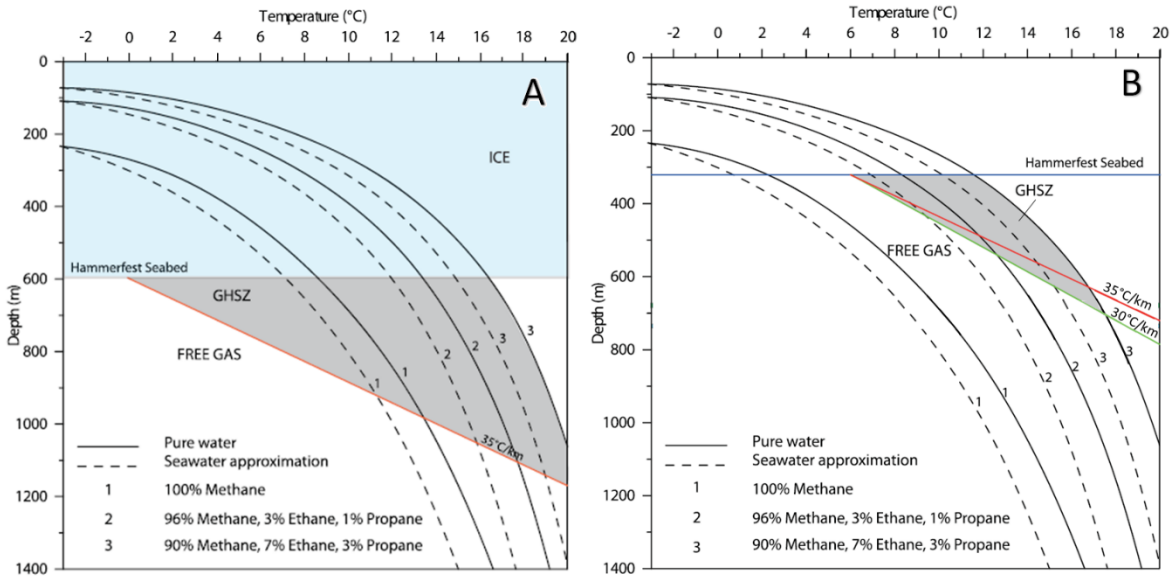

Figure 2-9 Gas hydrate stability diagrams showing how the stability changes from **A)** Last Glacial Maximum (LGM) and **B)** Present day conditions. Modified from (Ostanin et al., 2013)

By including well logs to detect hydrate-bearing sediments, common log curves will have this signature: high resistivity, short interval transit time (high velocity), increased gamma ray values and high gas readings while drilling (Zou, 2017), see **Figure 2-10.**

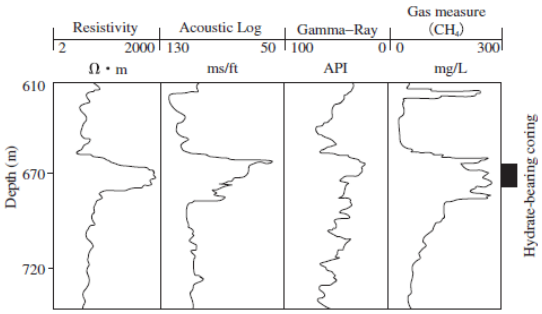

Figure 2-10 Log curve pattern indicating gas hydrates From (Zou, 2017)

Drilling from offshore rigs into accumulations of shallow gas and gas hydrates may cause major blow-outs. Studies show that a large number of drilled wells in the Norwegian sector have experienced events related to shallow gas accumulations, 44 to be exact, during the period from 1984 to 2006 (PSA, 2007). Eight of these in the course of production drilling, and 36 during wildcat (exploration) drilling. One of the most dramatic examples of a blowout event in Norway happened in 1985 on West Vanguard in the Norwegian Sea **(Figure 2-11)**. The accident occurred before the BOP was installed, at around 500 meters (Grinrod et al., 1988). The bit entered a shallow gas pocket, causing the well to blow out. The explosion caused a lot of material damage, environmental challenges due to oil spill, and the loss of a human life.

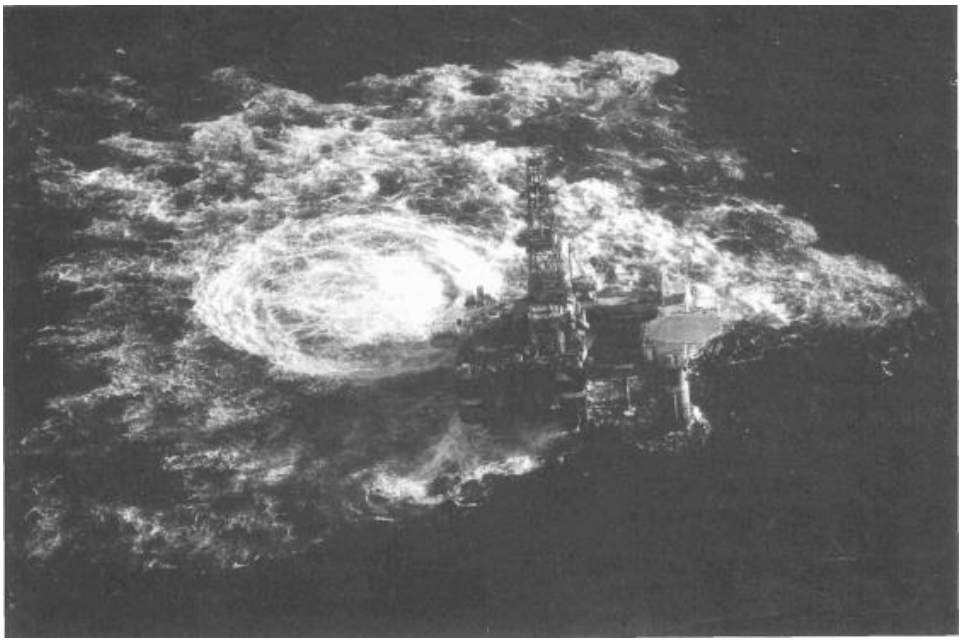

Figure 2-11 Gas seeping through the ocean into the atmoshphere, occuring from a blowout incident on West Vanguard in the Norwegian Sea. The same result as from natural gas leakage through the seabed. From (Martin Hovland et al., 1988)

2.4 Faults

The Hammerfest basin is strongly affected by tectonic activity, providing a complex province, influenced by different sets of structures with fractures and faults. Regarding the behavior of fluid flow in the subsurface, faults play an important part and may even affect the sealing capacity of reservoirs.

A fault, or a fracture, is a narrow zone in the Earth's crust where one side has moved relative to the other (Twiss et al., 1992). The two terms are often used synonymously, but it is also common to label structures with offsets exceeding one meter as faults (Fossen et al., 2005), and fractures (or microfaults) when the offset only displays in the scale of centimeters or millimeters (Fossen et al., 2005; Twiss et al., 1992). Over a long period of time, many major shear zones produce repeated displacements. Once developed, they appear to weaken, as they undergo repeatedly episodes of reactivation during successive cycles of crustal deformation (Rutter et al., 2001). Many shear zones also act as fluid pathways (Fossen et al., 2005; Rutter et al., 2001), which may contribute to the weakness relative to their surroundings (Rutter et al., 2001). Fluid flow along fault planes provides the possibility for fluids in deep reservoirs to migrate to shallower pockets of stratigraphy (Fossen et al., 2005; Ligtenberg, 2005).

2.4.1 Fault types

Faults are often classified based on the angle dip of the faults and its relative direction and displacement. When looking at the movement of the two blocks along a fault plane, there are three primary fault types; dip-slip faults, strike-slip faults and oblique-slip faults (Bennison et al., 2013; Twiss et al., 1992, 2006) **(Figure 2-12).** The above mentioned slip is defined as the net distance and direction of the hanging wall relative to the footwall. The dip-slip faults have movement parallel to the fault surface, while strike-slip faults have parallel to horizontal movement to the strike of the fault surface (Twiss et al., 1992). Oblique-slip faults will have slip inclined obliquely on the fault surface (Fossen et al., 2005; Twiss et al., 1992).

Whether a dip-slip fault is a normal (extension) or a reverse (compression) fault, is decided by the relative movement of the fault blocks. The hanging wall block is defined as the block above the fault plane, and the footwall block as the block below **(Figure 2-12).** In a normal fault regime, the hanging wall block moves down relative to the footwall block, caused by extensional forces (Twiss et al., 1992). In reverse dip-slip faults, the hanging wall block will move upwards relative to the footwall block (Twiss et al., 1992).

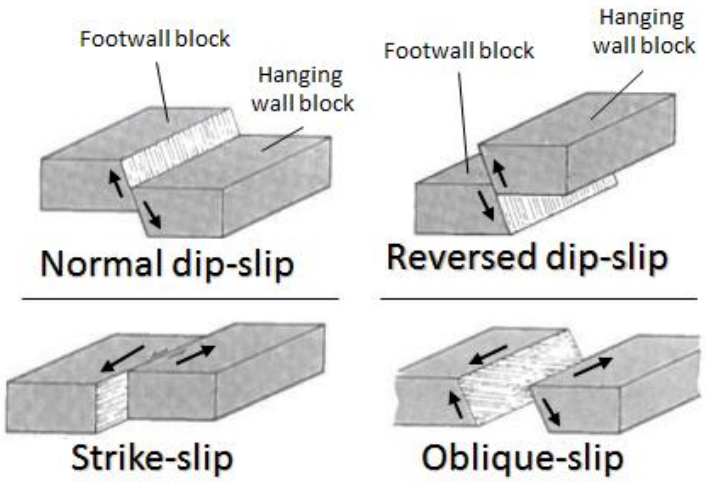

Figure 2-12 Illustration showing characteristic displacement for the different fault types. Modified from (Bennison et al., 2013)

2.4.2 Polygonal faults

From seismic exploration in the SW Barents Sea, uniformly developed fault arrays are observed in sedimentary basins, often confined to a specific succession or stratigraphic unit. These features are known as polygonal faults and have a polygonal expression on the surface **(Figure 2-13),** formed in sediments dominantly consisting of clay-sized particles (Berndt et al., 2003; Cartwright, 2011; Mansfield et al., 1996). The importance of investigating this type of faulting is explained by the relation to fluid flow, hydrocarbon accumulations and the dynamics of reservoirs (Cartwright, 2011).

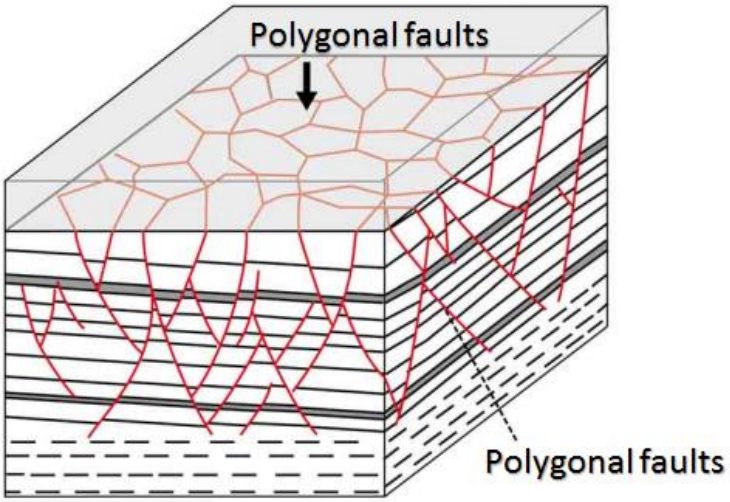

Figure 2-13 Schematic illustration of polygonal faults from a 3D seismic approach, seen from the vertical section and the horizontal surface. Modified from (Petracchini et al., 2015)

Different theories of the processes behind the origin of these faults have been made (Davies et al., 2011; Dewhurst et al., 1999; Goulty, 2008; Henriet et al., 1989), and will not be discussed in detail here. Polygonal faults may serve as conduits for fluids in areas with sufficient overpressure (Lonergan et al., 1999), and they are proven to have a stratigraphic relationship to fluid escape features (Berndt et al., 2003). Polygonal faults are not directly related to tectonic activity, but in zones of weakness during later tectonic events, they can be reactivated as tectonic faults, giving the impression that the initial polygonal faults are of extensional or compressional origin (Ostanin et al., 2012). Polygonal faults are normal (extensional) dip-slip faults with fault planes usually ranging from about 50-80°. Deeper faults tend to show fault systems with lower angles, of 20-50° (Lonergan et al., 1999).

2.4.3 Fault recognition, fault interpretation and fault displacement

Discontinuities in the stratigraphy may indicate the presence of a fault, but can also originate from features such as unconformities or intrusive contacts. Identified horses, displaced a significant distance from its original position along a discontinuity, is a clear evidence of a fault. The identification of the original stratigraphic position of the rocks indicates the distance and the direction of the movement (Twiss et al., 1992).

To investigate the history of growth, linkage and reactivation of a fault, displacement analysis on the seismic data is relevant. By correlation of similar reflectors across the fault, the dip separation can be estimated by calculating the throw and the heave of the fault (Brown et al., 1996) **(Figure 2-14).** The throw is the change in vertical elevation between the hanging wall and the footwall cutoff lines in the direction of the fault dip. The heave is the map distance in the direction of the fault dip between the hanging wall and footwall cutoff lines (Groshong Jr, 2006).

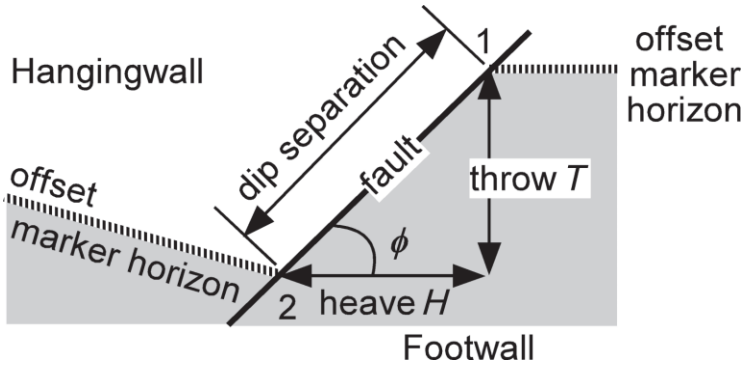

Figure 2-14 Sketch of dip separation in a fault. Throw is the vertical and heave is the horizontal component of the dip separation. From (Groshong Jr, 2006).

The throw and heave are related to the stratigraphic separation, and the dip of the fault is determined from the heave and throw by the equation

$$\boldsymbol{\varphi} = arctan\frac{\boldsymbol{T}}{\boldsymbol{H}} \qquad \textbf{(Equation 2-4)}$$

φ is the fault dip, T is the throw and H is the heave

2.4.4 Fault reactivation

Repeated faulting and fracturing will weaken the cohesion strength of a rock. Hence, the energy required to reactivate faults are lower compared to initiating new faults (Fossen et al., 2005). Mapping throw depths in seismic profiles can provide insights about the grow history of a fault, and help distinguish between faults developed through syn-sedimentary extensional faulting and faults developed from blind propagation (Tvedt et al., 2013). Analyzing throw and displacement profile of faults can strengthen the understanding of timing of fault propagations and reactivations, including linking these processes to the timing of fluid migration in the area.

2.5 Seismic principle

2.5.1 Acoustic impedance

The method of seismic investigation is related to the acoustic impedance (AI) contrast between different lithologies, given by

$$\boldsymbol{AI} = \boldsymbol{v}\rho, \qquad \textbf{(Equation 2-5)}$$

Where v is the P-wave propagation velocity in a specific layer and ρ is the density.

The reflection, or refraction, of a seismic wave is created where there is a change in acoustic impedance, which is recorded by a receiver to create seismics based on the arrival time and amplitude of the signals. Strong amplitudes implies high acoustic impedance

2.5.2 Vertical resolution

The ability to separate and recognize two vertically displaced reflectors in the seismic is determined by the vertical resolution. It also reveals the smallest an object or a feature has to be in order to appear in the data (Kearey et al., 2002; Lin, 2012) This resolution is defined to be ¼ of a wavelength, λ, which is

$$\lambda = \frac{v}{f}$$ **(Equation 2-6)**

v = velocity (m/s), f = frequency (Hz).

If the thickness of a layer is less than the calculated resolution, the top and bottom reflector will most likely merge into a single waveform, causing destructive interference (Bilat, 2005). The vertical resolution in this study is given in **section 4.2**.

2.5.3 Horizontal resolution

Horizontal resolution refers to the ability to distinguish between two laterally displaced features (Kearey et al., 2002). As seismic waves travel as wavefronts, the reflection is generated from a spherical area, known as the Fresnel zone. The Fresnel zone of the first wavefront is dependent on the arrival of the next, which arrives λ/4 behind. The reflection from the second wavefront will interfere destructively with the first (R. Sheriff, 1985), and the horizontal resolution on un-migrated data is defined by the width (diameter) of the first Fresnel zone, given by

$$rf = \frac{v}{2}\sqrt{\frac{t}{v}}$$ **(Equation 2-7)**

Where, rf is the diameter of the Fresnel zone (m), f is the frequency (Hz), t is the two-way travel time in seconds and v is velocity (m/s) (Kearey et al., 2002; R. Sheriff, 1985).

In the processing of seismic, migration of the data is done to enhance the horizontal resolution. In migration of 3D seismic, diffractions are collapsed back to their point of origin, which reduces the Fresnel zone to a small circle. In theory, with perfect migrated data, the extent of the Fresnel zone will be one quarter of a wavelength (Kearey et al., 2002; R. Sheriff, 1985).

2.6 Seismic indications of hydrocarbons

Fluid flow related features are identified both on the seabed as pockmarks and in the sub-surface as high seismic amplitude anomalies, gas chimneys and seismic pipes. Hydrocarbons leave imprints in the stratigraphic successions during their passage to the surface and may also be temporarily or permanently trapped in the subsurface (Badley, 1985; Hustoft et al., 2007).

2.6.1 Amplitude anomalies

Change in velocity and density compared to surrounding bed rocks cause acoustic impedance contrast, causing the amplitude anomalies seen in the seismic data (Andreassen, 2009).

Bright spots

A bright spot is a hydrocarbon indicator associated with high negative amplitude (Alan Judd et al., 2007), due to significant acoustic impedance contrast compared to local surroundings **(Figure 2-15)**. The bright spots are just *indicators* and can also detect different lithology changes (Müller et al., 2018). They are often found in porous sands (Badley, 1985).

Flat spots

In a thick enough reservoir, the gas-/water, oil-/water, gas-/oil-contact may appear as a distinct reflection (Telford et al., 1990). They tend to show up as horizontal reflectors in the vertical profile **(Figure 2-15),** cutting across the surrounding, dipping reflections. These are possibly the best gas indication (Andreassen, 2009) and they will always have positive reflection coefficient. They appear as a result of contact between gas/oil and water in a reservoir.

Phase reversal

When a single reflector suddenly switches from low amplitude to high amplitude (or the other way around), showed by a sudden color change in the seismic section, phase reversal appear **(Figure 2-15).** If the acoustic impedance of a brine-filled reservoir is slightly larger than the adjacent shale, the reduction by hydrocarbons may reverse the polarity of the reflection (Telford et al., 1990). The reversal is always observed along a continuous reflection with phase shift of 180° making the peak a through and vice versa (Løseth et al., 2009).

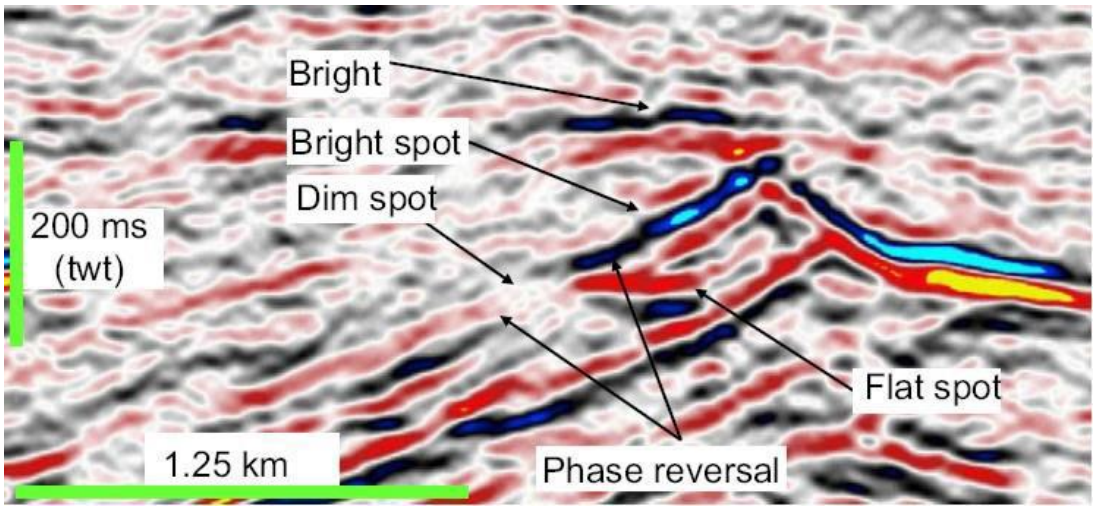

Figure 2-15 Seismic, vertical profile showing potential hydrocarbon indicators in terms of a flat spot, phase reversal, dim spot and bright spot. From Andreassen (2009).

2.6.2 Gas chimneys

Vertical migrations of gas in the overlying stratigraphy can interrupt the seismic records, causing wide wipeout zones with weak, disturbed and chaotic reflections, called gas chimneys (Cathles et al., 2010; Løseth et al., 2009). They are characterized by relatively low amplitudes (Meldahl et al., 2001), and are often associated with other hydrocarbon indicators, such as bright spots, pipes and pockmarks **(Figure 2-16)**. The distorted reflections may indicate either ongoing migration of gas, or previous migration and originates from scattering of energy related to breccations/fractions of sediments (Badley, 1985).

2.6.3 Seismic pipes

Seismic pipes are disturbances defined as vertical hydrocarbon migration pathways (Cartwright et al., 2015; Ligtenberg, 2005). They are typically formed by hydraulic fracturing of the sealing stratigraphy due to rapid upward fluid flow, and might cause major blowout events on the ocean floor (Hustoft et al., 2007), resulting in the formation of pockmarks **(Figure 2-16)**.

2.6.4 Pockmarks

Shallow, elliptical to circular crater-like depressions observed on the seafloor from a few meters to tens of meters deep, are termed pockmarks (Hovland, 1982; M Hovland et al., 1988; AG Judd et al., 1992; King et al., 1970; Løseth et al., 2009; Schroot et al., 2003). They usually occur within soft, fine-grained sediments on the seabed, produced by seepage of gas or fluids into the ocean, in proximity to gas chimneys and pipes (Cartwright et al., 2007; Løseth et al., 2009). The formation is often related to pockets

of shallow gas reservoirs **(Figure 2-16),** and may indicate an active petroleum system in that area (Cathles et al., 2010).

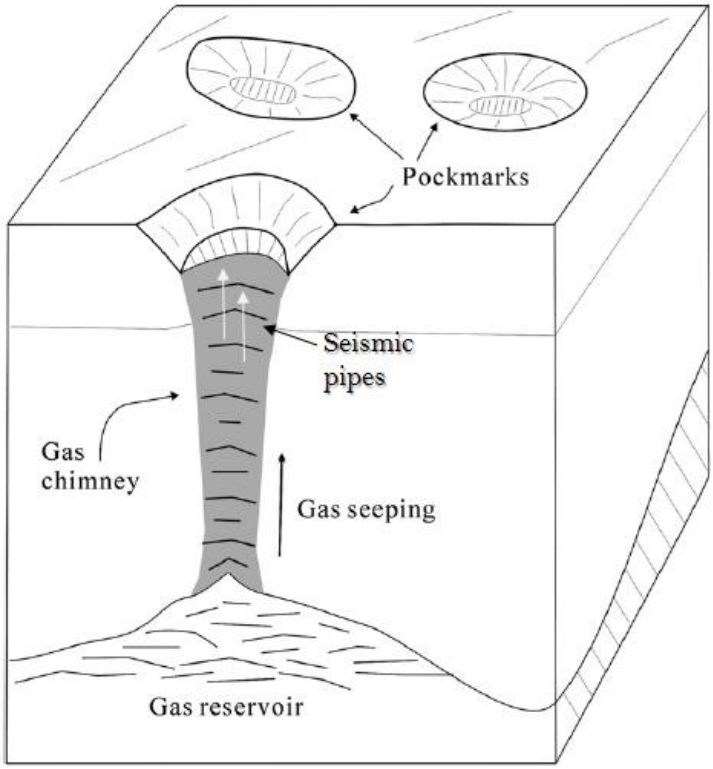

Figure 2-16 Illustration of pockmark formation at the seabed, originating from a leaking hydrocarbon reservoir and a large vertical gas chimney. Modified from Cathles et al. (2010).

2.7 Carbon capture and storage (CCS)

Despite increased awareness of global warming and sustainable energy, the future still depends on energy from fossil fuel resources. Steeneveldt et al. (2006) stated that approximately 80% of the world's total energy requirements in the coming decades, probably will originate from nonrenewable energy. This has led to increasing awareness on carbon capture and storage (CCS), where the limitation of anthropogenic emissions to the atmosphere is the main objective. CO_2 is a major greenhouse gas, mainly caused by the combustion of fossil fuels (Benson et al., 2008; Herzog et al., 2004; Parson et al., 1998; Steeneveldt et al., 2006). Sleipner CCS project, initiated in 1996, was the first large scale storage of CO_2 in geological formations (Steeneveldt et al., 2006). Research from this project have contributed to guidelines on how future CCS projects should be monitored using repeated (4D) seismic and time-lapse seabed gravimetric data to improve reservoir understanding (Furre et al., 2017).

Theoretically, two approaches to CCS can be performed. One is to capture CO_2 directly from the atmosphere by enhancing the natural uptake of carbon dioxide in plants, marine sediments and soils. The other possibility is the capture directly from the industrial source and subsequent sequestration in geologic or oceanic reservoirs (Benson et al., 2008; Herzog et al., 2004). When CO_2 is separated, it is compressed to a liquid state at 100 bar, and transported to the storage location by pipeline or by ship (Benson et al., 2008).

When captured, CO_2 needs to be stored, not emitted to the atmosphere. The storage method should meet certain criteria, like storage security for a long period of time (100-1000 of years), low storage and transportation cost, and should meet all national or international regulations (Herzog et al., 2004). Using drilled wells, captured CO_2 can be pumped down to subsea basins of sedimentary rocks, which include sands that represent the storage space and silt, clay or evaporites that provide seals (Benson et al., 2008). CO_2 have higher density than water, hence fine-textured rocks prevent the upward migration of CO_2 by a combination of viscous and capillary forces (Benson et al., 2008).

2.7.1 CCS at Snøhvit

The sequestration of CO_2 in Snøhvit has been in operation since 2008. Yearly, approximately 0,7 million tons of carbon dioxide is stored in the subsea development, located 143 km northwest of Hammerfest. The unprocessed well stream is transported through a multiphase pipeline to the LNG processing facilities at Melkøya **(Figure 2-17).** The content of CO2 in the gas stream is 5-8 mole%.

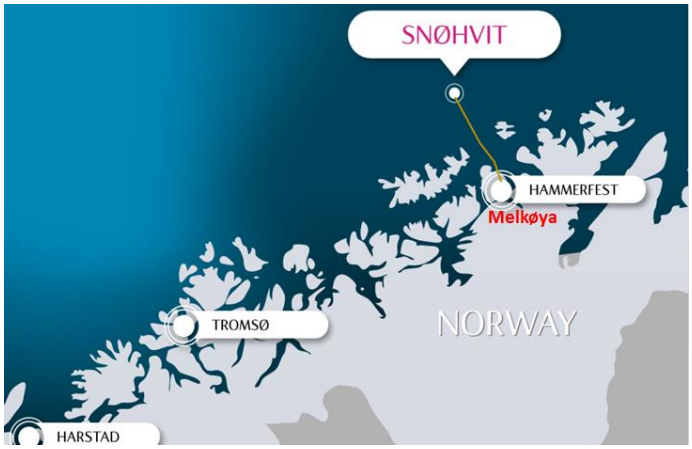

Figure 2-17 Location of Snøhvit field. Modified from (Equinor, 2018)

Due to the technical requirement for the liquefaction process to keep CO_2 content below 500 ppm, to prevent freezing in the cryogenic heat exchangers, the CO_2 is captured in an amine plant. It is then compressed and transported back to the Snøhvit field through a 153 km long pipeline (Negrescu, 2008), and reinjected into the reservoir. At first the CO_2 was injected into the Tubåen reservoir, but due to poorer properties than expected and an observed pressure build up, the injection interval was moved to the Stø formation (**Figure 2-18**).

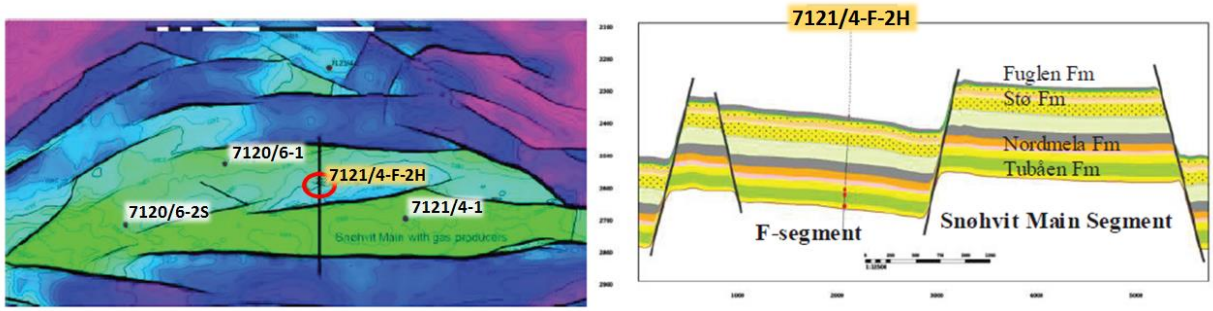

Figure 2-18 Left hand side: depth map of Top Fuglen with well locations. Right hand side: location of the 7121/F-2H CO_2 injector. It was previously injecting in the Tubåen Formation but is now injecting in the Stø formation. Modified from O. Hansen et al. (2013)

2.7.2 Risks related to carbon storage

Monitoring the subsurface movement of CO_2 is carried out at several sites (O. Hansen et al., 2013). Risks associated with geological storage are comparable to the risks associated with gas injection, natural gas storage and enhanced oil recovery (Benson et al., 2008). The increasing number of storage projects promote improved strategies for the management of risk associated with deep geological storage (Steeneveldt et al., 2006).

Carbon dioxide is stored in the underground to avoid emissions to the atmosphere. Considering the total risk, there are several ways the CO_2 may leak from the reservoir and up into the overburden (Miljødirektoratet, 2016):

- Horizontal migration of CO2 outside the planned reservoir
- Leakage through plugged and abandoned exploration wells in the formation
- Leakage through future changes in the formation and in the cap rock
- Leakage through existing faults and weaknesses in the cap rock
- Fracturing the cap rock because of pressure build up in the formation

3 Study Area

3.1 Introduction

The study area is located in the Snøhvit field, which represent the first offshore development in the southern Barents Sea. It is centered in the Hammerfest Basin, separated by structural highs and platforms (Jan I. Faleide et al., 1993; Larsen et al., 1993) (**Figure 3-1**), making it a complex region for petroleum exploration. Seismic investigation of the Barents Sea began in the early 70s, and knowledge about the geological history has been of great interest since. Understanding the tectonic and depositional evolution is crucial in order to predict the behavior of hydrocarbons in the subsurface, regarding both commercial and safety interests.

The Barents Sea covers an area of more than one million square meters, including complex fault systems, structural highs and a variation of basins and platforms. It has a long geological history, including a combination of tectonic events and varying depositional and climatic conditions since the late Paleozoic (Dore, 1995; Gabrielsen et al., 1990; Smelror et al., 2009; Worsley, 2008). Throughout time, repeatedly periods of uplift and erosion together with extension and subsidence has controlled sedimentation in the Barents Sea, inducing the present day configuration (Worsley, 2008).

The eastern and western part of the Barents Sea represents major differences in tectonic complexity, with the western region, the focus in this study, showing more complicated structures than the eastern region Smelror et al., 2009. The origin and evolution of all aspects affecting the large, epicontinental sea is covered by many scientists (L. Berglund et al., 1986; Dore, 1995; Jan Inge Faleide et al., 1984a; Jan I. Faleide et al., 1993; Gabrielsen et al., 1990; Smelror et al., 2009; Worsley, 2008), and the following subchapters will provide a brief summary of the tectonic evolution in SW Barents Sea, depositional settings in Hammerfest Basin and the petroleum systems in Snøhvit.

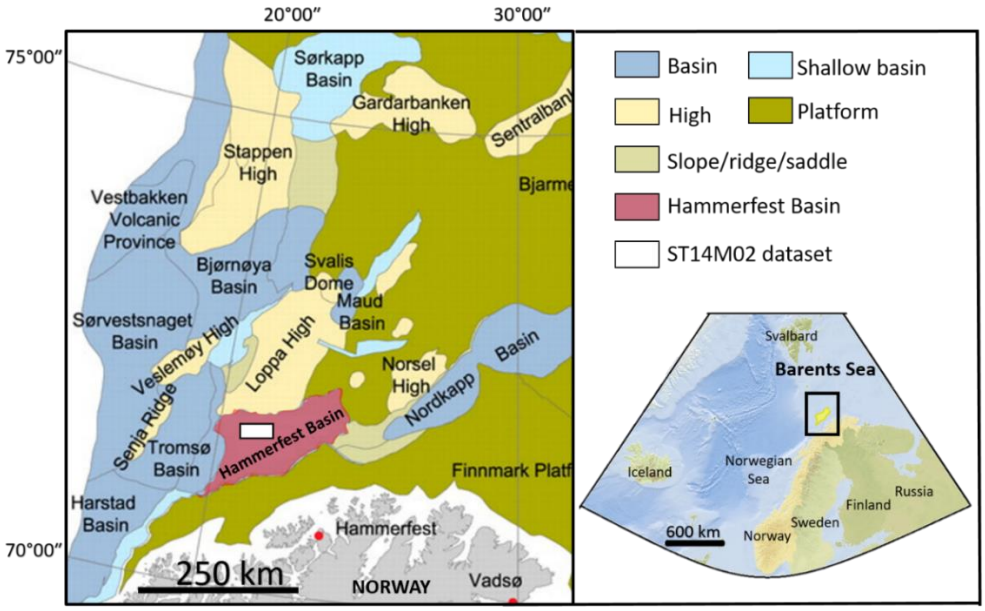

Figure 3-1 Location of study area with main structural elements in the southwest Barents Sea. The red shaded figure marks the Hammerfest basin. Modified from (Henriksen et al., 2011; NPD, 2017)

3.2 Tectonic evolution of the SW Barents Sea

3.2.1 Paleozoic (541 – 254 Ma)

The Barents Sea is located on the northwestern part of the Eurasian continental shelf, which originally was formed by two major continental collisions, and later went through continental separations (Dore, 1995). The first collision occurred in mid Paleozoic time, between the continent Baltica in east and Laurentia in west. This resulted in the closing of the Iapetus Ocean (**Figure 3-2**) and the development of the Caledonian orogeny, approximately 400 million years ago. The second collision occurred in late Paleozoic between Laurussia and western Siberia, an event that initiated the development of the northern Uralian orogeny, influencing the geology of the entire Barents Sea (Dore, 1995). Later, the eastern part of the Barents Sea has undergone less tectonic activity, while the western parts continued to be tectonically active in Mesozoic to Cenozoic times (Gabrielsen et al., 1990).

From the beginning of late Carboniferous, the tectonic development in the western Barents Sea was dominated by regional subsidence. During late Devonian-early Carboniferous a change occurred in the stress regime, as a continuation of the northeastern Atlantic division between Greenland and Norway, and the area went from being a compression regime to an extension regime (**Figure 3-2D**). Rift basins were formed and filled with continental clastic material, carbonates and evaporates (Jan Inge Faleide et al.,

1984b). Evaporites represent effective top seal to hydrocarbon accumulation due to low porosity and permeability, and often laterally continuous at a basin scale (Dore, 1995).

When the Caledonian compression regime was transferred into a large-scale regime of "strike-and-dip" plate movements, these movements led to formation of horst- and graben structures. In late Paleozoic, a 300 km wide and more than 600 km long NE-SW oriented rift zone was formed in the Western Barents Sea, a fan shaped range of basins, separated by fault-defined highs. The highs were NE-SW oriented parallel to the corresponding rift zone, but are today orientated N-S. As the rifting ceased in late Carboniferous, the western Barents Sea underwent regional subsidence (Gudlaugsson et al., 1998).

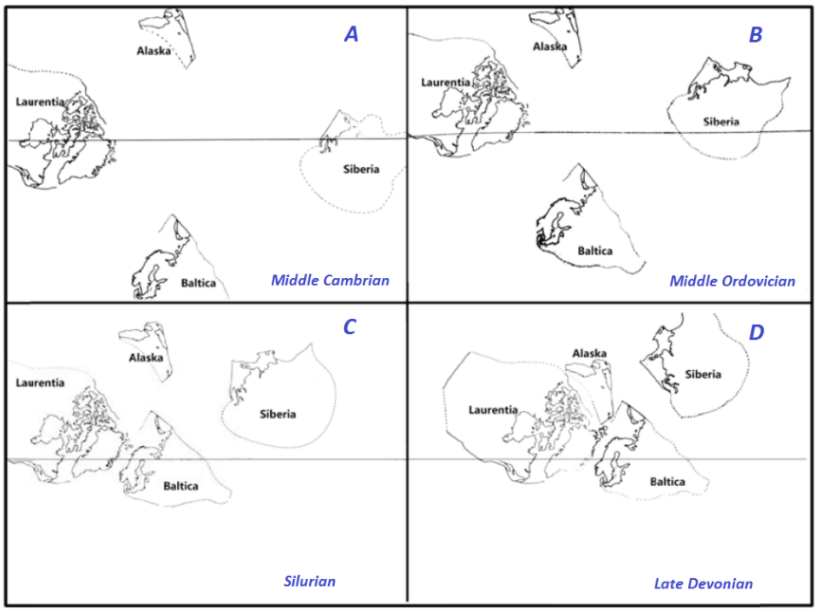

Figure 3-2 Opening and closing of the Iapetus Ocean from Mid Cambrian to Late Devonian. **A)** Iapetus opens until Early Ordovician. **B)** Iapetus turns to close during Middle Ordovician. **C)** Baltica collides with Laurentia at east Greenland at Silurian times. **D)** Baltica becomes part of Laurentia after collision. When it moves northward, extensive first order NE-SW oriented strike-slip faults are formed in the SW Barents Sea. Modified from (Smith et al., 1988).

In Carboniferous, the Barents Sea drifted northwards, and the climatic conditions changed. A warmer climate ensured the formation of extensive carbonate platforms, where thick successions of evaporites were locally deposited in graben structures, e.g. the Tromsø, Nordkapp and Bjørnøya Basins (Jan Inge Faleide et al., 2008; Smelror et al., 2009; Worsley, 2008). According to (Smelror et al., 2009), metamorphic basement rocks from late Silurian and early Devonian age cover the sediments in the western Barents Sea, and the basement was formed under the origin of the Caledonians.

3.2.2 Mesozoic (252 – 72 Ma)

In early Triassic, the Uralian orogeny, the uplifted Novaya Zemlya area and the Fennoscandian shield became major sediment sources for basins and platforms in the western Barents Sea. The new supply of sediments resulted in a westward progradation of the coast, and the development of large tidal inlets, estuaries and lagoons (Smelror et al., 2009). Tectonic activity occurred especially along the western margin, where the Loppa High was uplifted and eroded. A basement-involved regional extension gave rise to salt-diapirism in the Nordkapp Basin during early Triassic (Nilsen et al., 1995).

Triassic to early Jurassic represented a tectonically quiet period in the Barents Sea area (Gabrielsen et al., 1990), but extensional tectonics took place in middle Jurassic, when the Barents Sea was subject to regional extension and adjustments along old structures (Jan I. Faleide et al., 1993). The Late Jurassic transgression reached maximum, and much of the Barents region transferred to an open marine system. The Hammerfest basin and Bjørnøya basin experienced a period of rifting in Middle–Late Jurassic, where the rifting followed the pre-existing tectonic structures (Jan Inge Faleide et al., 1984a; Jan I. Faleide et al., 1993). The tectonic activity is increased in frequency during Late Jurassic and Early Cretaceous, when the present-day major structural elements of the Barents Sea were established (Gabrielsen et al., 1990). At the end of the Cretaceous, reverse faulting and folding increased and led to erosion in large areas, especially in the northern part of the western Barents Sea.

3.2.3 Cenozoic (66 Ma – present)

In early Cenozoic, seafloor spreading took place in the Eurasia Basin and the southern parts of the Norwegian-Greenland Sea. The western Barents Sea margin developed as a shear margin within the De Geer Zone. In the transition from Eocene and Oligocene, in the opening of Norwegian-Greenland Sea, this sheared margin evolved into a combined shear-rift margin (Jan I. Faleide et al., 1993). Basins along the margin were uplifted and subsided, and central parts of the rift margin experienced volcanism due to rifting. This resulted in to the formation of the Vestbakken Volcanic Province. Basins along the margin were uplifted and subsided due to local movements (Faleide et al., 1993).

In Pliocene the climate changed, resulting in large ice sheets covering much of the Northern Hemisphere. The climatic fluctuations caused several phases of glaciations and deglaciations. The uplifted Barents Sea shelf was subject to extensive glacial erosion. Repeated periods of erosion led to regional hiatus in the stratigraphic records. This hiatus is called the Upper Regional Unconformity (URU), separating underlying Mesozoic-Paleogene sediments and overlying glacial sediments (Smelror et al., 2009), and is present over most of the Barents shelf. The Svalbard area is considered to have gone through the most

extensive erosion, where 2 – 3 km of overlying beds were removed, whereas in the Hammerfest Basin and the Loppa high, the eroded material represents a thickness of 1 – 1,5 km (Smelror et al., 2009). In these processes, enormous amounts of sediments were transported by glaciers towards west, and led to sediment accumulations of up to 4 km in Bjørnøya and Storfjorden fan (Smelror et al., 2009). The extensive Cenozoic glaciation and its implications in the study area is further described in the next subchapter.

3.3 Glaciation history in the Study Area

The severe uplift and erosion that took place during the Cenozoic, the quantity of sediments removed and the timing of this removal have had important implications for exploration activity in the Barents Sea (A. Doré et al., 2000). The release of shallow gas into the ocean in this region has been found to be strongly linked to the retreat of the ice (Ostanin et al., 2017; Ostanin et al., 2013).

The Cenozoic erosional history of the Barents Sea is complex, caused both by tectonic and glacial processes, where the tectonic uplift is linked to plate reorganization in the Norwegian-Greenland Sea (Cavanagh et al., 2006; A. G. Doré, 2002). During Late Pliocene-Pleistocene, major glaciation and deglaciation caused extensive erosion from the shelf areas of the Western Barents Sea, leading to widespread deposition of thick sedimentary wedges on the continental slopes (Laberg et al., 2012). In the Barents Sea, different areas have been subject to different magnitudes of erosion (Henriksen et al., 2011). The massive redistribution of material during Cenozoic resulted in structural uplift and tilting, affecting underlying traps and probably entire hydrocarbon systems (Cavanagh et al., 2006). Probably, these glacial processes caused changes in hydrocarbon generation, secondary migration, fluid composition and location of pools (A. G. Doré, 2002). Removal of overburden caused leakage of hydrocarbons, resulting in empty reservoirs or structures not being filled to spill (Henriksen et al., 2011). In the Snøhvit area, these cycles of loading and unloading have caused extensive fracture development within cap rocks, leading to hydrocarbon leakage from traps, out of proven hydrocarbon reservoirs and fluid migration along permeable carrier beds (Tasianas et al., 2016).

In the Hammerfest Basin, residual oil columns found beneath gas fields indicate that these structures earlier were oil bearing. The extensive removal of the sedimentary overburden has had critical consequences for hydrocarbon accumulations. Exsolution of gas from the oil and expansion of the gas, due to the decrease in pressure, resulted in massive expulsion of oil from the traps. Seal breaching and spillage probably also occurred as a result of the following uplift and tilting. (Jan I. Faleide et al., 1993).

3.4 Evolution of the Hammerfest basin

The Hammerfest basin is situated in the southwestern part of the Barents Sea, to the north-west of the Norwegian mainland, approximately 100 kilometers to the north of Hammerfest. It is a 70 km wide and 150 km long sedimentary basin (L. T. Berglund et al., 1986), which is separated from the Finnmark Platform area to the south, the deeper Tromsø Basin to the west and the Loppa High to the north, separated by the Asterias fault complex (**Figure 3-1**). It is a relatively shallow, fault controlled basin, which stretches in an east-west direction. The Hammerfest Basin was probably established during the Early to Late Carboniferous rifting, and developed into a more mature basin in connection with fault activity and uplift in the Late Jurassic-Early Cretaceous (L. Berglund et al., 1986; Gabrielsen et al., 1990).

Due to separate basin subsidence in the northeastern and southwestern part, the Hammerfest Basin is divided into east and west sub-basins (L. Berglund et al., 1986), separated by the extension of the W-NW oriented Trollfjord-Komagelv fault trend, which was reactivated in Late Jurassic times (L. Berglund et al., 1986; Gabrielsen et al., 1990). The geometry of the faults and the central dome along the basin are most likely remnant of late Jurassic tectonism (Larssen et al., 2002; Linjordet et al., 1992). Even if the basin most likely established in late Carboniferous, the main subsidence and formation of present tectonic features occurred later, in Triassic to early Cretaceous (Larssen et al., 2002). The basin development peaked probably around mid-Cretaceous. A thin condensed section of shales from late Cretaceous and Early Tertiary is preserved, in spite of the Tertiary uplift (Larssen et al., 2002).

The different Permian basin subsidence in the east and the west resulted in the presence of two different depocenters in the Early Triassic, when the subsidence turned quieter (L. Berglund et al., 1986). Subsequently, Triassic and Jurassic sequences were deposited under influence from shifting sea level and sediment input conditions. Later, these deposits were covered by thick Cretaceous and Tertiary clastic deposits (L. Berglund et al., 1986). The mid Jurassic deposition represents a change from sandstones to shales across the Bathonian–Callovian unconformity (Breivik et al., 1998), and sea level rise during mid Jurassic led to the deposition of the Stø Formation (Breivik et al., 1998) (**Figure 3-3**), which is the main reservoir unit in the Snøhvit Field. The Late Triassic sequence was deposited during a setting of high sea level, containing the Olderfjord formation (today named Hekkingen) (**Figure 3-3**), the most important hydrocarbon source rock in the Hammerfest Basin (L. Berglund et al., 1986). Depending on location, this source rock matured, ranging from late oil-early gas to early oil window when overlain by thick Paleocene and Eocene sequences (L. Berglund et al., 1986).

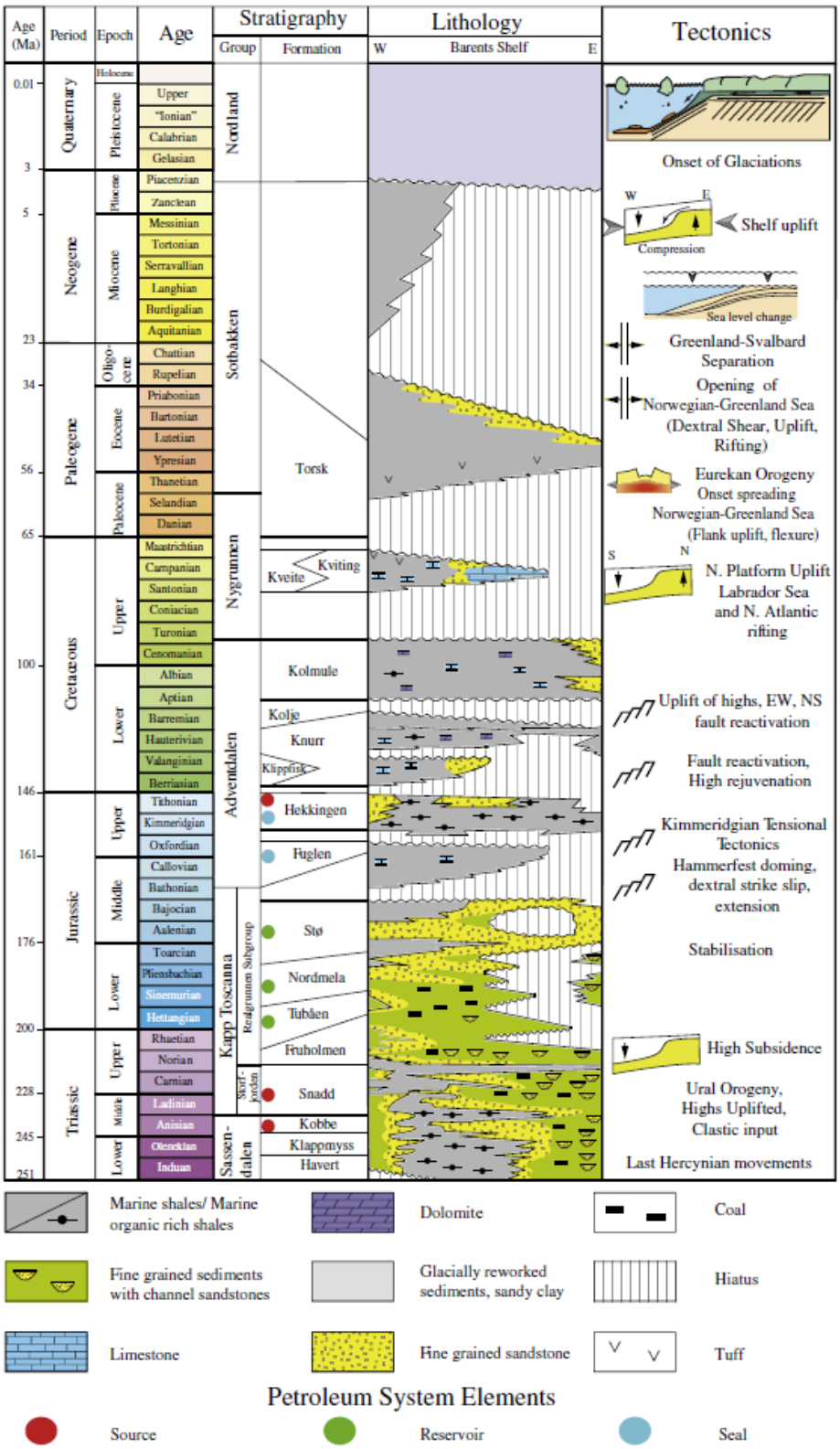

Figure 3-3 Stratigraphy of the Hammerfest Basin showing source and reservoir rock and major tectonic events. From (Ostanin et al., 2012).

3.5 Petroleum system in Snøhvit

Source rocks

Hekkingen, Nordmela, Snadd and Kobbe Formations represent the potential source rocks in Snøhvit (Linjordet et al., 1992). The late Jurassic Hekkingen Formation is considered the main source rock, despite the limitation from the underlying seal rock (Fuglen Formation). It was deposited in a marine environment, dominated by organic rocks which has reached the oil window (Linjordet et al., 1992; Ohm et al., 2008). This formation is commonly found as dark grey organic rich shales with some minor intervals of sandstone (Dalland, 1988).

The early Jurassic Nordmela formation is a clay-rich terrestrial-deposited source rock (Linjordet et al., 1992), accumulated in a near coastal climate, influenced by tidal- and flood plain environments (Dalland, 1988). This formation consists of siltstones, shales, coals and sandstone, which becomes more common towards the top. The Nordmela Formation has less variation in maturity and organic matter than the Hekkingen Formation, and the identified Snøhvit oil wax was probably generated from this formation (Linjordet et al., 1992). In the Snøhvit area, the observed shallow gas anomalies could be a result of large volume gas migration form the Triassic source rocks, and also from an upward migration of gas from the Hekkingen Formation, caused by lack of top seal layers (Duran et al., 2013b).

Reservoir rocks

The main reservoir rocks are the Jurassic Stø, Nordmela and Tubåen Formations, with Stø as the main producing formation. It is dominated by relatively well-sorted mature sandstones, deposited in prograding coastal regimes. A fining upwards trend is recognized, and pebbly sandstones beds identified within this interval (L. Berglund et al., 1986). Core data from well 7121/4-1 shows good reservoir properties, with porosities up to 17 % and permeabilities up to 500 mD. The upper and lower parts of Tubåen Formation is dominated by sandstones while the middle part is more shaly, probably deposited in high energy, marginal marine environment and related to tidal and/or estuarine facies (Dalland, 1988).

Seal rocks

The Jurassic Fuglen and upper part of the Hekkingen Formations represent the reservoir seal rocks. These formations mark a change in the depositional style compared to the underlying. The Fuglen Formation consists of pyritic mudstones with interbedded thin brownish limestones, and was deposited in marine environments during high sea level with ongoing tectonic movements. It contains less marine environment than the Hekkingen Formation (Dalland, 1988).

4 Data and method

4.1 Dataset

This study is based on interpretation of the FINAL MIG dataset from the seismic survey ST14M02 **(Figure 4-1)**. The survey is a post stack, multi-azimuth 3D survey, shot by CGG for Statoil in the Snøhvit area in 2014, released in September 2016. The covered area is approximately 270km^2, with inline direction from west to north ranging from 1942 – 4340 (inc 1) and crossline direction from south to north ranging from 12001-12735 (inc 1). The dataset has a bin size (inline x crossline) of 12,5 x 12,5m with sample interval of 4 ms. The survey was shot in an area of good well control, and provides good fault/horizon imaging due to the high resolution.

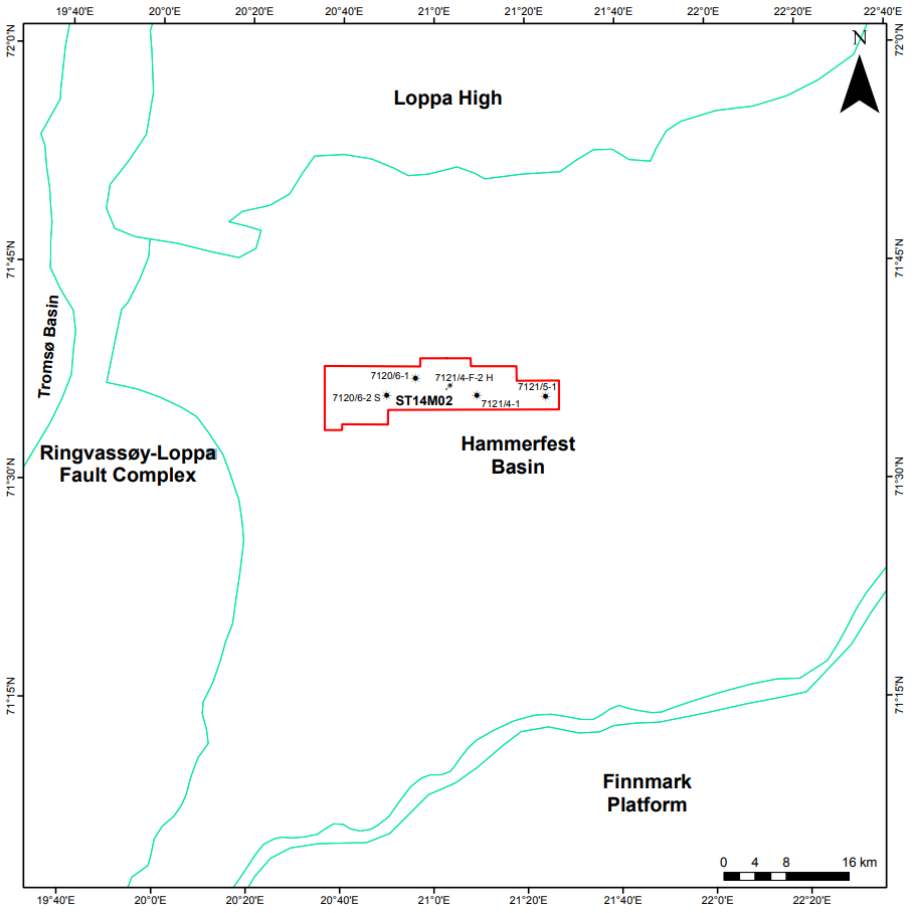

Figure 4-1 Location of seismic cube, including available wells and injection well 7121/-F-2-H.

The dataset is processed with a zero phase, normal polarity (SEG standard), meaning that a peak will correspond to an increase in acoustic impedance **(Figure 4-2)** (Andreassen, 2009).

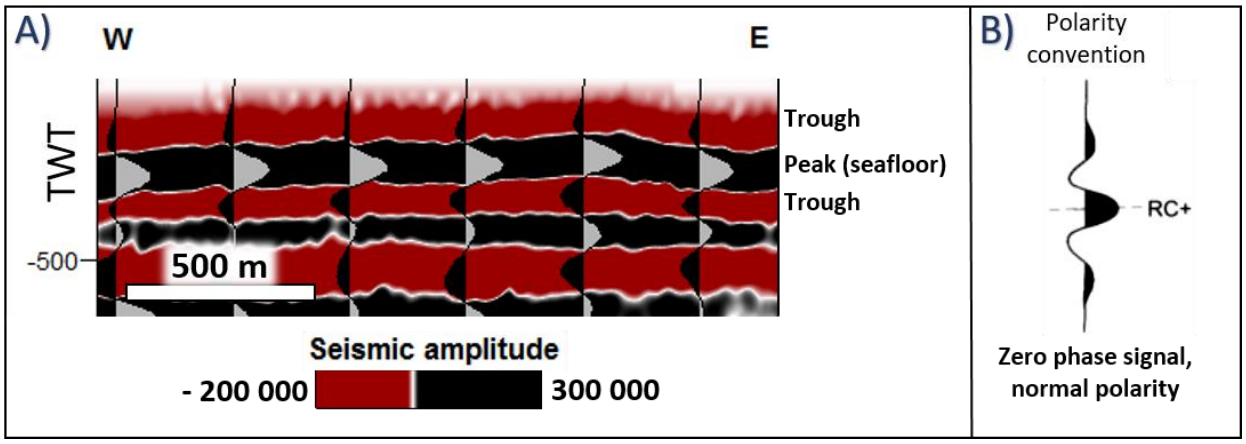

Figure 4-2 A) Seismic vertical profile with corresponding wiggle display of dataset ST14M02 showing the seafloor reflection appearing as a peak (grey). Crossline 12415. **B)** SEG standard polarity convention model from R. E. Sheriff (2002) applied in this study. Zero phase signal, normal polarity.

4.2 Resolution in dataset ST14M02

The velocity increases with depth, whilst the frequency decreases making the vertical resolution poorer with depth **(Table 4-1)**. The average velocities in each sequence are found in the sonic log from available wells, and the frequencies are gathered using the inspector tool and its frequency spectrum in Petrel.

Table 4-1 Frequencies, seismic velocities, wavelengths and vertical resolution of the seismic horizons in the area.

Sequence (horizon - horizon)	**Peak Frequency** (Hz)	**Seismic velocity** (m/s)	**Wavelength**	**Vertical Resolution** (m)
S8 (Kolmule URU)	30,13	2370	78,66	19,66
S7 (Kolje - Kolmule)	26,22	2730	104,12	26,03
S6 (Knurr - Kolje)	25,86	2964	114,62	28,65
S4-S5 (Fruholmen - Knurr)	23,65	3084	130,4	32,6
S1-S3 (DH1 - Fruholmen)	17,03	3625	212,86	53,21

The horizontal resolution in the 3D migrated volume is the same as inline and crossline spacing, found to be 12.5 meters.

4.3 Well data

The wells used in this study are the exploration wells 7120/6-1, 7120/6-2S, 7121/5-1 and 7121/4-1, and the CO2 injection well 7121/4-F-2H. Location in **Figure 4-3** and information in **Table 4-2.** All exploration wells are plugged and abandoned, and the well data is displayed in MD, meaning that the Kelly bushing elevation is included. Available logs applied in this study include the gamma ray (GR), sonic (AC), density (DEN), neutron (NEU) and resistivity (RDEP) log.

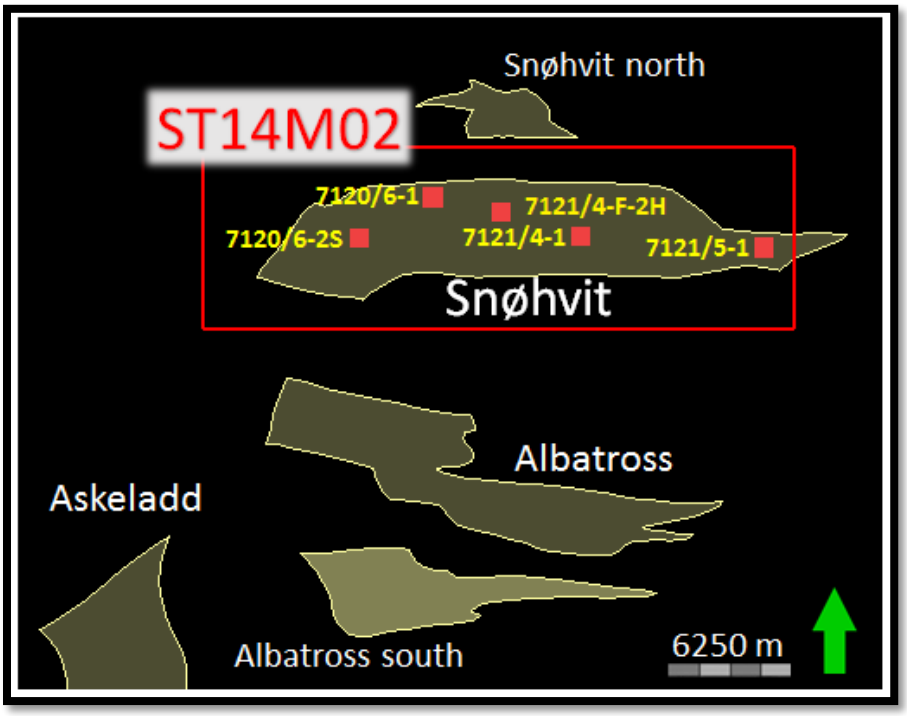

Figure 4-3 Close-up of seismic survey ST14M02 (red rectangle) including the location of the wells used in this paper and surrounding fields in the Hammerfest Basin.

Well 7120/6-1

7120/6-1 is a vertical exploration well, drilled by Norsk Hydro in 1985 as an oil and gas well, to a total depth of 2820 meters. It is located in the northwestern Snøhvit field **(Figure 4-3)**, with water depth reaching 314 meters. The scope of the well was to evaluate the potential hydrocarbon bearing sand sequences in the Middle Jurassic Stø Formation, and to evaluate the development of structure and stratigraphic trends in the Hammerfest Basin. Deepest penetrated formation is the Tubåen fm. in the late Triassic age, and first level of discovered hydrocarbons was found in early Jurassic.

Well 7120/6-2S

7120/6-2 S is a deviated well, drilled by Statoil in 2007, also as an oil and gas well. The total depth is 3242 meters, with water depth of 321 meters. Deepest penetrated formation is the Snadd fm. in late Triassic age, and first level of discovered hydrocarbons was the Stø formation. The aim of this well was to prove the presence of oil in the sandy sediments within Stø, and to find larger gas volumes than previously calculated.

Well 7121/4-1

Statoil drilled 7121/4-1 in 1984 to a total depth of 2609 meters. The purpose of the well was to test hydrocarbon accumulations in middle to early Jurassic sandstones. It turned out to display gas above oil in the upper sequence (Stø and Nordmela) between 2318 and 2442 meters, while the lower sequence (Tubåen) was gas bearing from 2468 to 2473 meters. This is the first discovery well of the Snøhvit hydrocarbon field.

Well 7121/5-1

7121/5-1 is an appraisal well drilled the year after 7121/4-1, in the eastern part of the Snøhvit field **(Figure 4-3),** down to a total depth of 3200 meters. According to the operator Statoil, the primary purpose of the well was to further test hydrocarbon accumulations in middle to early Jurassic sandstones, seen in the neighboring wells. The well displayed hydrocarbons in Stø formation at 2369 meters, but the secondary Triassic target only gave some weak shows in Snadd formation.

Injection well 7121/4-F-2 H

The CO_2 injection well 7121/4-F-2 H is 2906 meters long, and was drilled in 2004 to a vertical depth of 2795 meters, and has been injecting CO_2 in the Snøhvit field since 2008.

Table 4-2 Wells used in this study

Well	Operator	Year	Water depth (m)	Total depth (m RKB)	Oldest Formation	Type
7120/6-1	Norsk Hydro	1985	314	2820	Tubåen	Exploration
7120/6-2S	Statoil	2007	321	3242	Snadd	Exploration
7121/4-1	Statoil	1984	335	2609	Fruholmen	Exploration
7121/5-1	Statoil	1985	336	3200	Snadd	Exploration
7121/4-F-2H	Statoil	2008	318	2906	Tubåen	Injection

4.4 Seismic interpretation

4.4.1 Petrel Software

Interpretation of well-log data and 3D seismic was carried out using Schlumberger's Petrel software by:

- Identification of main stratigraphic units and formations in the basin.
- Interpretation of key reflections to produce maps used for extraction of advance seismic attributes.
- Identification of fluid-flow related features like bright spots, gas pipes and chimneys, potential gas hydrate indicators, pockmarks etc.
- Correlation between seismic and well-log data

4.4.2 RMS amplitude

The RMS attribute (Root Mean Square) measures the average amplitude value for a given interval in the seismic. This attribute calculates the square root of the sum of the squared amplitudes, divided by the number of samples in the chosen interval (Brown et al., 1996). In this way, some of the seismic amplitudes get clearer, allowing morphological structures with acoustic impedance contrast to become more visible. This is a good tool for finding possible hydrocarbon accumulations, or other geological structures with high-density contrasts.

4.4.3 Variance

The variance method is a three dimensional attribute estimating the local variation between different traces for a given interval (Brown et al., 1996). This tool highlights the structural and stratigraphic boundaries, such as different deposits, faults and areas with acoustic masking.

4.4.4 Thickness map

To display the thickness variations between layers in the subsurface, thickness maps are useful. The interpretation of these attribute maps can provide important information about the depositional environment, hydrocarbon accumulation trends, thickening/thinning layers etc. The Petrel software gives the opportunity to choose between vertical thickness maps, isochores (measured in depth) and time thickness maps, isochrones (measured in the time domain). For this study the latter was chosen, and thickness maps were made between all the interpreted sequences.

4.5 Application of an analytical model for estimating leakage through faults

Zahasky et al. (2014) developed a simple analytical model for estimating leakage of carbon dioxide through faults. This model is used as a quick screening of the risk of a storage site and determine the potential leakage rates from a given system. With only basic knowledge of the systems geometry and permeability, this solution provides a good first order analyses of potential CO_2 leakage rates, and acts as a suitable starting point finding out which parameters that are most important for leakage through faults.

Figure 4-4 shows the conceptual geometry of the model of CO_2 injected into the reservoir. After some time, the CO_2 plume intersects a finite fault zone length, which allows CO_2 to flow into the overlaying aquifer. This concept assumes that the injected fluid partitions itself into two flow paths; one that stays in the reservoir and one that travels up the fault, and then move radially away from the fault in the upper aquifer.

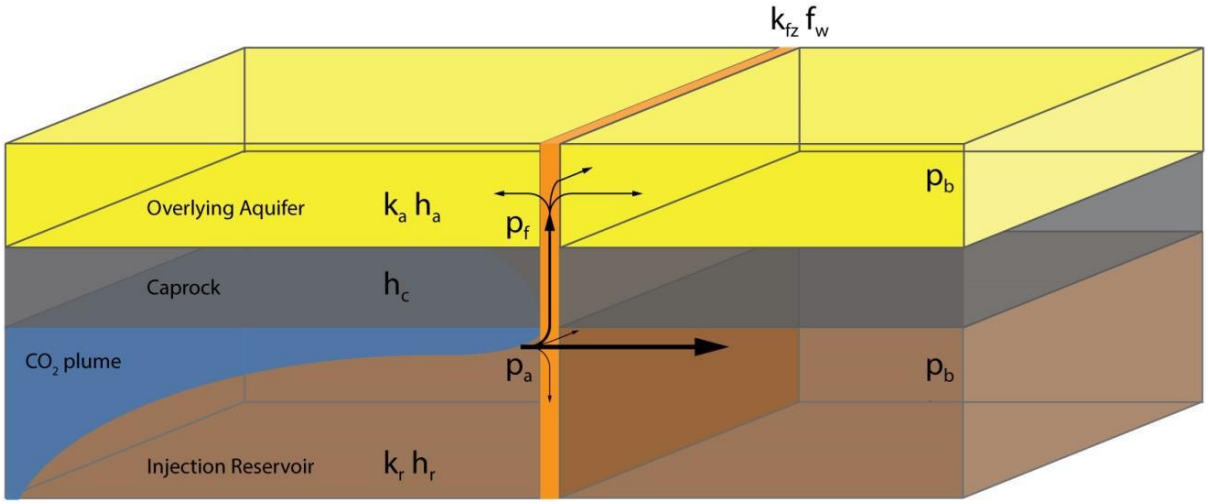

Figure 4-4 Schematic sketch of a system with leakage of CO2 from the injection well into the reservoir, followed by fluid migration through a fault zone to the overlying aquifer. From (Zahasky et al., 2014). Parameters listed in **Table 4-3**

The analytical expression developed by Zahasky et al. (2014), is

$$q_a = \frac{q_r}{2\pi k_r h_r}\ln(r_{br}/r_a)\Bigg/\left(\frac{h_c}{k_{fz}f_w f_l}+\frac{\ln((r_{ba}-r_a)/r_f)}{2\pi k_a h_a}\right) \qquad \textbf{(Equation 2-9)}$$

Where included parameters are listed in **Table 4-3** below.

Table 4-3 Parameters included in the schematic sketch in **Figure 4-4** and **Equation 2-9**

$\mathbf{q_a}$	flow rate into the aquifer (m/s)	$\mathbf{k_{fz}}$	permeability in the fault zone (m^2)
$\mathbf{q_r}$	flow rate of the injected fluid (m/s)	$\mathbf{f_w}$	fault width (m)
$\mathbf{h_r}$	height of the reservoir (m)	$\mathbf{f_l}$	fault length (m)
$\mathbf{k_r}$	permeability in the reservoir (m^2)	$\mathbf{h_a}$	thickness of the overlaying aquifer (m^2)
$\mathbf{r_{ba}}$	extent of pressure response in aquifer (m)	$\mathbf{p_a}$	pressure at base of fault (Pa)
$\mathbf{r_a}$	fault distance for injection well (m)	$\mathbf{p_f}$	pressure at the top of the fault (Pa)
$\mathbf{r_f}$	equivalent radius to fault (m)	$\mathbf{p_b}$	pressure at model boundary (Pa)
$\mathbf{h_c}$	thickness of the cap rock (m)	$\mathbf{k_a}$	permeability of the overlaying aquifer (m^2)
$\mathbf{r_{br}}$	extend of pressure response in reservoir (m)		

The leakage factor, L is then presented by

$$L = \frac{q_a}{q_a + q_r} \qquad \textbf{(Equation 2-10)}$$

L = leak off fraction q_a = flow rate into the aquifer (m/s) q_r = flow rate of the injected fluid (m/s)

The derivation of the equations starts by combining Darcy's law (equation 2.1) to the general pressure equation. The complete derivation of the equation can be found in **Appendix A**. Three key assumptions are made. First, the system is in steady state, which is valid for a system that has been injected for a long period of time with constant leakage into the aquifer. Secondly, it is assumed that the fluid and the rock in the fault is incompressible, which is valid when CO_2 is injected in a supercritical state. Due to the reservoir pressures and temperature, this is the case on Snøhvit, see **Figure 4-5**. Thirdly, it is assumed radial flow in the aquifer, which is a good approximation when the fault length is small relative to the size of the leakage plume in the overlaying aquifer. Zahasky et al. (2014) compared the results from the analytical equation with the results from a simulation model, and concluded that the analytical expression agrees well with the simulation results at leakage rates less than 10% of the total CO_2 injected.

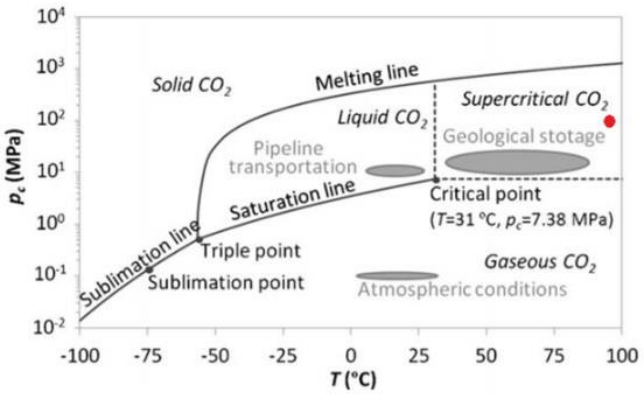

Figure 4-5 Phase diagram for CO_2 together with the Snøhvit reservoir properties (red dot). Modified from (Vilarrasa et al., 2013)

4.5.1 Parameters used in analytical model

Data from the Snøhvit field is applied to the analytical model from Zahasky et al. (2014) as a quick screening of the leakage potential of injected CO_2, from the reservoir through faults seen on seismic and into overlying units with portions of sand in the overburden. This will be used to observe if faults close to the injector has leakage potential, and will potentially say something about the leak off potential as off today. During the drilling of the 7121/6-1 well, sands was observed within the Hekkingen formation, according to the completion report and available log data. Therefore, the overburden sand in this screening will be within the Hekkingen formation.

For thickness of the reservoir, caprock and overburden, the average from the four available exploration wells nearby the F-2 gas injector is used, see **Figure 4-3** and **Table 4-4**. Here, Stø is the reservoir, Fuglen is the caprock and sands within Hekkingen acts as the overlaying aquifer.

Table 4-4 Average thickness of the formations in the exploration wells closest to the F-2 CO2 injector

Thickness of the formations in the different exploration wells					
Formation/Exploration well	**7120/6-2 S**	**7120/6-1**	**7121/4-1**	**7121/5-1**	**Average thickness [m]**
Hekkingen	75.9	81.5	69.8	64.9	73.0
Fuglen	13.8	19.0	11.5	12.0	14.1
Stø	108.5	84.0	78.0	75.9	86.6

The reservoir properties in Stø used in the model is taken from the 7120/6-1 completion report and log, see **Table 4-5**. A weighted average is used, with porosity of 15.3 % and permeability of 325.8 mD. For the properties in the overlaying sand (Hekkingen) a porosity of 10 % and a permeability of 50 mD is assumed. The thickness of the sand is sat to 15 meters. These parameters will be varied in the sensitivity study **(5.5.2)**.

Table 4-5 Reservoir properties from the well 7120/6-1 completion report and log

CORE ANALYSIS RESULTS			
INTERVAL (matched to CPI) (mRKB)	2385.5-2402	2402-2427	2427-2442
Ø AV (%)	15.43	13.31	18.31
K AV (mD) (Arithmetric)	176.0	7.0	1022.0

Two faults located close to the F7121/F-2H CO_2 injector **(Figure 4-6)** are looked further into. One of them is placed at a distance 600 m from the injector, the other one is placed roughly 1800 meter apart. According to Zahasky et al. (2014) the fault zone permeability is between 1 and 10^{-9} mD. Hence, 1 mD is used for the leak off value of fault 1 and fault 2 and the fault zone permeability will be varied in the sensitivity study.

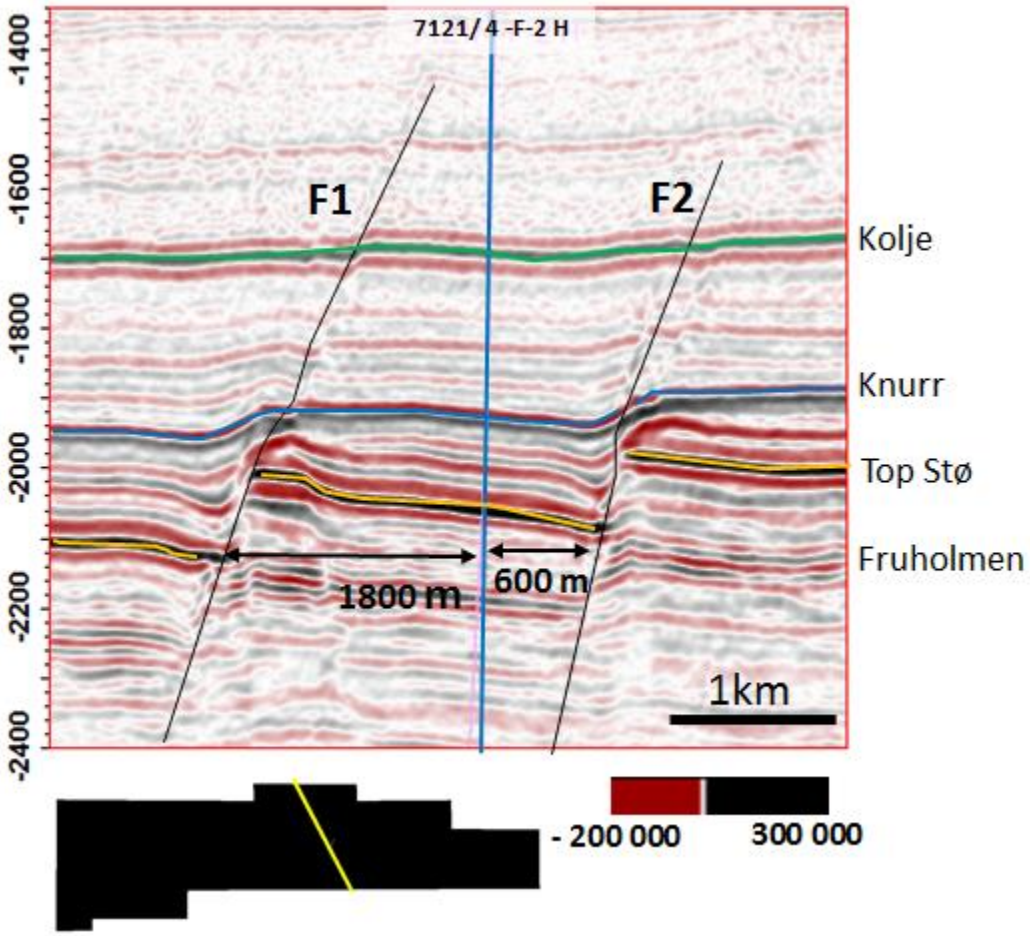

Figure 4-6 Distance from Co2 injector to Fault 1 and Fault 2

5 Observations and results

This chapter contains interpretations of features observed in the seismic dataset ST14M02, supplied with corresponding well log data from the area. Seismic indications of fluid migration and accumulation are analyzed using attribute maps from key horizons presented here. The objective is to interpret high amplitudes observed in shallow parts of the subsurface and to determine whether it is actually gas or just lithology contrasts. If it turns out to be hydrocarbons, the next step is to find any correlation with the large chimneys beneath and deeper structures, and to determine the origin and migration mechanisms controlling the fluid flow, which is the objective for the next chapters.

5.1 Stratigraphy of study area (Interpreted horizons and sequences)

To provide interesting and meaningful maps, some key horizons have been interpreted (**Figure 5-1**). These are chosen based on strong, continuous reflections in the seismic in correlation with four available wells in the area. In order to describe the stratigraphy, the vertical section is divided into eight different sequences based on these interpreted horizons, termed S1 – S8 (**Figure 5-1**). The characteristics of each sequence is given in the following section, as well as a brief description of morphology features on the seafloor and interpreted URU (Upper Regional Unconformity).

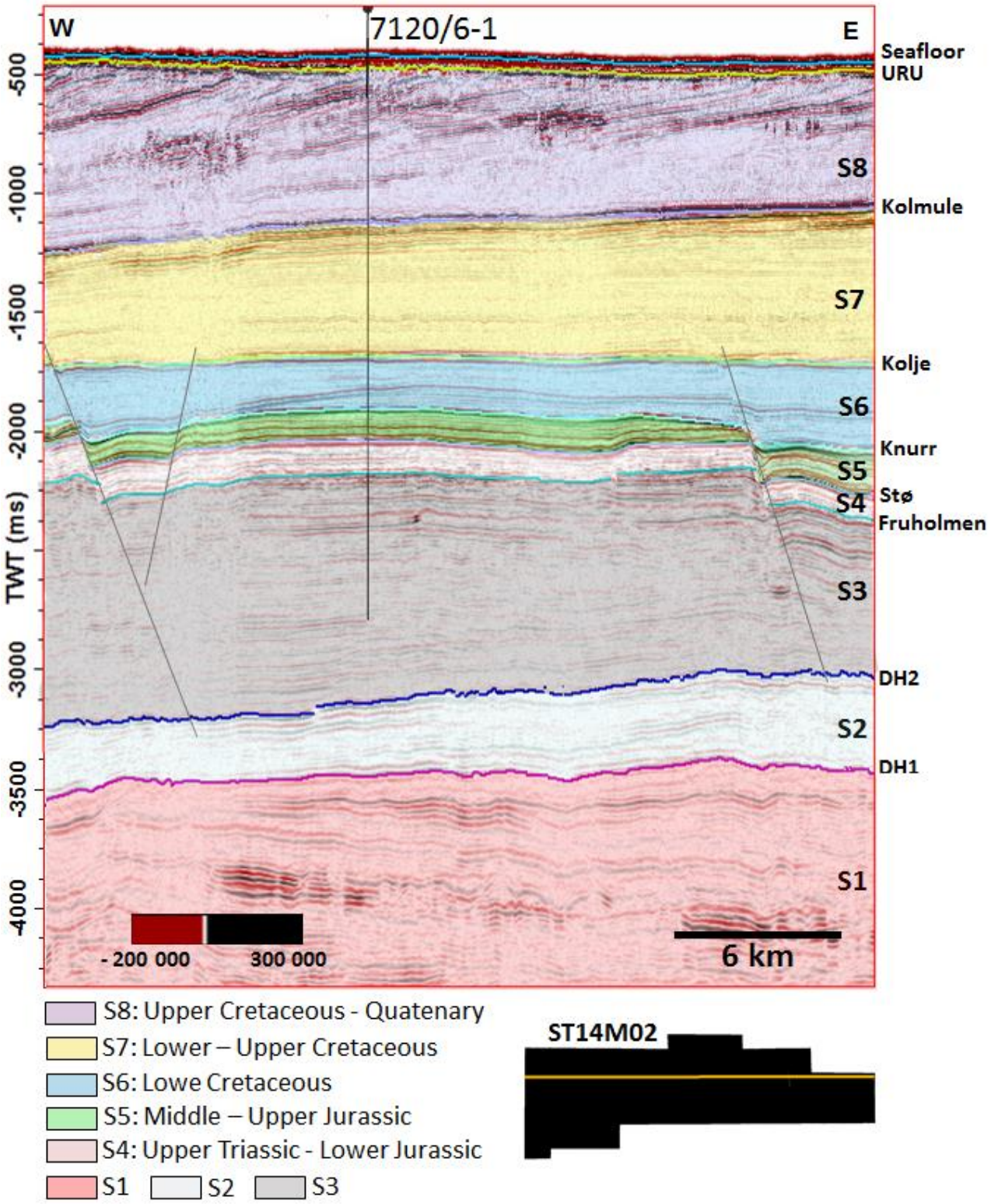

Figure 5-1 Overview showing all the interpreted horizons and subdivided sequences applied in this study. Vertical section from crossline 12484 in the dataset ST14M02. S1, S2 and S3 not defined in age due to the lack of well log data. 7120/6-1 is the well penetrating this section.

5.1.1 Sequence 1 - 8

The petrophysical properties of each described sequence are collected from available logs in well 7120/6-1, 7120/6-2S, 7121/5-1 and 7121/4-1. Information is mainly provided from the sonic (AC), neutron (NEU), density (DEN), gamma ray (GR) and resistivity (RDEP) logs, seen from well 7120/6-1 in **Figure 5-2**. The characteristic trends in the well logs is described from top to bottom. Notice the general increase in velocity and the shift in gamma ray, density/neutron and resistivity from S5 to S4.

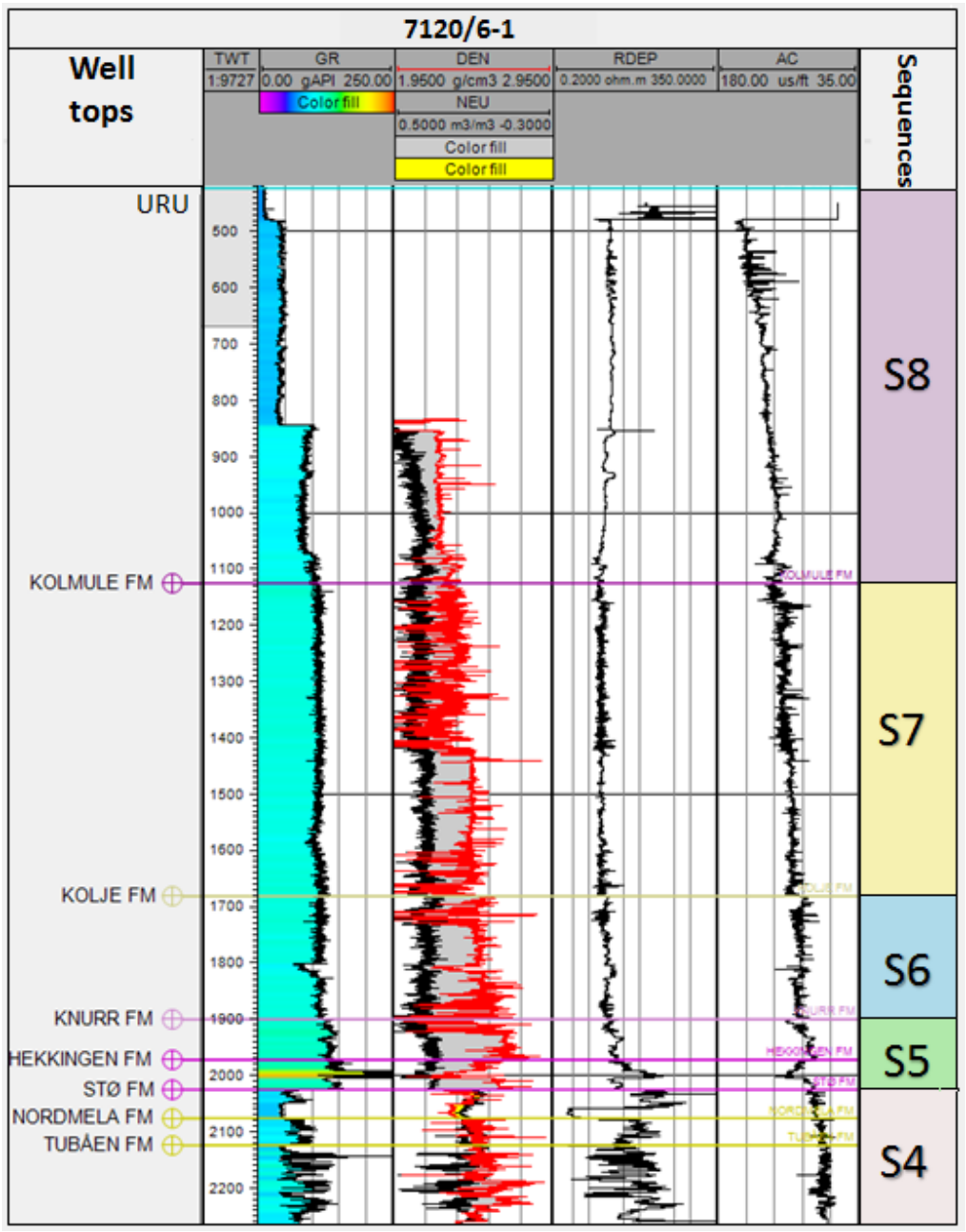

Figure 5-2 Main interpreted logs from well 7121/6-1. GR = Gamma Ray, DEN = Density, NEU = Neutron, RDEP = Resistivity, Ac = Sonic log. Notice that the AC log is measured in µs/ft.

Sequence 1, 2 and 3

The two deepest sequences in this study are marked by horizons DH1 and DH2 (**Figure 5-3A**), interpreted at around 3500 and 3200 ms (twt), respectively. None of these units are penetrated by the wells in this area, making it difficult to predict the exact ages and compositions. The third sequence (S3) is reached by all the available wells, showing that the Late Triassic Fruholmen is the top formation in this unit. The thickness seems to decrease slightly towards east (**Figure 5-3B**), opposite to the trend in S2, where the thickness is increasing in the same direction (**Figure 5-3C**). The average thickness in S3 is 850-1000 ms (twt), while S2, having an average thickness of 250-400 ms (twt) is thinner throughout the sequence. In the seismic section, S1 is characterized by continuous reflections and high amplitudes, while S2 and S3 have weaker, more discontinuous reflections, with only a few areas of high amplitudes. Most of the deep-seated faults interpreted in this study are observed in these sequences, and looks to bend at the top of S3.

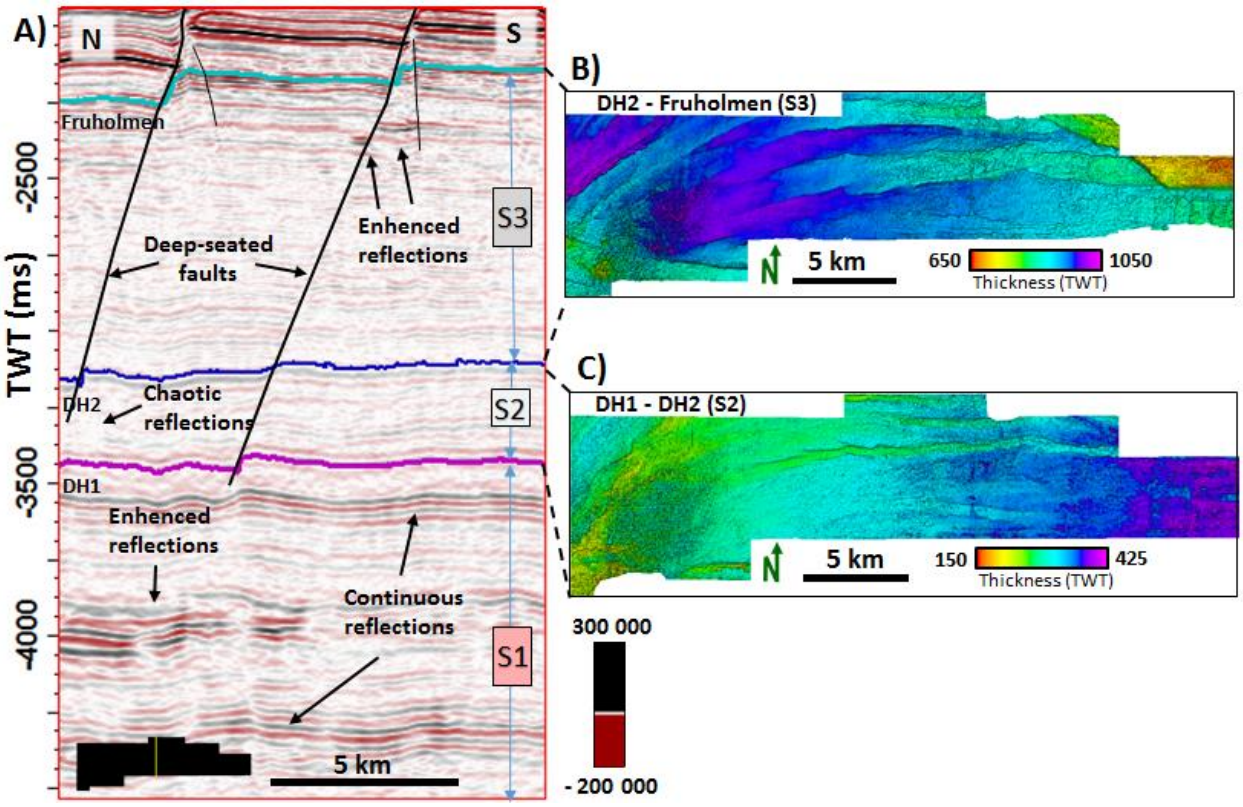

Figure 5-3 A) Seismic stratigraphy of sequence S1, S2 and S3. Inline 3250. **B)** Isochron thickness map between DH2 and Fruholmen (S3). **C)** Isochron thickness map between the two deepest horizons DH2 and DH1 (S2).

Sequence 4

Entering the reservoir zone, sequence 4 (S4) consists of formation tops visible in the wells, bounded by top Fruholmen and Top Stø Fm. The seismic section (**Figure 5-4A**) indicates a lot of faulting and chaotic, discontinuous reflections, and is affected by a large area of acoustic masking in the west.

The thickness map in **Figure 5-4B** shows a quite uniform pattern, averaging from 100 to 150 ms (twt) throughout the section. The highest and lowest values are related to the acoustic masking and penetrating faults, respectively.

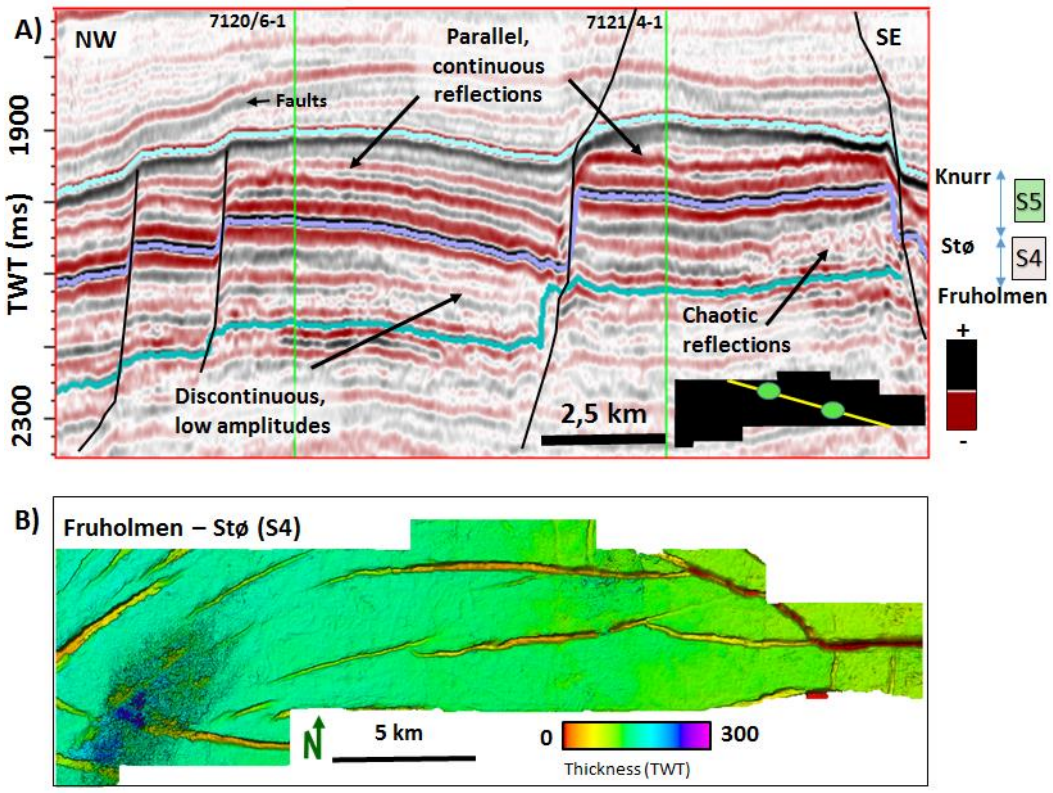

Figure 5-4 A) Seismic section visualizing the reflection characteristics in sequence 4 and 5. Random line, location in black figure. **B)** Thickness map between Fruholmen and top Stø (sequence 4).

Tubåen, Nordmela and Stø are the main formations in this sequence, and logs from available wells show unique characteristics for each sequence. The most interesting trends were found from the gamma ray, density, neutron and resistivity logs, collected from well 7121/4-1 **(Figure 5-5)**.

Throughout the interval of S4 the gamma ray shows relatively small values compared to adjacent horizons, but there is also observed internal alterations. Some very low GR are identified, significant lower than the general low rates in the sequence. In this section, these will be separated by "low" and "high" gamma rays, for simplicity. The low values seem to correlate with a decreasing trend in bulk density and neutron porosity, creating the yellow infills in **Figure 5-5.** This occurs when the density and

neutron crosses, causing an overlap (crossover). At higher values of both density and neutron, the infill is grey, which seems to be the case when the gamma ray in this section is high. In the low gamma ray, differentiations in resistivity between the upper and the lower regions are observed. In the upper unit, the resistivity log respond with increased values, whereas the lower part indicates a decrease, shaded in red and blue in **Figure 5-5**, respectively. The sonic log showed little, or no trends in velocity throughout the sequence, and was not included in the figure.

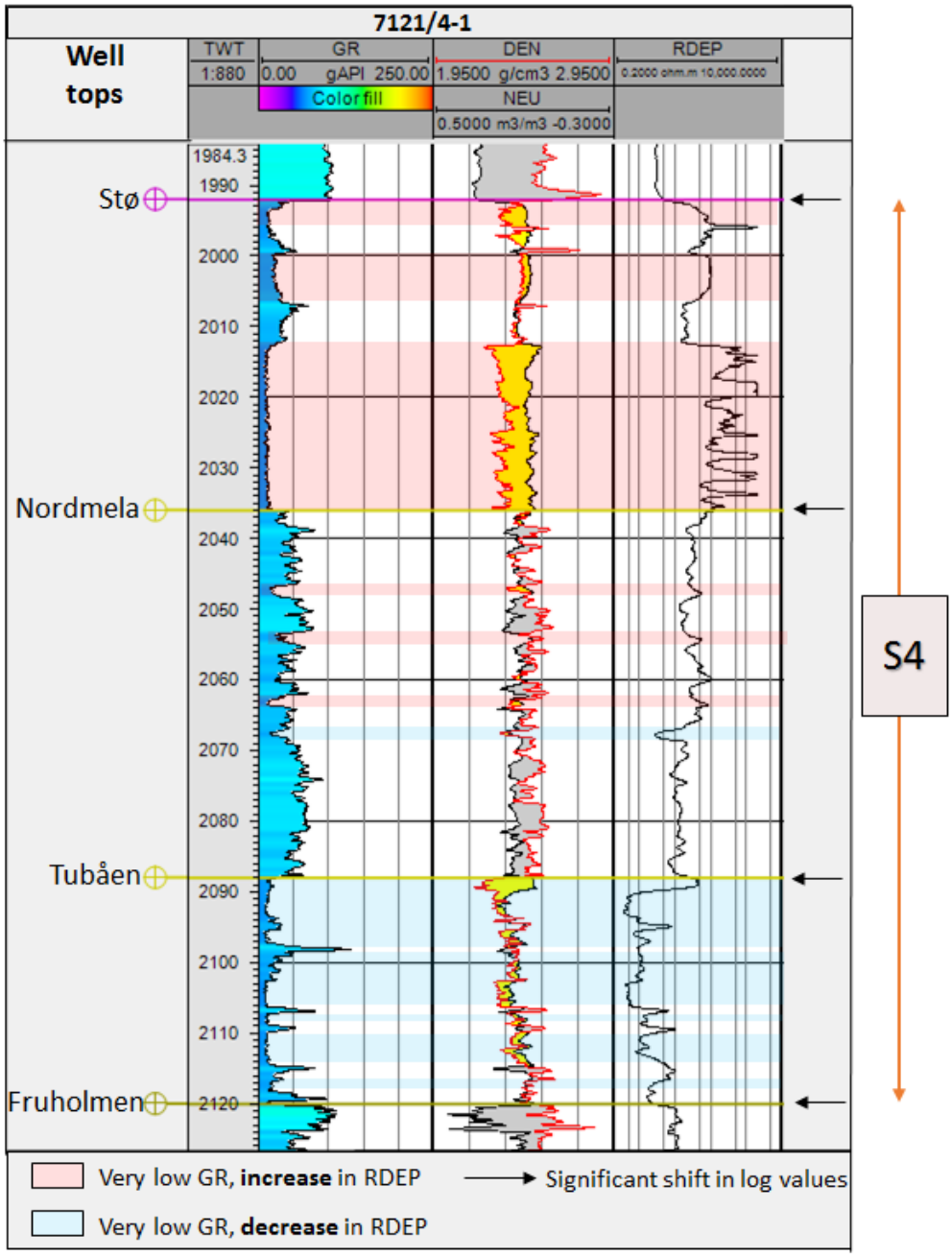

Figure 5-5 Main logs from well 7121/4-1 in the reservoir sequence (S4)

Sequence 5

Sequence 5 consists of middle to late Jurassic sediments, from top Stø to top Knurr formation, including Fuglen, Hekkingen and Knurr, listed from the deepest formation. The reflections within this unit are bounded by faults, which is observed to be changing in dip direction within this sequence. Most of the reflections appear as parallel, continuous reflections within these dipping fault blocks (**Figure 5-4A**). The thickness map **(Figure 5-6)** shows slightly variations throughout the field, with the thinnest and thickest parts located in NW and SE respectively.

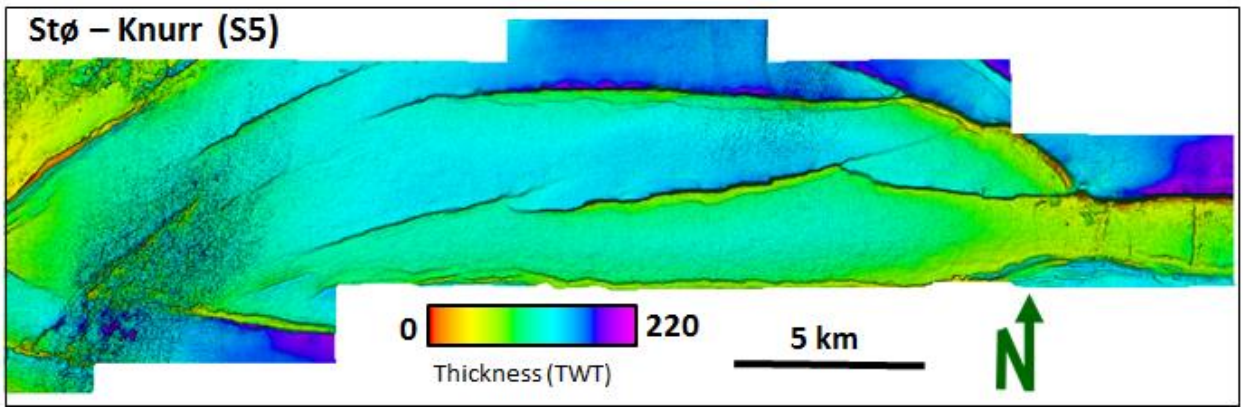

Figure 5-6 Isochron thickness map between Top Stø and Knurr, bounding sequence 5 (S5).

Comparing the well logs from sequence 4 and 5, the resistivity in S5 shows more stable values, there are no crossovers between neutron and density and the gamma ray values are significant higher in general **(Figure 5-7).** The most prominent shifts occur at around 1970 ms (twt), when entering the Hekkingen formation. The velocity and density decrease, while resistivity and neutron shows increased values. At approximately 1992 ms (twt), an even steeper gradient of decrease / increase occurs, correlating with the interval with increased gamma ray values. The shifting trends are located within the yellow shaded unit in **Figure 5-7.** Reaching Fuglen, the normal trends for this sequence are obtained. A stable, overall high gamma ray value, a more unstable, overall high density, increasing velocity and gradual decreasing neutron. The resistivity shows no specific trends outside the yellow shaded area.

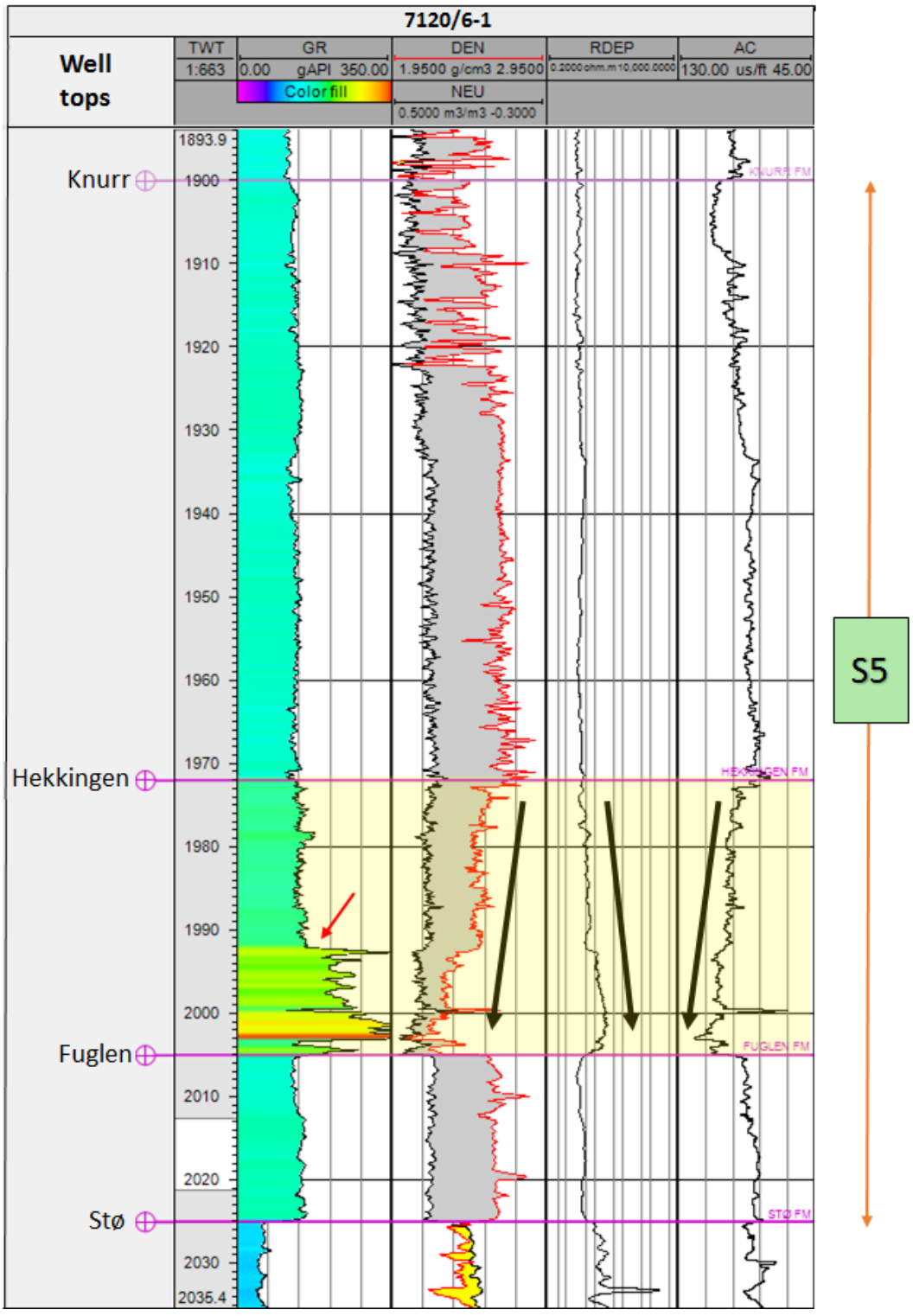

Figure 5-7 Main logs from well 7120/6-1 in sequence 5. Yellow shaded area indicates the interval with most sufficient shifts in values.

Sequence 6 and 7

The sequences S6 and S7 are characterized by weak reflections and areas of acoustic masking **(Figure 5-8A)**. Some continuous, dipping reflections are observed in the topmost part of the S7 and in the middle of S6. The thickness maps **(Figure 5-8B** and **Figure 5-8C)** show variations in thickness related to faults, which seem to change direction within these sequences. The early Cretaceous sediments in S7, have a thickening going from west to east, while S6 are thinnest in the middle, and tend to thicken towards the flanks. No specific trends were observed in available well logs.

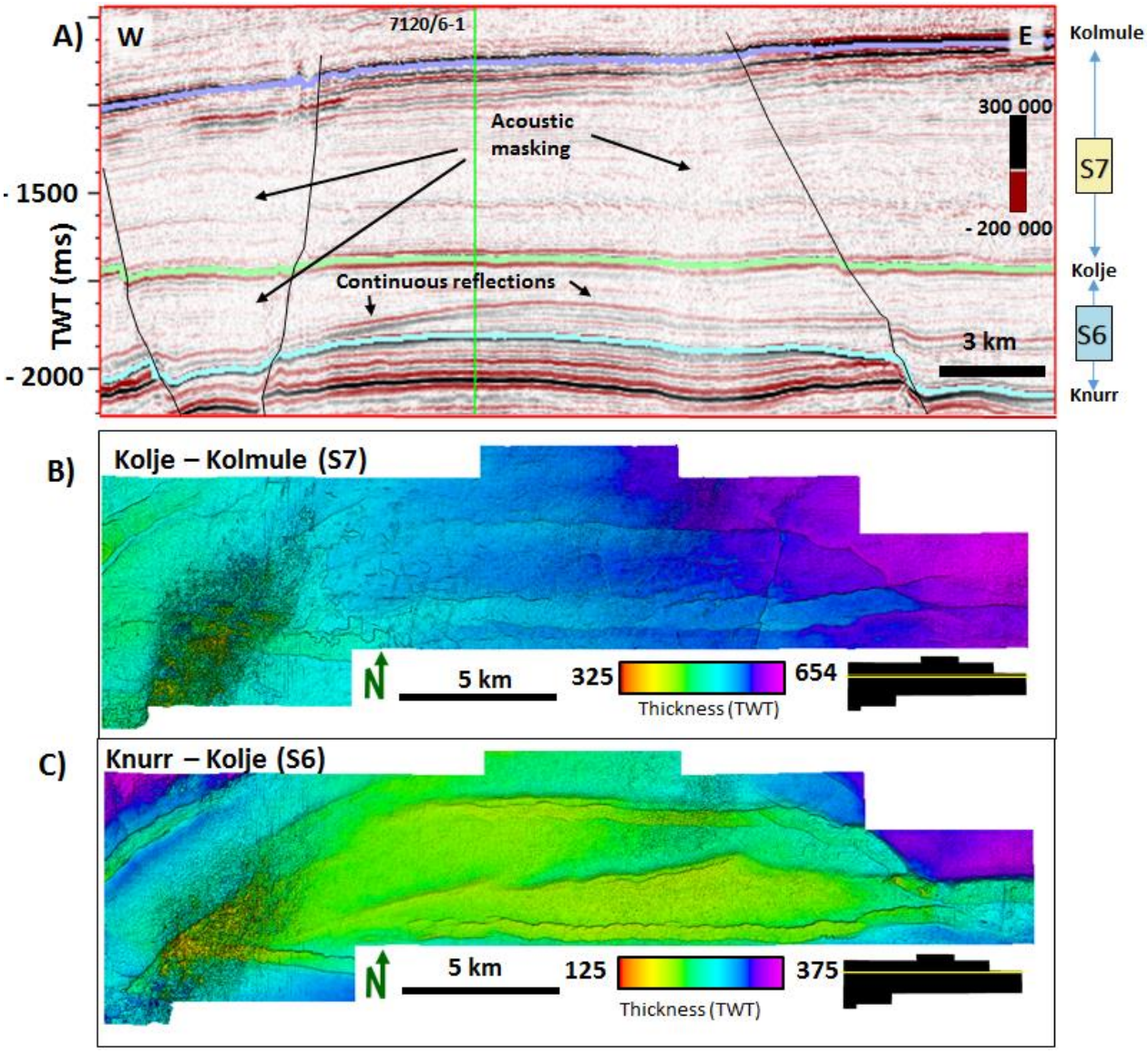

Figure 5-8 A) Seismic characteristics of the reflections in sequence 6 and 7, from crossline 12485. **B)** Thickness map of S7. **C)** Thickness attributed map between Knurr and Kolje (sequence 4).

Sequence 8

The package between the Early Cretaceous Kolmule formation and the upper regional unconformity (URU) is a relatively large sequence with a lot of interesting structures and amplitude anomalies. Areas of acoustic masking, enhanced reflections, faults and discontinuous, chaotic reflections are characteristics for this unit **(Figure 5-9A)**. All the high amplitude anomalies interpreted in this study are located in the upper part of this sequence. A network of faults is found in and above the upper Cretaceous Kolmule reflector, and some minor faults are also observed in the vicinity of the interpreted anomalies. The thickness attribute map **(Figure 5-9B)** shows a thinning trend from west to east. In the thickest part to the west, the two-way travel time passes 800 ms, whilst the thinnest part in the east only have a travel time around 575 ms (twt).

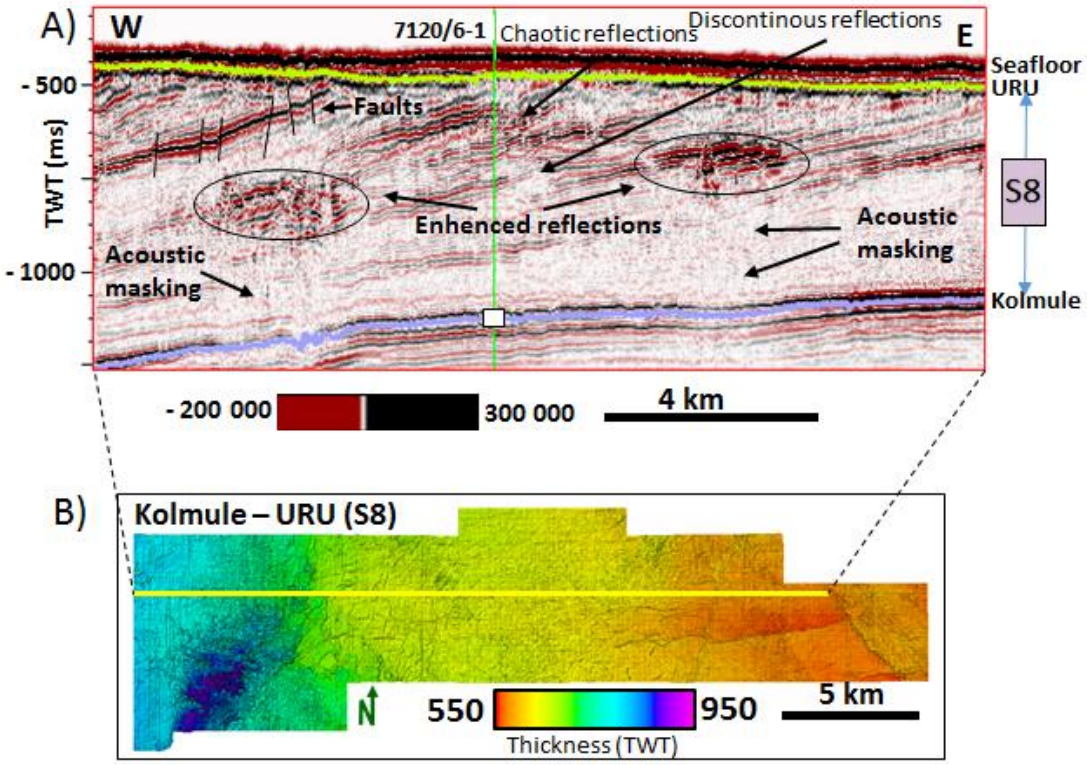

Figure 5-9 Sequence 8, bounded by Kolmule and URU (Upper Regional Unconformity). **A)** Seismic profile of crossline 12464 with seismic characteristics. **B)** Thickness variations in S8.

Log data collected from well 7121/5-1 show some interesting trends (**Figure 5-10**). In general, the velocity and density tend to increase, with several peaks throughout the sequence. At around 660 meters, a significant peak occur for the density, resistivity and sonic logs, shaded in red in the figure. Deeper down an interval with shift in log values is observed (green shaded area). This is a 28 ms (twt) window, between Kolmule and Kviting formations.

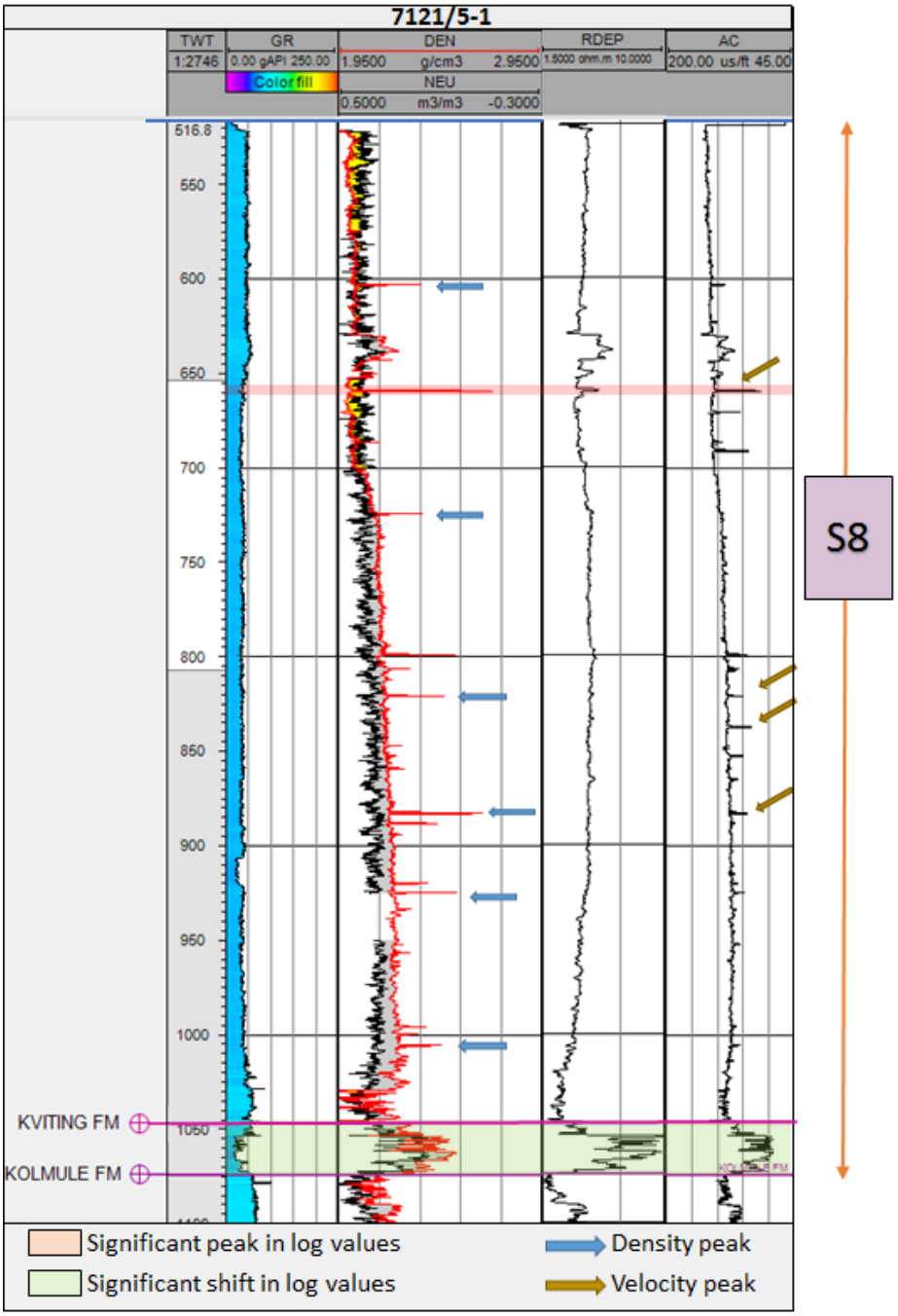

Figure 5-10 Main logs from well 7121/5-1 through the Upper Cretaceous – Cenozoic sequence, S8. Red and green shaded areas are discussed further.

5.1.2 Upper Regional Unconformity

The boundary separating Paleogene – Neogene sediments with overlying Quaternary glacial deposits is termed the Upper Regional Unconformity (URU). Several glaciations have affected the SW Barents Sea since the Pliocene (Laberg et al., 2012; Vorren et al., 1991), providing a highly erosive surface with depressions observed in the seismic **(Figure 5-11).** These interpreted pockmarks seem to be populated in two distinct areas, in the southwest and in the northern, central part. In the seismic section, the unconformity reflection appears with a high amplitude, with slightly varying distance to the seafloor **(Figure 5-11).**

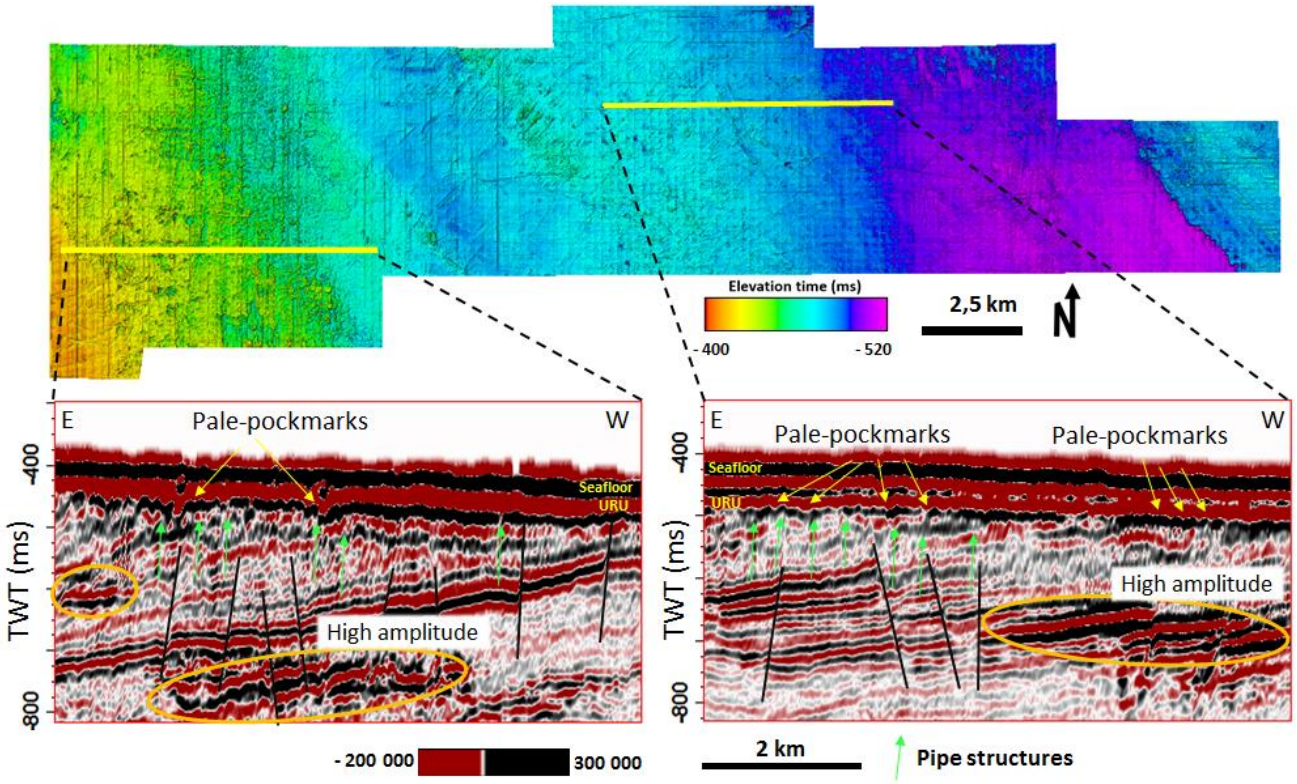

Figure 5-11 Time elevation map of the Upper Regional Unconformity with seismic sections from the yellow lines, showing paleo-pockmarks on the reflector. On the left hand side the URU coincides with the seafloor, while on the right hand side, another reflection is observed in between.

5.1.3 Seafloor

Several shapes of depressions, varying in length, width and relief, characterize the seafloor above the Snøhvit field in the Hammerfest Basin. The features are interpreted to be plough marks and scours or pockmarks, ranging from curved, elongated and linear shape to more circular and sub-circular outline, respectively **(Figure 5-12)**. The seabed ranges from 392 ms to 476 ms (twt), corresponding to approximately 290 – 352 meter below sea level, with a gradual increase in depth towards the east (**Figure 5-12)**. The study

area is, as described earlier, strongly affected by glacial erosion. The furrows and lineations imprinted on the seafloor are evidence of this, originating from current and wind-driven icebergs.

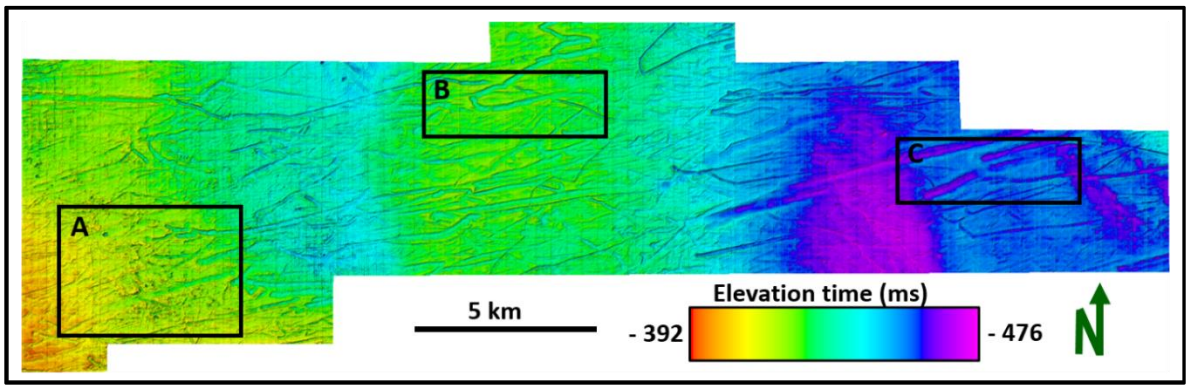

Figure 5-12 Map of the seabed contributed from the interpreted seafloor reflection. The morphology features observed indicates an ENE-WSW orientation. Elevation time measured in twt. Black squares indicate position of features shown in **Figure 5-13**.

The orientation of the furrows varies, and may even overlap, indicating several periods of calving ice. The prominent trend however, is observed in an ENE – WSW direction, giving a good approximation of the ice stream direction. The furrows in the study area vary significant in length, width and depth. The longest, widest and deepest features are measured to around 13 km, 200 meters and 10 meters, respectively. Some of the longest and most parallel furrows are located in the east **(Figure 5-13).** The western part is dominated by shorter and more chaotic depressions with surrounding pockmarks. These pockmarks are often found within iceberg furrows, and may originate from fluid seepage on the seabed, described later on.

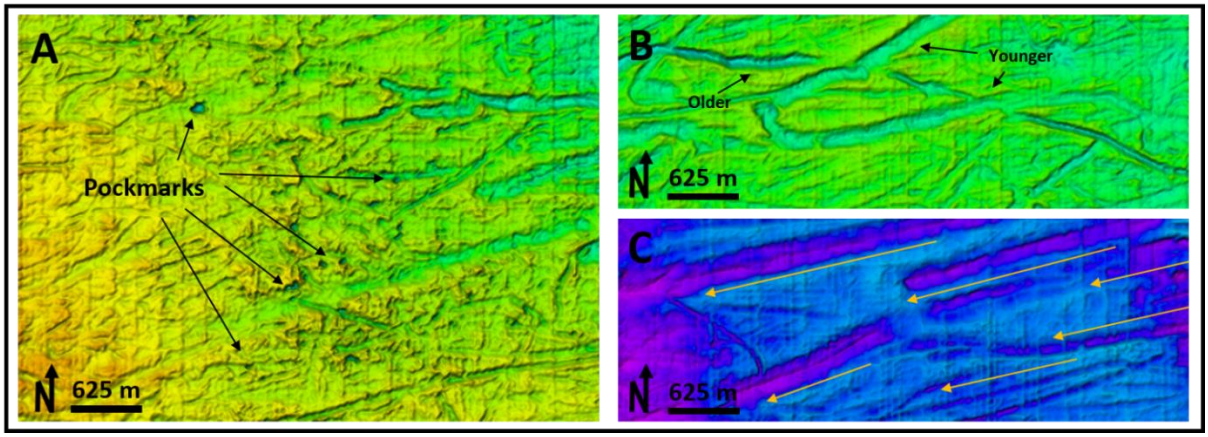

Figure 5-13 Closer look at some of the geological features seen in **Figure 5-12**. **A)** Area influenced by the presence of many pockmarks, both around and inside the interpreted plough marks. **B)** Crossing plough marks, indicating age differences. **C)** Parallel lineations in the eastern part, giving a good approximation on the ice direction, indicated in yellow arrows.

5.2 Faults

Faults are observed throughout the whole dataset, affecting the stratigraphic sequences above Snøhvit. Although this study focuses on the shallow strata, deep-seated faults may act as conduct for fluid migration and will be discussed in relation to shallow fluid accumulations. The interpreted faults are divided into two categories, deep-seated faults (major and intermediate faults) and shallow faults (minor and polygonal) **(Figure 5-14)**. This thesis focuses on the deep-seated major faults and shallow polygonal faults. The former is observed from the deepest Jurassic sequences, through the reservoir and all the way up to the Paleocene-Eocene units. The interpreted polygonal faults are located in the Upper Cretaceous Kolmule formation.

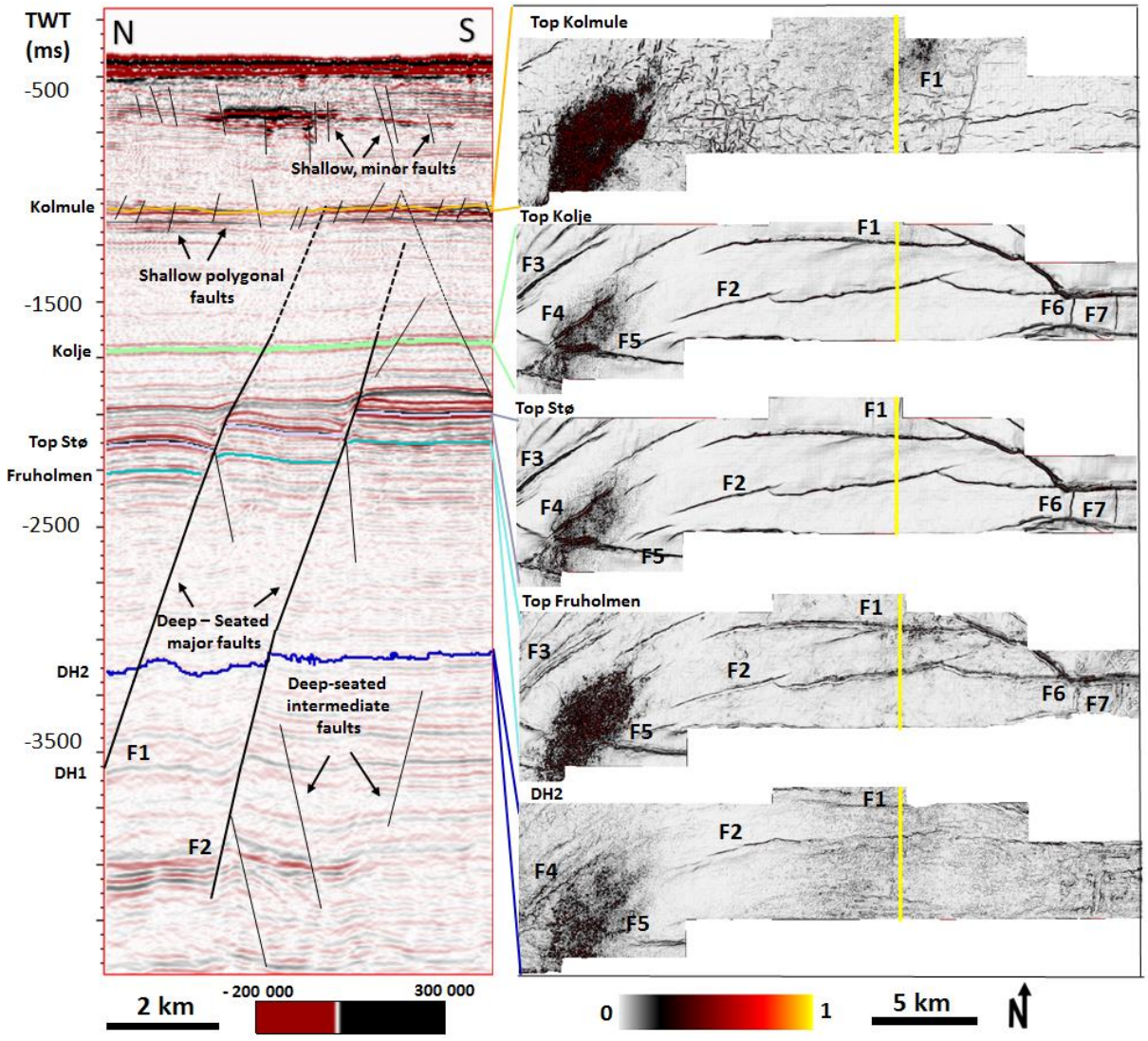

Figure 5-14 Left hand side shows the categorized faults in a seismic profile. Deep-seated (major and intermediate) and shallow (minor and polygonal) faults are identified. The 7 major faults (F1-F7) are visualized in variance attribute maps (right hand side), from the deep horizon, DH2 to the shallower formations. Polygonal faults are identified in variance map from Kolmule surface.

5.2.1 Major faults

Seven deep-seated major faults are observed and further described in this subchapter, denoted F1 - F7 **(Figure 5-14).** These faults are ranging in a large interval between deep Triassic and shallow Paleogene sequences, but the exact termination of the major faults are sometimes hard to observe due to acoustic masking throughout the dataset. The trending strike is found in an east – west direction, with some N-S oriented exceptions. The faults have been active since the upper Jurassic and shows variations in dip angle due to reactivation in the lower Cretaceous. They are interpreted as normal dip-slips faults, with varying dip angles from 55-75 degrees.

Fault 1 and 2 (F1 and F2) are the longest observed faults in this study, measured to approximately 13 and 22 kilometers, respectively. They have parallel strike orientation in an E-W direction. The faults are traceable from the deepest sequences all the way up to Kolmule formation, where the exact termination is hard to predict. The two interpreted faults are both normal dip-slip faults, dipping around 65 - 75 degrees. The faults are penetrating the Snøhvit reservoir, separating the different segments into footwalls and hanging walls relative to each other **(Figure 2-12A).**

Fault 3, 4 and 5 (F3, F4 and F5) are observed in the western part of the seismic cube. The strike orientation of F3 and F4 are in parallel SW-NE directions, while F5 is oriented WNW-ESE. Their lateral extent is measured to be about 5080, 4750 and 8200 meters, respectively. In the vertical seismic section they are observed tilting approximately 60 - 70 degrees, **(Figure 5-15B)**, F3 and F5 towards the NW and F4 towards SE. The deepest part of the faults are hard to interpret due to the large area of acoustic masking. This is interpreted to be either presence of gas arriving from the deep, or interruptions from the large gas chimney above, hereinafter referred to as gas chimney 1 (C1). Most of the fourth fault is located within (C1), making it hard to predict the exact origin and termination. On the footwall, F5 is also truncating the large chimney, making it difficult to see if the fault is reaching any shallower formations. The faults are interpreted as normal dip-slip faults, and are traceable down to approximately 2400-2700 ms (twt). They are presumably reactivated repeatedly, dividing the reservoir fault blocks in horst and graben structures **(Figure 5-15B).** Fault 4 and 5 are pointing towards a large area of high amplitudes, located on top of the gas chimney. These amplitudes are in for interpretation later on.

In the east, fault 6 and 7 (F6 and F7) appear, oriented perpendicular to the rest of the faults **(Figure 5-15C).** The strike orientation is N-S, extending approximately 1400-1600 meters. They are traceable from lower Triassic sequences, up to Top Kolje Fm., dividing the reservoir stratigraphy into horst and graben structures.

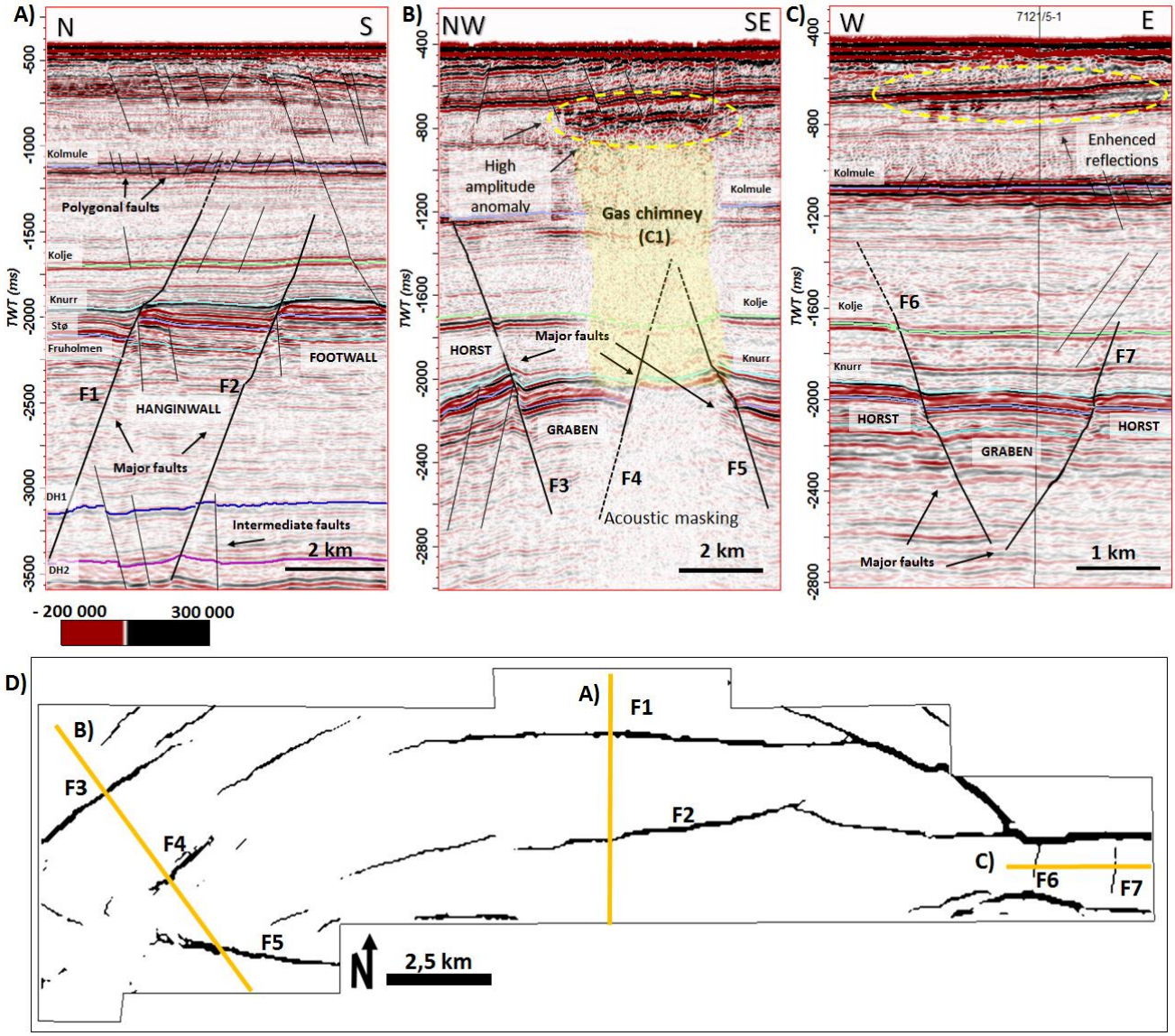

Figure 5-15 Seismic sections of all the major faults (F1-F7) interpreted in this study. **A)** Seismic profile of the longest faults observed in this area, F1 and F2, originating from the deep sequences with possible termination near the polygonal faults in Kolmule. **B)** F1, F2 and F3 observed near the large gas chimney (C1) in the east. Horst and graben structures observed in the reservoir. **C)** F6 and F7 in the east, oriented perpendicular to the rest of the faults. **D)** 2D planar view of all the deep-seated major faults interpreted in this study, denoted F1 – F7. Extracted from the Stø Formation. Yellow lines indicate location of seismic profiles A-C.

5.2.2 Shallow faults

Two types of shallow faults are identified within sequence 8. These are the Paleocene – early Eocene faults in the uppermost part and the closely-spaced, late Cretaceous faults at the lowermost part. The former are tracked down to Campanian age, and are observed with highest density pr. m^2 in the west, where they intersect with a large area of enhanced reflections. The latter is a network of faults observed in a time interval of approximately 60 ms (twt), with dominant strikes orientated in N-S and E-W directions, tilting in opposite directions. Variance map of Top Kolmule formation reveals a polygonal pattern with linear to curved-shape distribution, and some overlapping features (**Figure 5-16A).** The highest density is found in the middle and the western parts of the seismic cube, covering an area of approximately 67 km^2, with 100-500 meters spacing. Due to their character and their closely spacing, this fault system is interpreted as polygonal faults **(Figure 5-16B).**

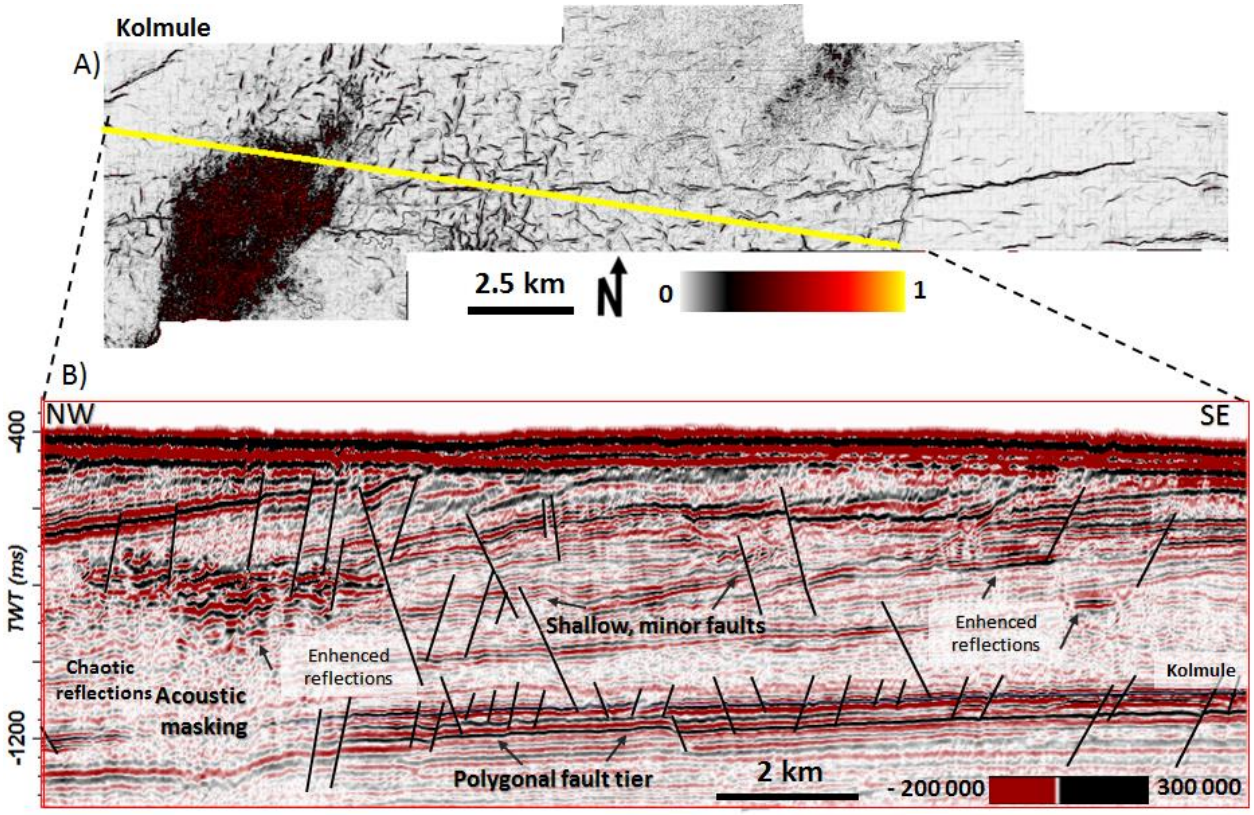

Figure 5-16 A) Shallow faults observed in a variance attribute map extracted from the interpreted Kolmule horizon. **B) S**eismic section, yellow line in A indicates the location.

5.3 High amplitude anomalies

Within the Cenozoic stratigraphy of sequence 8, many enhanced reflections, or high amplitude anomalies were observed. Four of these were further interpreted based on their amplitude values, polarities and stratigraphic location, displayed in **Figure 5-17.** This section provides a detailed description of the anomalies, with focus on size, shape, orientation and affected time window.

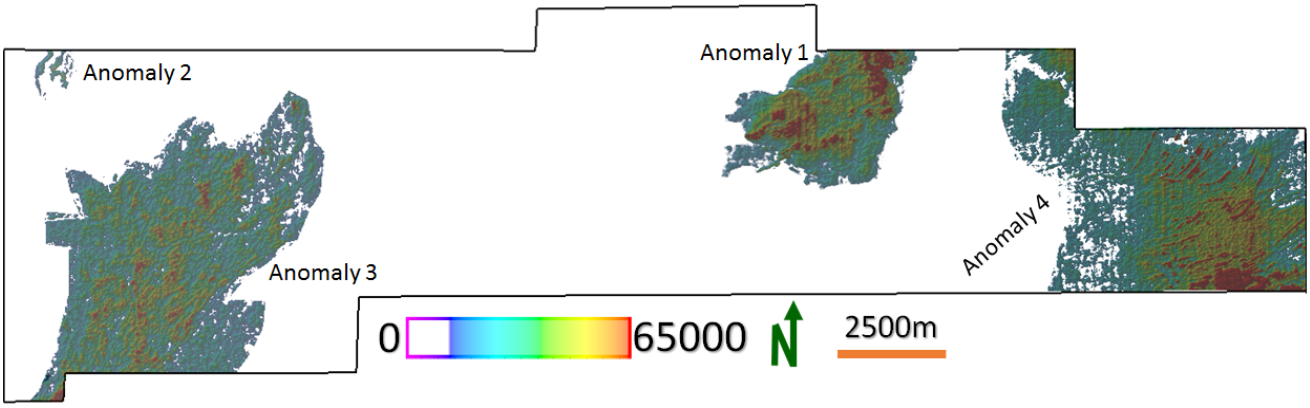

Figure 5-17 2D planar view of the distribution of all the high amplitude anomalies interpreted in this study.

5.3.1 Amplitude anomaly 1

Anomaly 1 (A1) is located in the northeastern part of the seismic cube with a sub-angular shape **(Figure 5-17).** It extends 5.1 km in an SW-NE direction and 2.9 km in a NW-SE direction. The lateral distribution of the anomaly is measured to be approximately 9.2 m^2, but is thought to extend further north due to the un-natural ending and the lack of seismic data. The anomaly is characterized by strong, high amplitude values with polarity reverse compared to the seafloor **(Figure 5-18).** The underlying seismic is affected by acoustic masking and velocity pull-down effects. The anomaly is located on the hangingwall side of F1, and marks the top of gas chimney 2 (C2), approximately 200 – 404 ms (twt) below the seafloor.

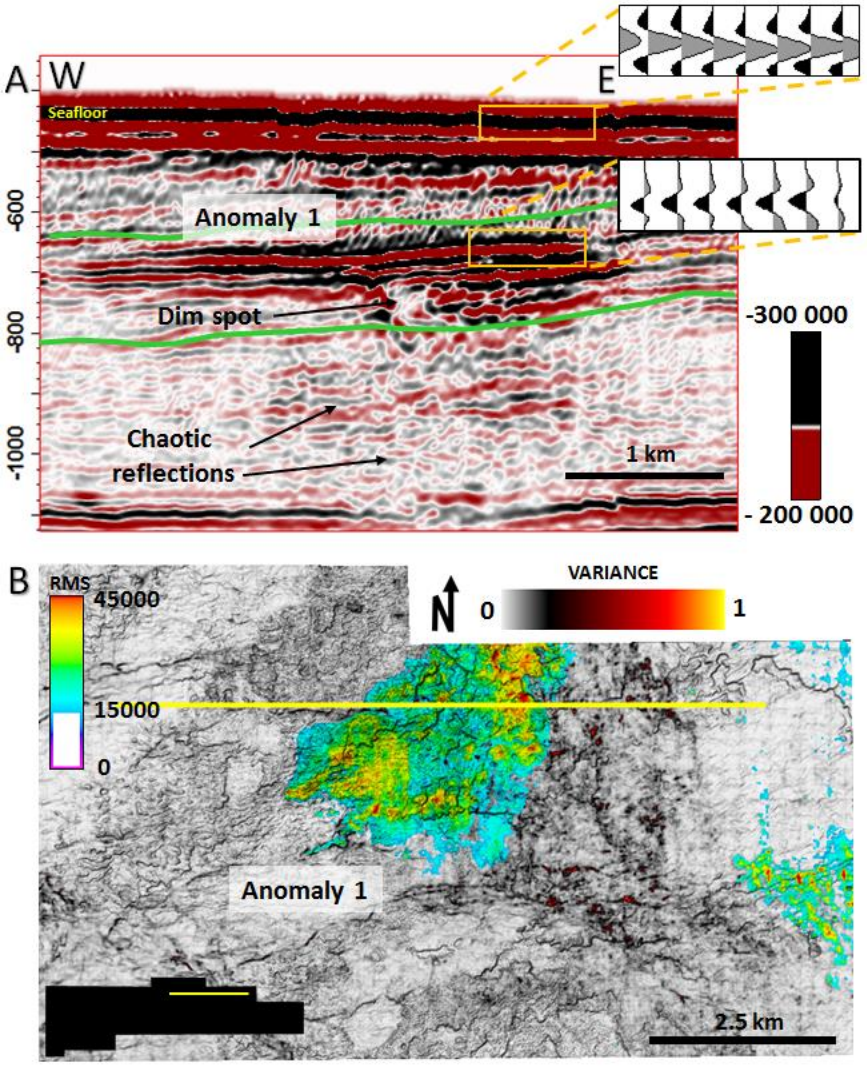

Figure 5-18 A) Seismic section across anomaly 1 (A1), showing how the high amplitude reverse in polarity compared to the seafloor. **B)** Combined RMS amplitude and variance maps, extracted from a 204 ms (twt) interval indicated in A (green lines).

5.3.2 Amplitude anomaly 2

A smaller high amplitude anomaly (A2) is located in the northwestern part of the seismic cube, with an elongated shape oriented in an N-S direction (**Figure 5-17**). It is observed 200 ms (twt) below the seabed, in a time interval of 88 ms (twt), showing a polarity reverse compared to the seabed **(Figure 5-19A)**. A1 is characterized by high and strong amplitude reflections, with intersection of minor, Paleocene-early Eocene faults **(Figure 5-19B).** The lateral extend of the anomaly is measured to be 0.54 square meters, though to extend further north, beyond the seismic cube.

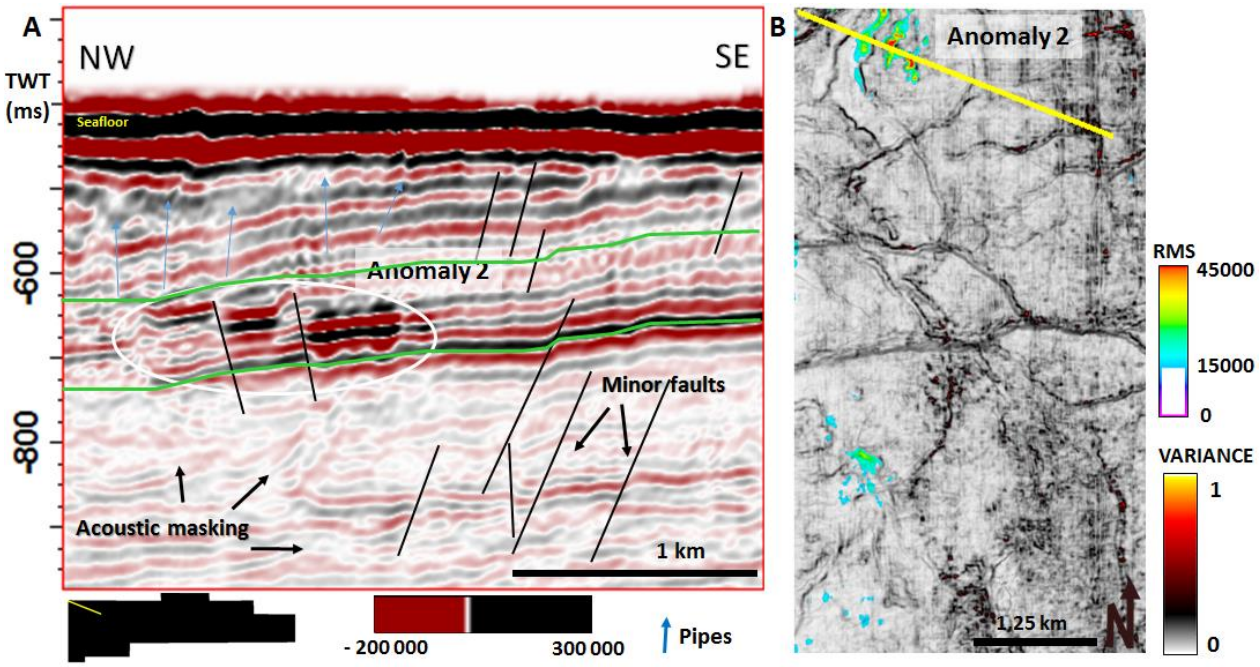

Figure 5-19 A) Amplitude anomaly 2 from the vertical seismic section (NW to SE), showing acoustic masking, intersection with minor faults and seismic pipe structures above. **B)** RMS / variance map between the green lines indicated in A. The interval is 110 ms (twt).

5.3.3 Amplitude anomaly 3

Anomaly 3 (A3) is identified in the southwestern part of the cube **(Figure 5-17),** located on top of the largest gas cloud in the study (C1). It is related to two of the interpreted major deep-seated faults (F4 and F5), and are cross cut by several minor Paleocene – Miocene faults. The seismic reflections beneath the observed structure is affected by distortions, acoustic masking and pull downs, probably in relation to the large gas chimney.

A3 is located 256 – 388 ms (twt) below the seafloor and is characterized by a decrease in acoustic impedance, appearing as a strong negative reflection with reversed polarity compared to the seafloor **(Figure 5-20**). The shape is observed with an elongated, sub-angular configuration, with the long axis oriented in a 7.8 km SW-NE direction, and the short axis in a W-E direction, 4.6 km long. It is unconformable with the surrounding reflections, cross cutting the westerly dipping stratigraphy. A3 is located in a time interval of 132 ms (twt), above weak, discontinuous and irregular seismic reflections traceable down to the reservoir in relation to the Jurassic faults.

With the abovementioned characteristics in mind, the top of anomaly 3 is interpreted as a possible BSR (bottom simulating reflector), representing the opportunity for stable gas hydrates in the sediments above.

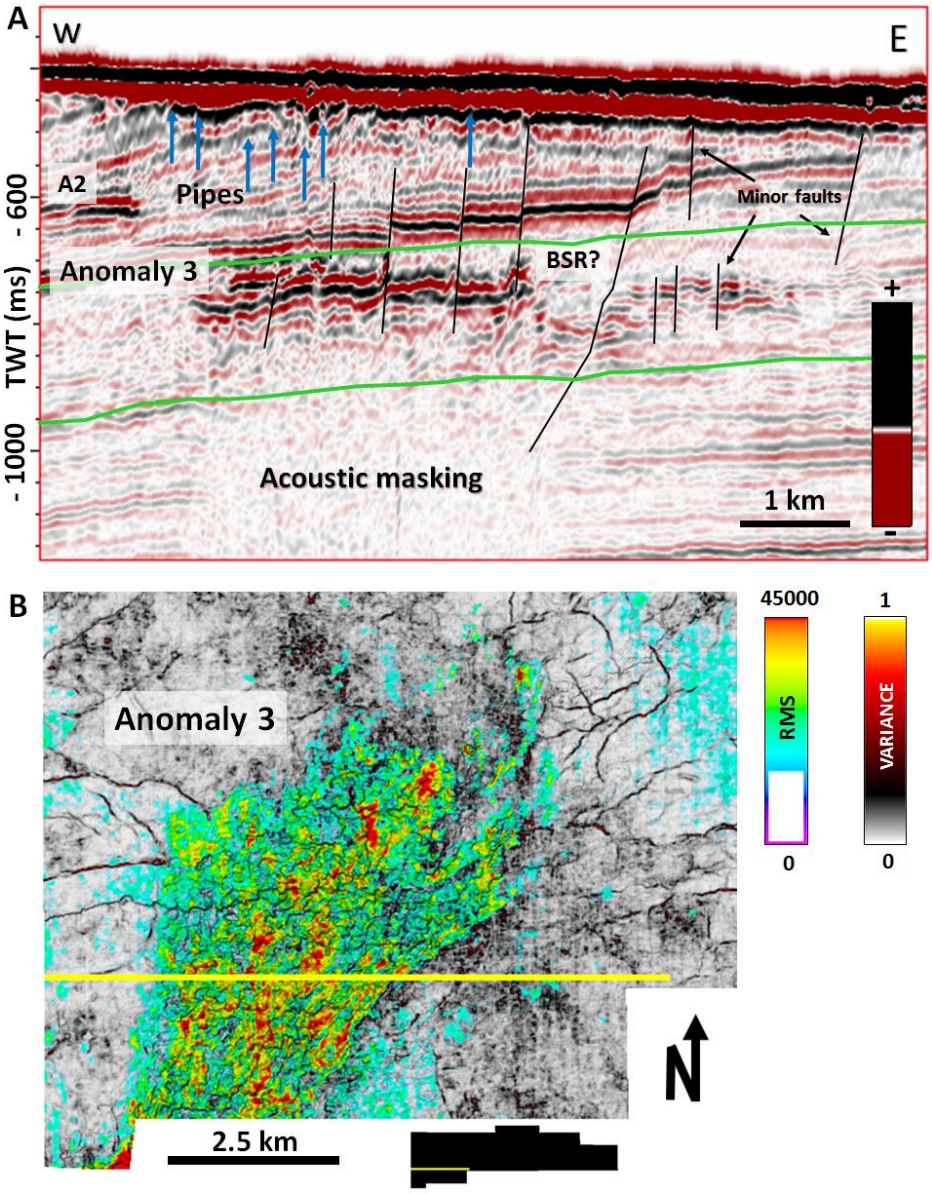

Figure 5-20 A) Seismic section (XL: 12229) of A3, showing how minor faults are crosscutting the anomaly. Notice the location of A2 in the top left corner. **B)** Variance map in combination with a RMS amplitude map, from a 205 ms (twt) time interval indicated between the green lines in A.

5.3.4 Amplitude anomaly 4

Anomaly 4 (A4) is observed in the eastern part of the field **(Figure 5-17)**, up-dip from the earlier described A1. The lateral extend is approximately 18.7 square meters, with an elongated shape and the highest amplitudes located in the southeastern part of A4 **(Figure 5-21A).** The longest axis is measured to be 8.3 km (probably extending outside the cube) oriented in SE-NW direction and the short shortest axis is 4.1 km, oriented in an W-E direction. The seismic anomaly is located in a time interval of 156 to 316 ms (twt) below the seafloor.

Notice that the anomaly could be sub-divided in two, based on characteristics. The top of the anomaly is recognized with continous, dipping reflections from east to west, relative parallel with the backround reflections. This has the same polarity as the sefloor, opposite to the more horisontal amplitudes beneath, which corsscuts the dipping reflections (**Figure 5-21B)**. The deep-seated faults 6 and 7 (F6 and F7) are observed in underneath the anomaly as well as the polygonal fault system in Kolmule.

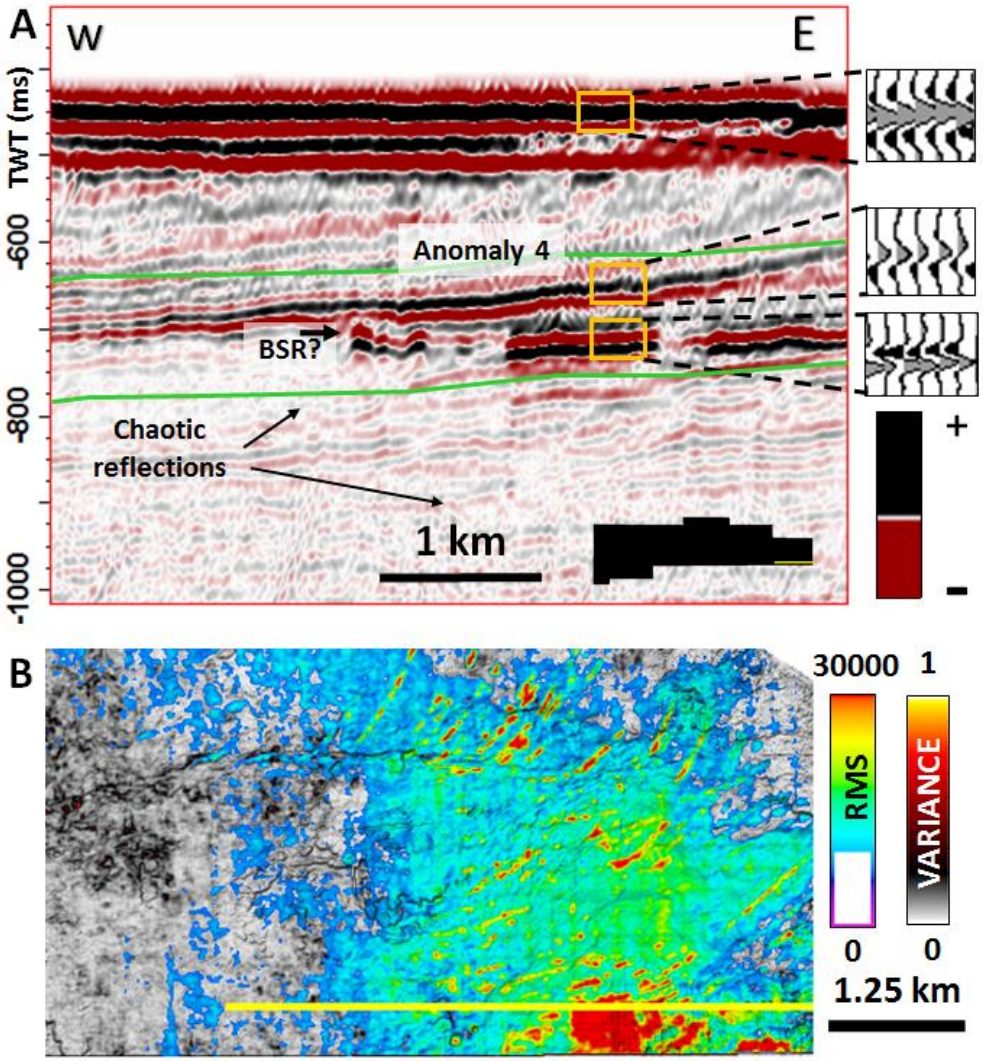

Figure 5-21 A) Seismic section of A4, showing the different characteristics within the anomaly. Notice the different polarities and interaction with the dipping reflections. **B)** Combined variance and RMS amplitude map from the 160 ms (twt) time interval indicated in A.

5.4 Pockmarks

As described in previous chapters, the seafloor is strongly influenced by several morphological depressions, both erosional structures from glaciers and circular to sub-circular features observed as isolated depressions. This section deals with the latter, being a potential indication of fluid leakage on the seafloor. With the awareness of these being a result from icebergs piercing the seabed, these depressions are referred to as pockmarks, and will later be discussed in relation to deeper fluid flow features.

They either occur individually, often within glacial-related plough marks or together in close-spaced groups as smaller depressions. Many similar features were observed, where a selected number of them were further analyzed and interpreted, indicated in black squares in **Figure 5-22.** The observed depressions are ranging from a few meters to 14-15 meters in depth. The configuration are shifting from circular to sub-angular in a plan view perspective, while seen in the seismic section they alter between U-shape to V-shape with different symmetry. The distribution vary within the study area, with a high density of close-spaced pockmarks observed in the west. Going further east, the seafloor contains more individual depressions, observed within and around these parallel, linear features.

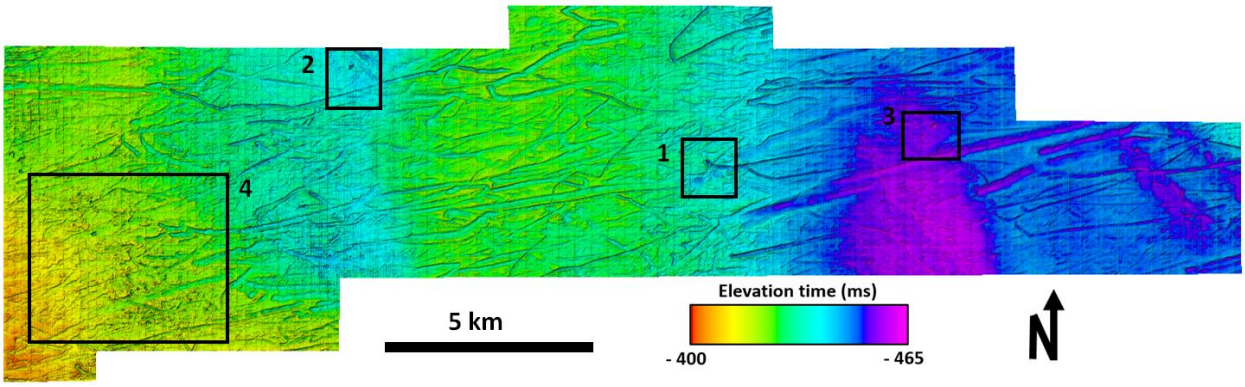

Figure 5-22 Overview of the seabed, with the pockmarks described in this chapter indicated in black squares from 1 – 4.

5.4.1 Pockmark 1 (P1)

The first interpreted pockmark (P1) is located in the middle of the seismic cube with a sub-circular shape. It is found within a glacial plough mark **(Figure 5-23A).** The longest axis is measured to be approximately 162 meters with a NW-SE direction, and the shortest axis to 114 meters. The lateral distribution is measured to approximately 14 138 square meters, with a depth calculated to be 14 meters. In the seismic section **(Figure 5-23),** the feature is identified with a u-shape. Below this depression, enhanced reflections and interpreted seismic pipes are visible, lying above nearby faults.

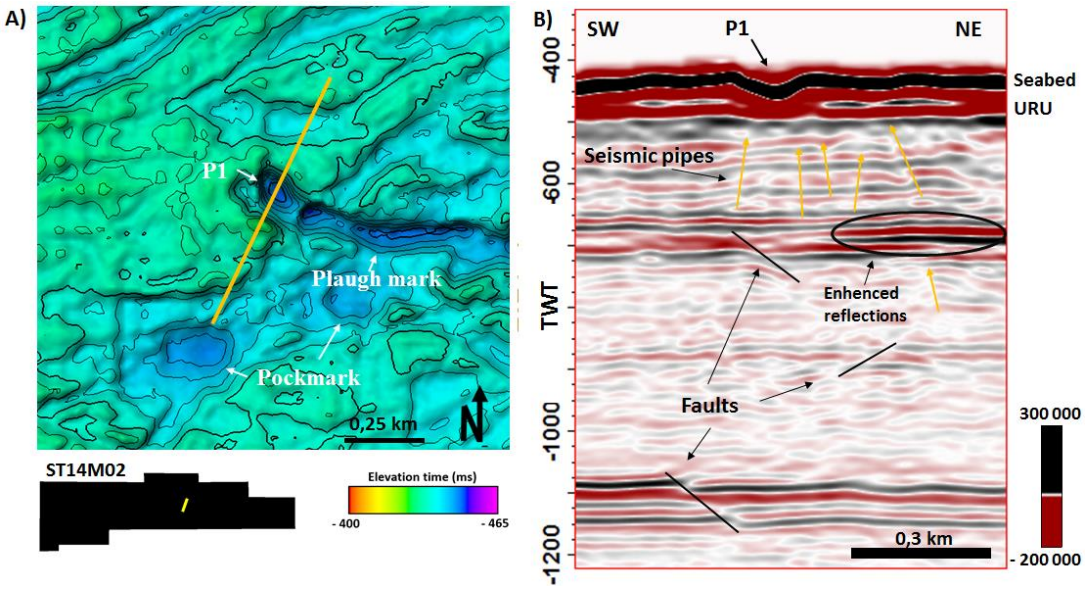

Figure 5-23 A) Close-up of an interpreted pockmark (P1) from square 1 in **Figure 5-22**. **B)** Seismic section from SW to NE random line, crossing P1. Yellow line indicates location of the profile

5.4.2 Pockmark 2 (P2)

This feature is observed in the western part of the seismic cube (square 2 **Figure 5-22**), with a sub-angular shape of approximately 10 091 m^2. The longest axis is oriented in a SE-NW direction, measured to be approximately 157 meter, while the shortest axis is 82 meters in a SE-NW direction **(Figure 5-24A).** The depth is calculated to be approximately 11.8 meter. In a vertical section the depression is observed with an asymmetrical shape, not interfering with the upper regional unconformity (URU). Below URU, the reflections are affected by weak, irregular amplitudes possibly due to seismic pipes **(Figure 5-24B).**

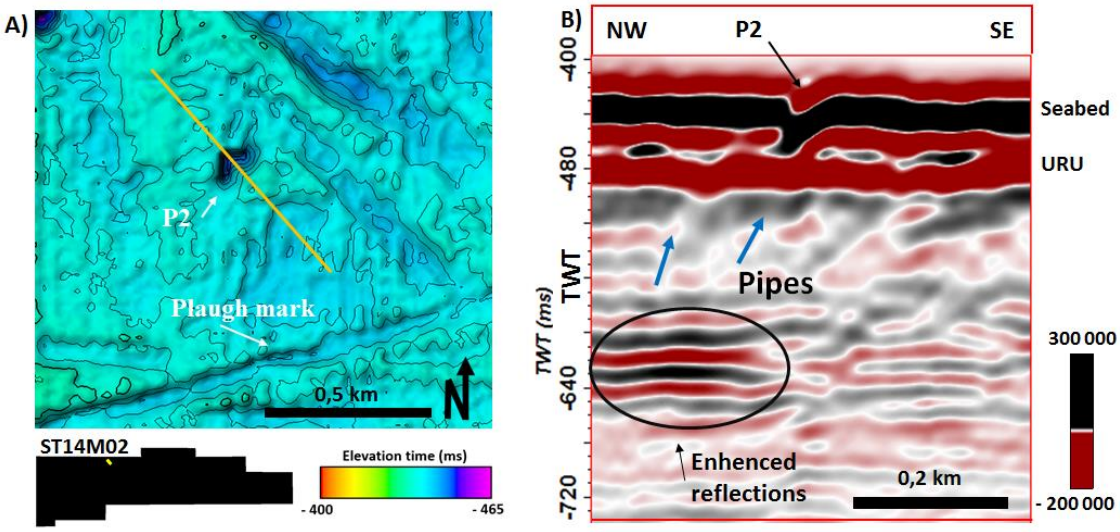

Figure 5-24 A) Close-up of P2 indicated in square 2 (figure 5-22) with surrounding ploughmarks. **B)** Seismic profile from NW – SE (random, yellow line in A), crossing P2.

5.4.3 Pockmark 3 and 4 (P3 and P4)

Observed above in a 2D window, pockmark 3 (P3) has a sub-circular shape with an area of approximately 20 300 m^2 **(Figure 5-25A).** The longest axis is measured to be around 200 meters oriented in a SW-NE direction. The shortest axis is measured to be approximately 131m and oriented in N-S and the depth is calculated to be 6 meter. Pockmark 4 (P4) is observed in the same area as P3, with a relative circular/sub-angular shape. The longest axis is approximately 72m oriented in a SW-NE direction. The shortest axis is oriented NE-SE and measured to be 45 meters. The features depth is calculated to be approximately 6 meters. In the vertical section, both the depressions have asymmetric shape **(Figure 5-25B).**

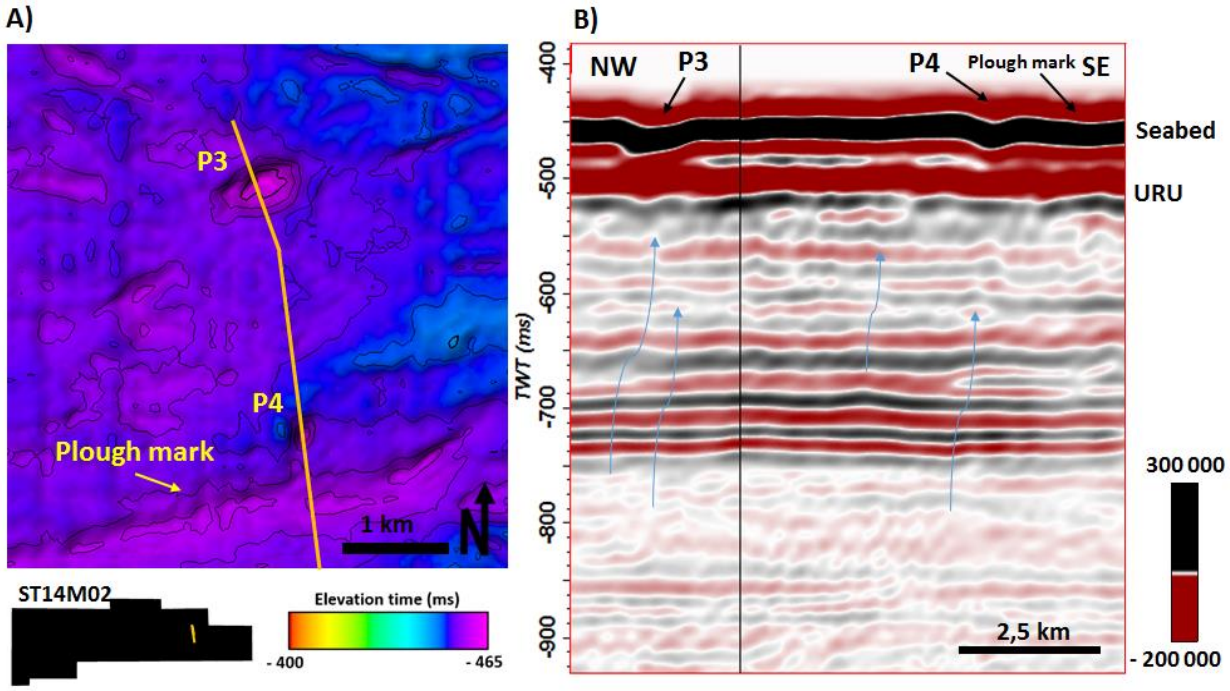

Figure 5-25 A) Close-up of P3 and P4 indicated figure 5-22 (square 3 in **Figure 5-22**) with surrounding ploughmarks. **B)** Seismic profile from (yellow, random line in A), showing P3, P4 and the plough marks observed in A.

5.4.4 High density area of depressions

In the western part of the cube (square 4 in **Figure 5-22**), a close-spaced area of depressions is observed. These pockmarks are smaller than previously interpreted depressions, and range from a few meters to approximately 7 meters deep. Some are hard to observe in the vertical profile due to resolution, but in a 2D-window they seem to have a sub-circular to circular shape **(Figure 5-26A)**. In the vertical profile, they are observed above seismic pipes, high amplitudes (A3) and a large gas chimney (C1) **(Figure 5-26B).**

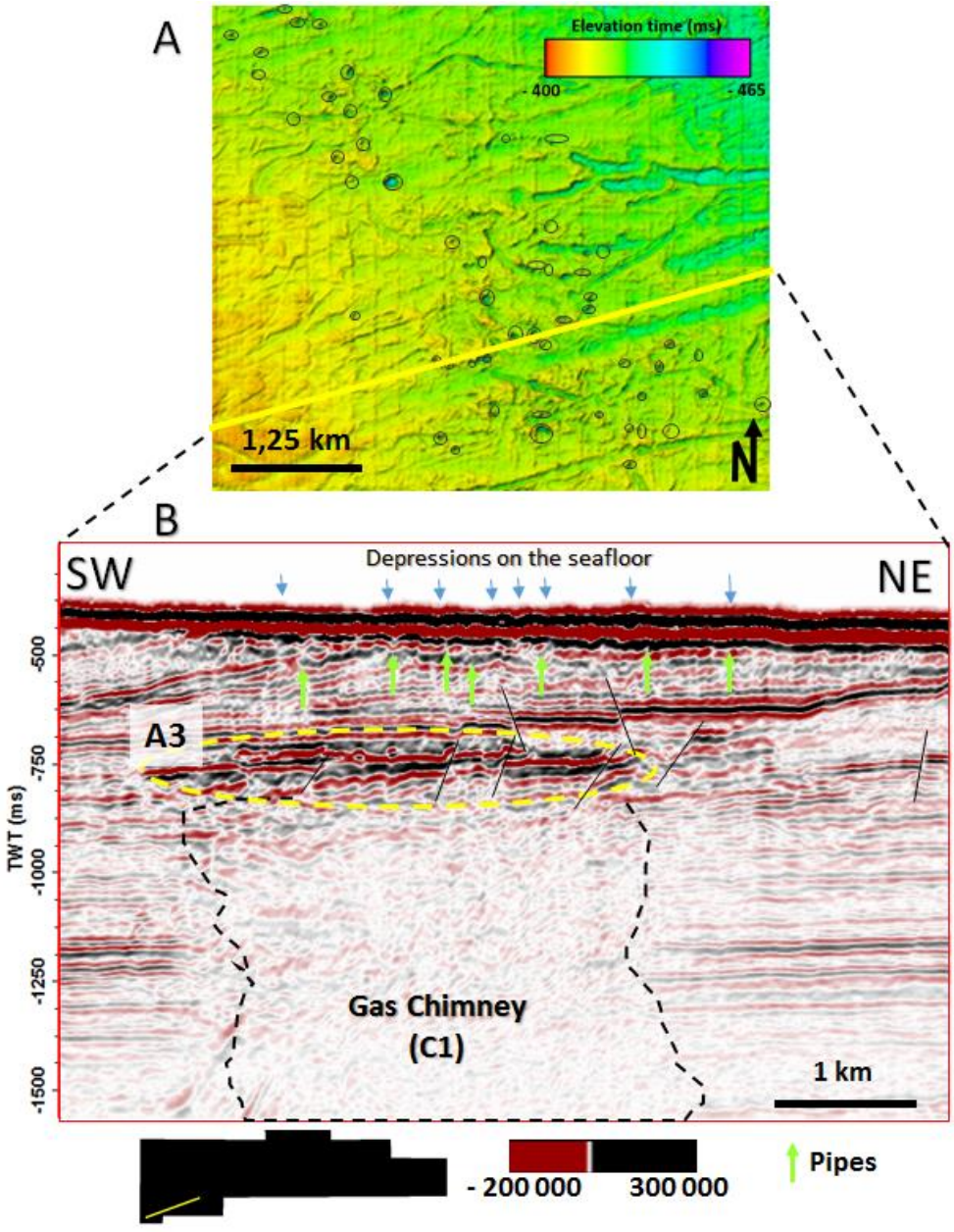

Figure 5-26 A) High density area of pockmarks observed on the seabed surface. **B)** Seismic section revealing the location of these pockmarks above seismic pipes, A3 and C3.

5.5 Analytical model

5.5.1 Results of the analytical model

The input data from the Snøhvit field is inserted in equation 2.4 and equation 2.5. The leakage factor is calculated after 10 years of stable CO_2 injections, equal to the period of injection at the Snøhvit field. According to O. Hansen et al. (2011) the injector rate is 1400 Sm3/d. **Table 5-1** shows the leakage coefficients of the two faults.

Table 5-1 Calculated leakage factor for the two faults located close to the F-2 CO2 injector

Leakage factor [%]	
Fault 1	0.004 %
Fault 2	0.002 %

The results show that a very low amount of the injected CO_2 leaks into the overburden. It also shows that faults located closer to the CO_2 injector has a higher leak off coefficient than a fault located further away. The result is assuming that the reservoir is in connection with an overlying sand with good properties in the Hekkingen formation through a fault that has flow potential.

5.5.2 Sensitivity study

The sensitivity study is carried out to see which parameter is most important for the leakage of CO_2 from the reservoir and into the overburden. The different variables used is found in **Table 5-2**. **Figure 5-27** shows how sensitivities to different parameters impact the leak off value when all other parameters are kept constant. The dotted line shows the leak off value for the base case.

Table 5-2 Variables used in the sensitivity study

	Low	Base	High
Reservoir permeability [mD]	10	325.8	2000
Overburden permeability [mD]	10	50	1000
Fault permeability [mD]	0.1	1	1000
Distance to fault [m]	100	600	2000
Thickness of overburden [m]	5	15	50
Thickness of cap rock [m]	5	15	50
Height reservoir [m]	15	81	150

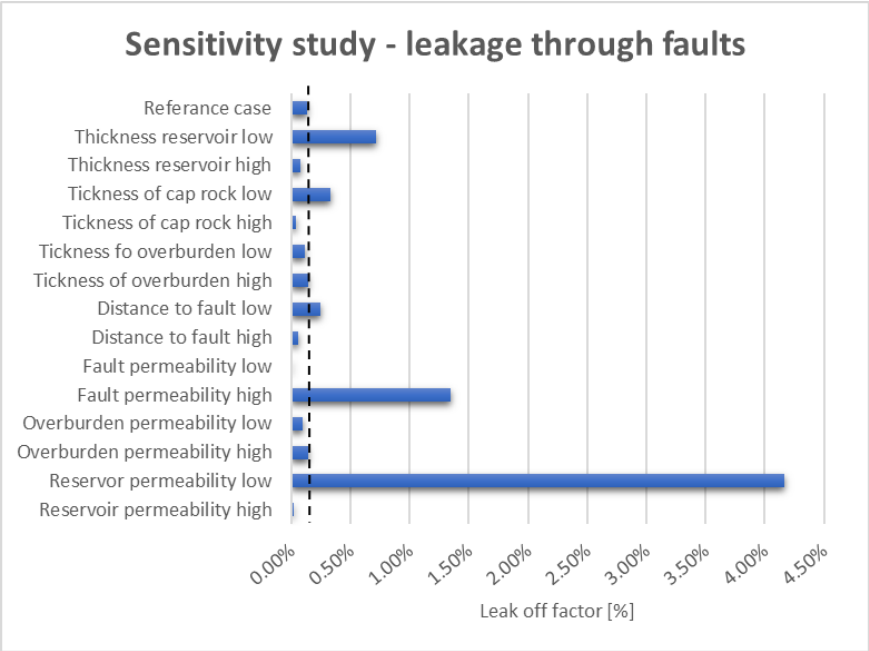

Figure 5-27 Sensitivity plot showing the most important parameters for leakage through faults.

As **Figure 5-27** shows, the most important variables for the leak off value is the reservoir permeability, fault permeability and thickness of the reservoir. These three parameters will be investigated further.
Firstly, the permeability in the reservoir is varied between 5md – 1500 md to see the effect on the leakage coefficient, while all the other variables is constant, see **Figure 5-28**.

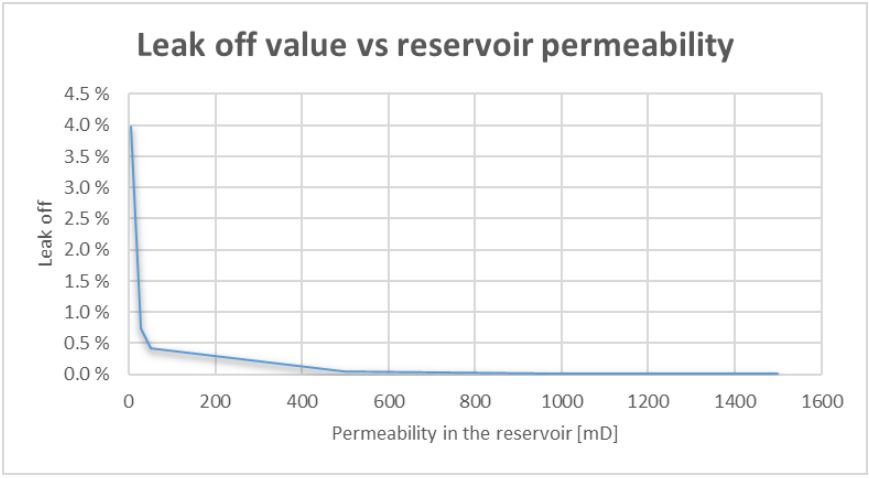

Figure 5-28 Leak off value vs. reservoir permeability. The overburden permeability is sat to 50 mD.

The overburden permeability is 50 mD. The result shows that the leakage coefficient increases significantly when the permeability in the reservoir decreases below the permeability to the overburden

sand. This means that there is a risk of leakage if CO_2 is injected into a reservoir that has lower permeability than the overlaying sand.

Secondly, the fault permeability is varied together with a low permeability in the overburden sand sat to 10 md. **Figure 5-29** shows the leak off value.

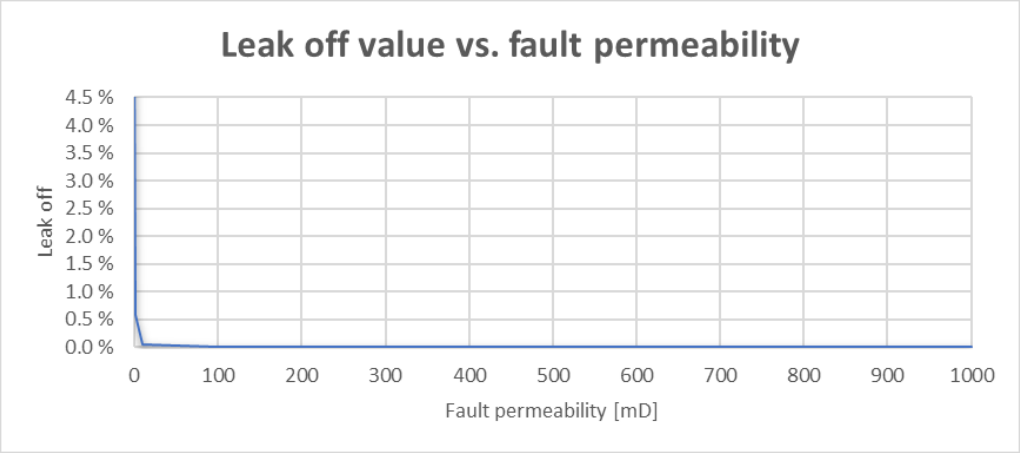

Figure 5-29 Leak off value vs. fault permeability. The overburden permeability is sat to 10 mD.

The results show that the leak off factor is low even if the fault has high permeability. This implies that the risk of leakage is low if the overlaying aquifer has a low permeability, regardless of the fault permeability.

Thirdly, the thickness of the Stø reservoir is varied between 5 m – 150 m while the reservoir permeability is set to 50 mD, see **Figure 5-30**. This is used to see the effect off thickness given a low permeability reservoir. All the other variables are constant.

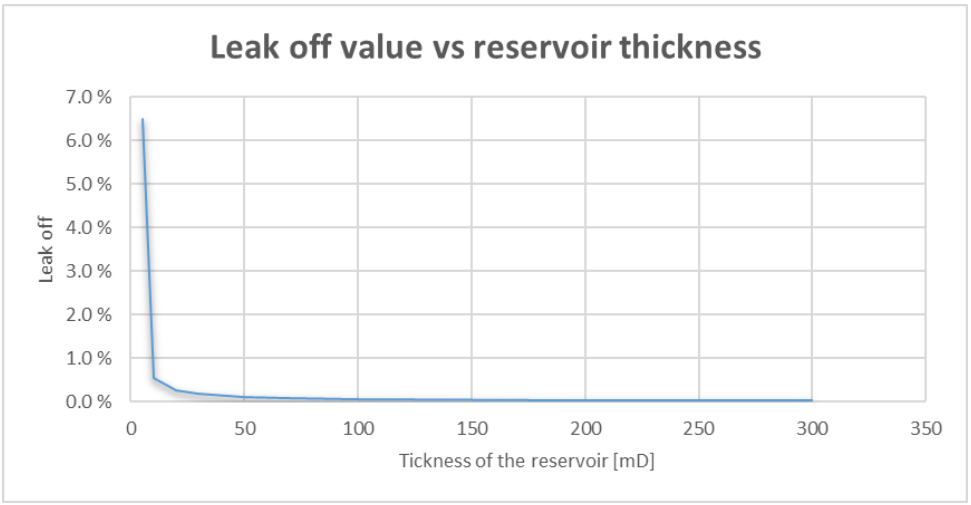

Figure 5-30 Leak off value vs. reservoir thickness.

6 Discussion

The main objective in this chapter is to discuss the observed results in relation to each other, in order to better understand the mechanisms controlling fluid flow and accumulation of hydrocarbons.

6.1 Evidence of shallow gas and gas hydrates

The Paleogene – Neogene stratigraphy above the Snøhvit hydrocarbon field in Hammerfest basin is characterized by several high amplitude anomalies, zones of chaotic reflections, seismic blanking and faults. Four high amplitude anomalies (A1-A4) have been described and interpreted as potential accumulations of shallow gas, some as potential BSRs with overlaying sediments of gas hydrates. The confidence of these assumptions, and discussion of the relation with identified gas chimneys, seismic pipes, pockmarks and deep-seated structures are presented here.

6.1.1 GHSZ in study area

Some of the gas anomalies in this study are discussed in relation to overlain hydrate bearing sediments (e.g. A1, A3 and A4), due to their crosscutting appearance compared to the background layers and their location near faults, gas chimneys, pipes and pockmarks. The credibility of the interpreted BSRs depends on the gas hydrate stability zone within the study area. **Figure 2-8** comprise the Hammerfest Basin as a region where hydrates can be stable, unless the gas composition is pure methane. Increased wetness (i.e. decreased amount of C_1) provides increased thickness of the GHSZ.

Available log data **(Figure 6-1)** shows the trip gas composition in well 7121/5-1. Trip gas is gas entrained in the drilling mud during the well string`s *trip* back to the surface (Ablard et al., 2012). Gas readings (**Appendix B, Table B-1**) show the presence of ethane (C_2), increasing wetness and thus the GHSZ. This is supported by Vadakkepuliyambatta et al. (2017) who suggest a methane composition in well 7121/5-1 of 85-90 % (see **Figure B-0-1, Appendix B**). That means, by including the depth of the interpreted anomalies in **Figure 2-9**, and assuming average sediment velocity (2000m/s), A1, A2 and A3 all coincides with the bottom of the stability zone **(Figure 6-2)** and might be resembles of BSRs.

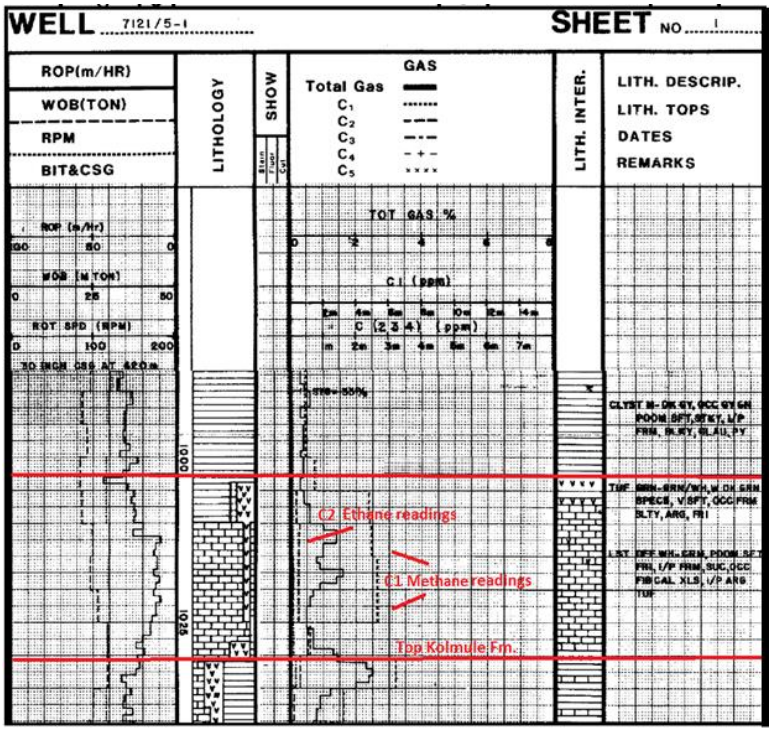

Figure 6-1 Gas readings showing trip gas composition just above Kolmule. Modified from released 7121/5-1 End-Of-Well Report, Statoil.

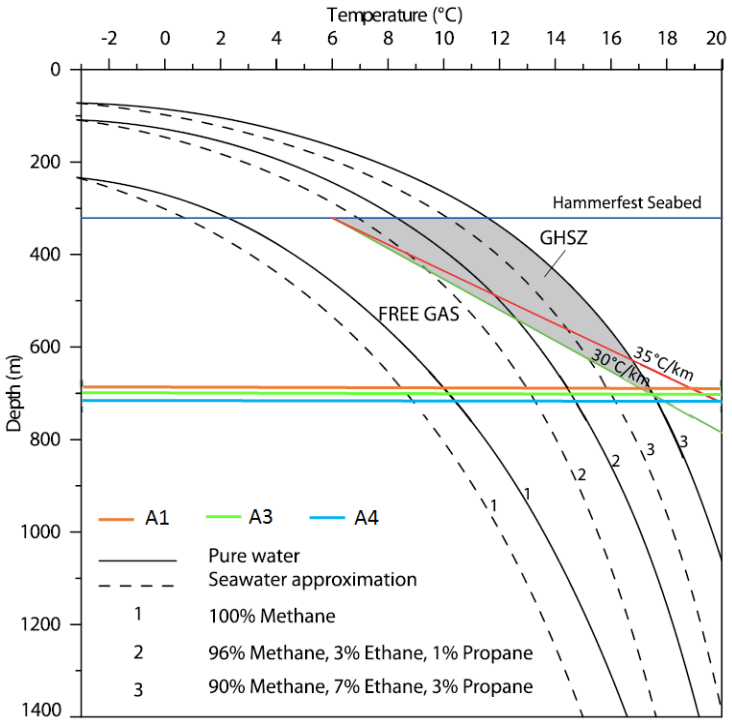

Figure 6-2 The interpreted gas anomalies (A1, A3, A4) in correlation with hydrate stability diagram, modified from Ostanin et al. (2013)

6.1.2 Correlation between interpreted anomalies and nearby structures

Anomaly 1 **(5.3.1)**, located in the eastern area, is found in correlation with hydrocarbon related features. Minor faults do not intersect with A1 as much as anomalies spotted in the west, and may not be a part in controlling the fluid migrations towards the seabed. This can be an explanation of the less density area of observed pockmarks compared to the western area. Thus, some pockmarks are observed, both on the URU and on the seafloor. Seismic pipes located above the enhanced reflections are a possible explanation of these events, since acoustic pipes work as seal-bypass systems. As fluids keep migrating upwards (due to buoyancy), pressure builds up and overcomes the seal due to hydrofracture, leading in fluids assessing the seafloor through pipes.

From the previous discussion **(6.1.1)**, it is found that the top of A1 (measured at 680 m depth) correlates with the base of the gas hydrate stability zone **(Figure 6-2).** The fractured sealing above A1 is hence suggested to be gas hydrates, with the partly trapped free gas partly beneath as remnants of a BSR. The phenomenon of free gas escaping the sealing hydrates above, through vertical pipe structure, have been reported by others (Bünz et al., 2003; Gay et al., 2006).

Figure 6-3 illustrates the possible migration route for the accumulation of A1, which correlates with C2, the major deep-seated fault F1 and polygonal faults in Kolmule. Even though two major faults (F1 and F2) intersects the reservoir beneath A1, the gas chimney looks to follow the hanging wall of F1, implying that the thermogenic gas mainly migrated on this side of the fault. Hence, it is suggested that F1 plays a major role in the leaking of hydrocarbons from the reservoir, transporting the fluids along the hanging wall of the fault and inside C2 up towards the shallower strata. Reaching the Kolmule formation, the gas either follows the chimney vertically, or horizontally along the east, up-dipping reflectors of the upper Cretaceous sediments. The gas following the chimney is offered three opportunities reaching the Paleocene – early Eocene strata: 1) accumulate as free gas beneath the gas hydrates, 2) continuing through the hydrofractured hydrates via seismic pipes or 3) continuing along the up-dipping carrier beds towards anomaly 4 in the east.

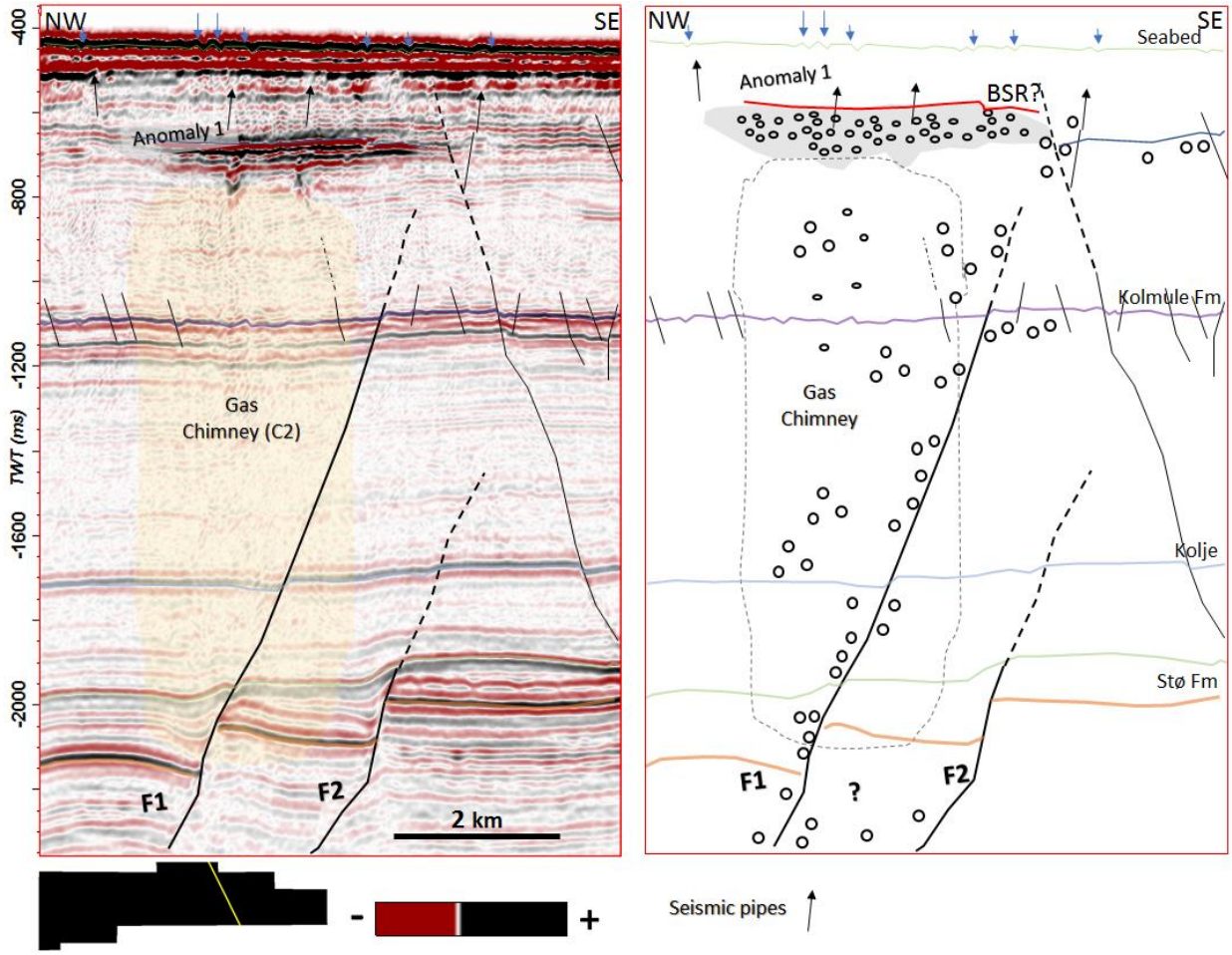

Figure 6-3 Conceptual model suggesting the accumulation of free gas trapped under gas hydrates, and the source of hydrocarbons from underlying chimney and faults.

Based on location, gas anomaly 4 **(5.3.4)** is discussed next. It is positioned in an up-dip perspective, and may be receiving fluids from A1, as well as deeper structures **(Figure 6-4).** Despite some observations of chaotic reflections, no clear evidence of a gas chimney is seen in the area beneath A4. Instead there are some enhanced reflections related to the dipping reflectors in upper Cretaceous, possible indicators of the presence of gas. Two of the possible sources of these high anomalies the deep-seated faults F6 and F7, and gas chimney 2, the same chimney providing hydrocarbons to A1. When arriving Kolmule formation from C2, these fluids might laterally escape along carrier beds, before seeping out of fractures related to the polygonal fault systems described in **5.2.2.**

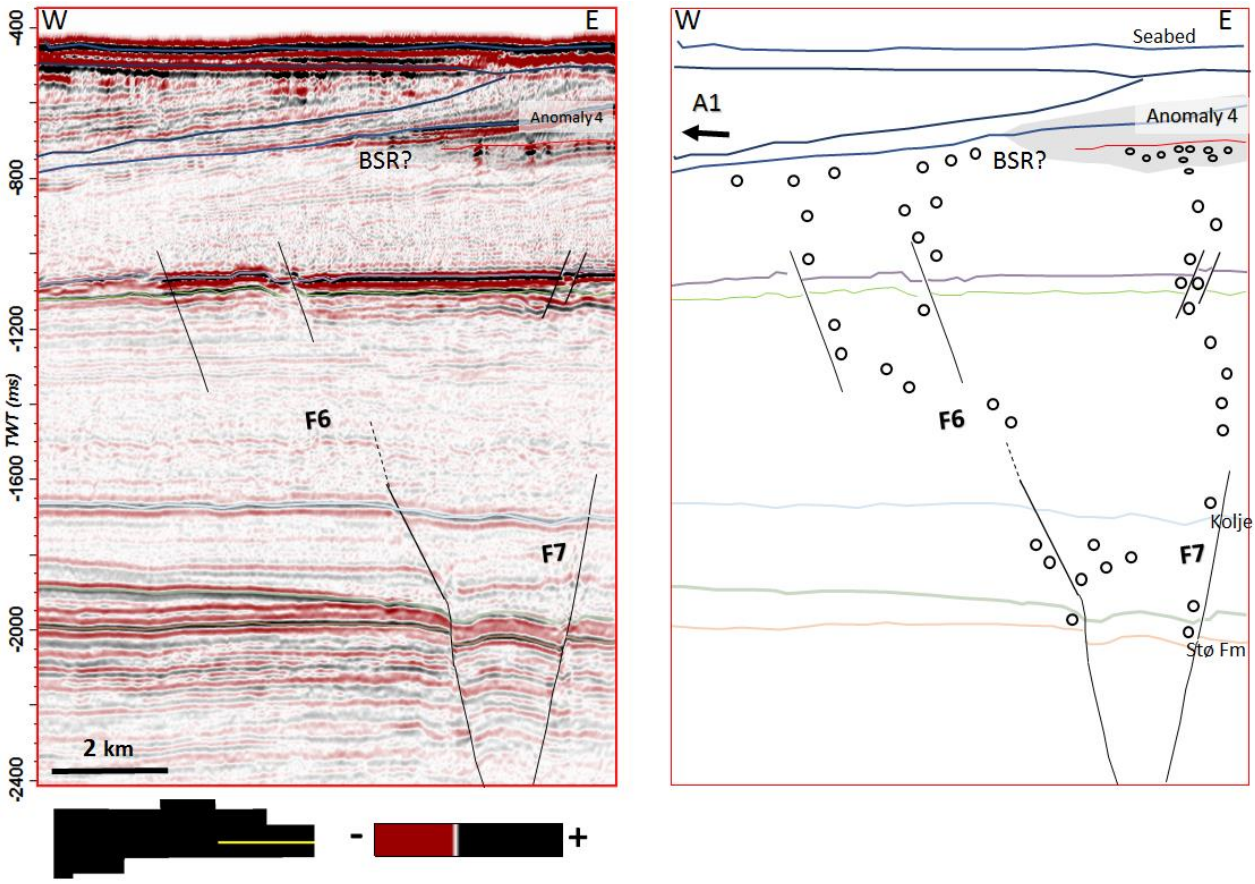

Figure 6-4 Conceptual model suggesting possible hydrocarbon sources for the interpreted anomaly (A4).

Examination of log curves from well 7221/5-1 **(Figure 5-10),** together with gas readings from released end-of-well report from the same well **(Figure 6-5)**, showed indication of gas present in and above Kolmule, supporting the possible migration route towards A4, from the polygonal fractures observed in this area.

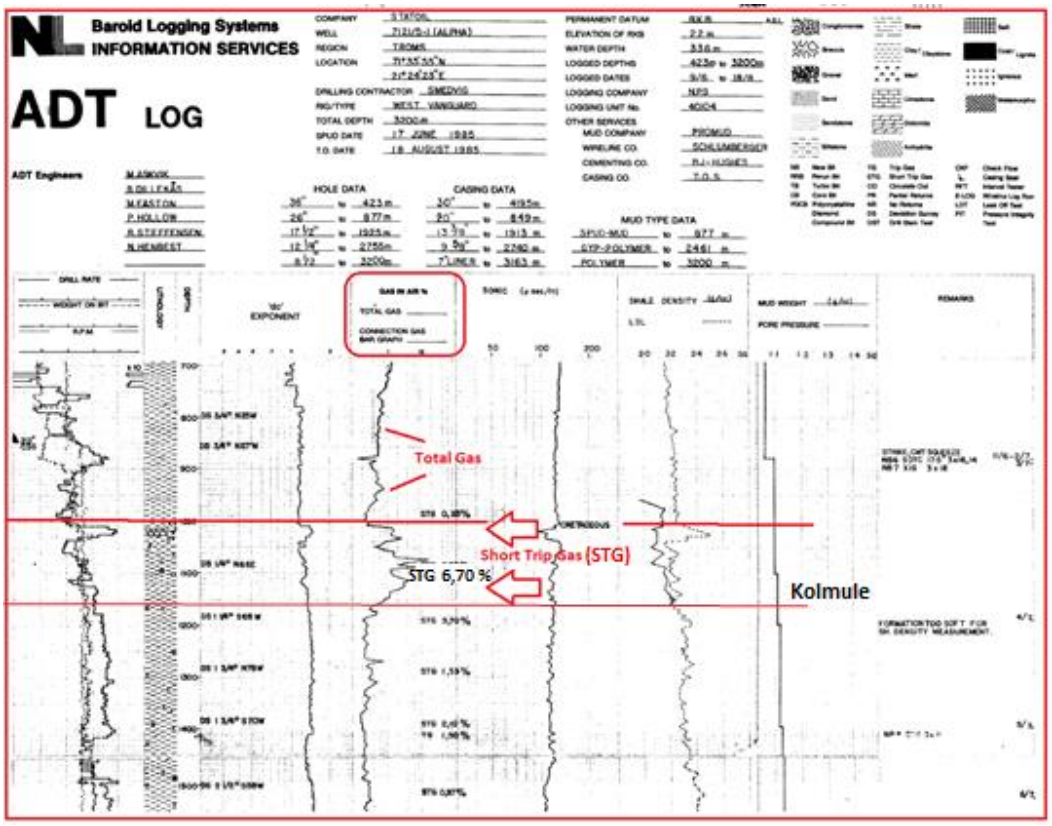

Figure 6-5 Gas readings showing the amount of short trip gas in upper Cretaceous sediments. These measurements are done during drilling: when the drill bit penetrates the rock, the drilled material along with oil, gas, water is carried back towards the surface by the drilling mud. Here it is separated into the cuttings and liquid mud, which are further analyzed providing total gas content (showed here) and gas composition (showed in **Figure 6-1**). Modified from end-of-well report, Statoil.

The two different sub-divisions of the anomaly discussed in **5.3.4,** are likely related to gas hydrates. The localization of the anomaly is measured just beneath the GHSZ in the area **(Figure 6-2),** and log data also indicates the presence of hydrates. **Figure 6-6** shows an enlarged excerpt of the log from well 7121/5-1 **(Figure 5-10)** and anomaly 4 in **Figure 5-21**. The theory of hydrates are based on the high amplitude at 660 ms, with normal polarity compared to the seafloor, indicating high density content (hard material) with the presence of gas hydrates, correlating with the log values at the same depth. The high amplitude below, which crosscuts the dipping layers, appearing patchier, more incoherent is interpreted to be remnants of a BSR.

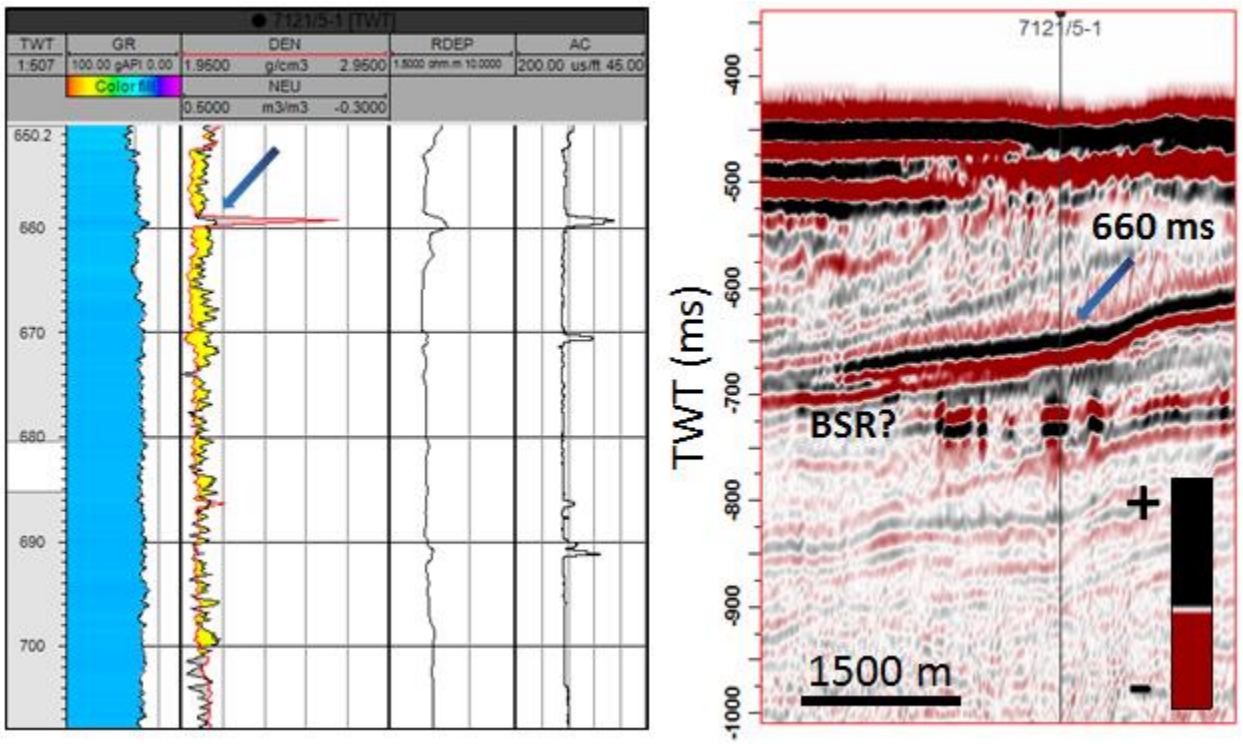

Figure 6-6 Left: Extracted log values from **Figure 5-10** showing a significant peak in values at 660 ms (twt). **Right:** A zoomed-in picture of **Figure 5-21**, showing where the peak originates from in the seismic section.

Anomaly 3, located on top of the largest gas chimney in the study (C1) is also interpreted as a possible BSR. The depth (712 meters) is very close to the bottom GHSZ and the appearance as crosscutting surrounding, dipping reflections is a good indicator of the presence of gas hydrates. The area beneath is affected by acoustic masking and wipe out effects, in addition to pulled-down reflections, classic evidence of a gas conducting chimneys, and a good indicator of the source to the hydrates and underlying free gas. The southern boundary of C1 coincides with the spill point of the Jurassic reservoir, bounded by two E-W trending major deep-seated faults (F4 and F5), observed penetrating the reservoir. This suggests that these faults possibly act as fluid migration pathways, together with C1, in to the shallower strata, which correlates with previous observations in this area (Mohammedyasin et al., 2016; Ostanin et al., 2017).

The anomaly is also bounded by minor, interconnected faults, reactivated in Paleocene – early Eocene. These act as fluid migration pathways, through the sealing hydrates and further towards the seabed via interpreted pipes. Evidence of this is the high density area of pockmarks **(Figure 5-26)**, located in the west, just above gas A3. These faults also looks to participate in the accumulation of anomaly 2, which is observed up-dip in a westward direction, from A3. It is also underlain by a major fault (F3), also reactivated in the late Jurassic to act as a possible conduit for fluid leakage out of the reservoir. It seems to

reach all the way up to Paleocene-early Eocene strata. Hence, F3 together with A3 are likely sources for the possible thermogenic gas accumulations causing the high amplitudes related to A2.

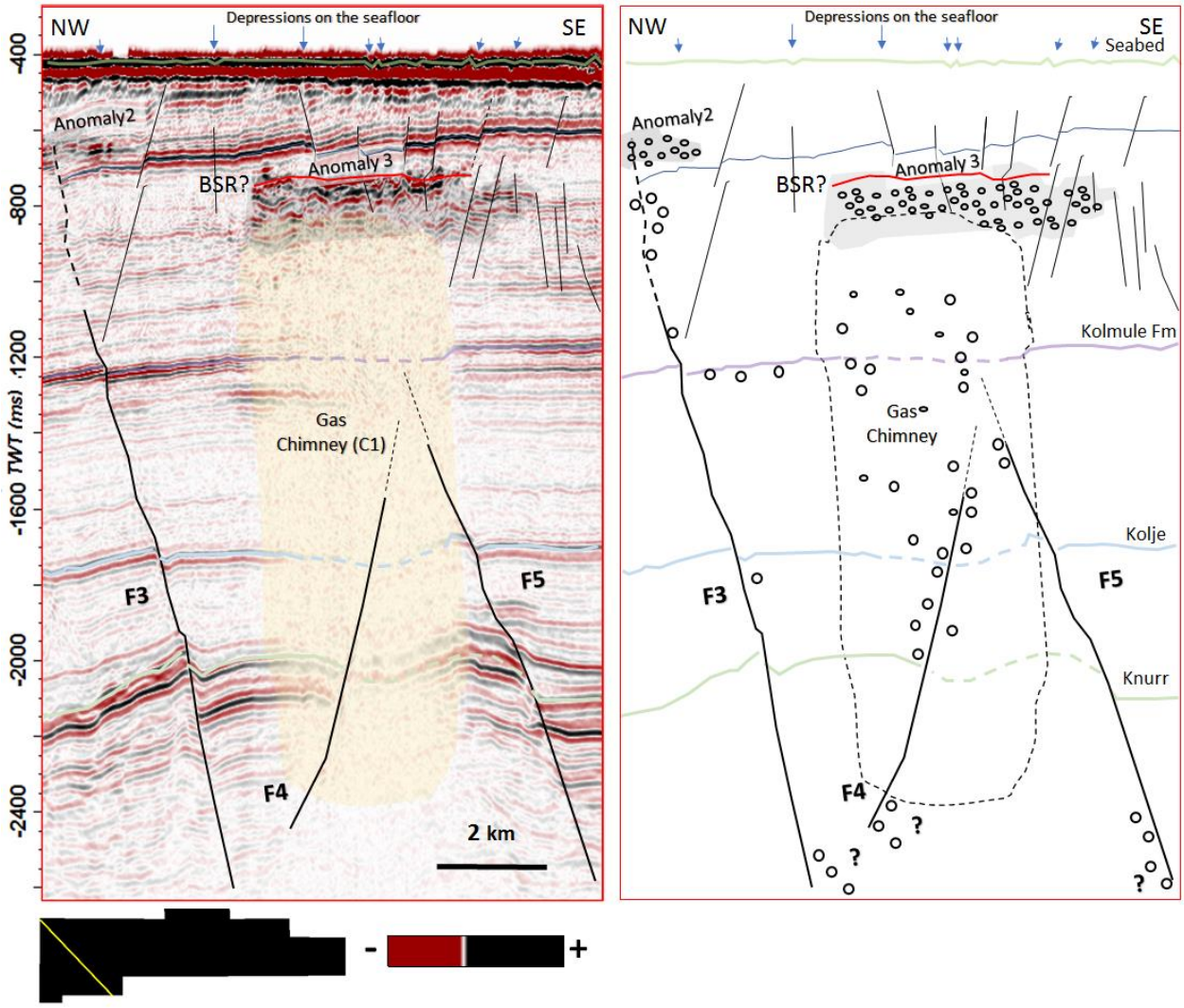

Figure 6-7 Conseptual model showing how anomaly 3 is fed by fluids from the underlying faults and gas chimney, and the location of A2, which presumably receives hydrocarbons from F3 and A3.

6.1.3 Timing and origin of the shallow gas and gas hydrates

Glacial processes and reactivation of faults play an important role in the origin of the shallow gas and gas hydrates located above the deep-seated reservoir. Due to the residual oil columns found beneath the gas field it is indicated that these structures earlier where oil bearing, hence have experienced leakage (Jan Inge Faleide et al., 2008; Linjordet et al., 1992; Ostanin et al., 2012).

The change in dip observed along the deep-seated, major faults **(5.2.1)** seem to occur approximately at the same periods, with most abundant in the reservoir units, separating the upper Jurassic sediments in horst and graben structures **(Figure 5-15).** These reactivations is linked to the leakage from deeper structures, as frequently periods of fault reactivation is known to cause fractures and breccations, hence increasing porosity and permeability across fault planes (Mohammedyasin et al., 2016).

During middle Pleistocene, eight full scale glaciations occurred (Knies et al., 2009; Laberg et al., 2010), being a possible explanation of the observed reactivated faults, as severe erosion and uplift leads to gas expansion and pressure increase. Episodes of glacial loading, approximately 1 Ma years ago, is suggested to increase the pressure of the overburden, thus leading to solution of the gas. Some of the fluid were potential lost due to capillary leakage through the fractured structures. The formation of gas hydrates occurred beneath the ice sheet due to favorable temperature and pressure conditions and worked as a trapping mechanism for free gas accumulating below **(Figure 6-8A)**.

The following deglaciation events removed weight from the reservoir, resulting in expansion of the gas. The removal of sediments (unloading) is thought to increase horizontal compressive stress (Gudmundsson, 2011), which in turn results in increased pore pressure beyond the hydrostatic level (overpressure). The capillary pressure **(2.1.3)** is thus exceeded, resulting in possible leakage out of the reservoir **(Figure 6-8B)**. As migration is likely to escape through faults, rather than through hydrofractures in the caprock (Løtveit, 2009), this is the suggested scenario in this study.

During deglaciation the decreased pressure and increased temperature resulted in gas hydrate dissociation and reduced GHSZ (Crémière et al., 2016), liberating the methane from the gas hydrate deposits. The destabilized free gas possibly escaped through the shallow plumbing system, resulting in the formation of pockmarks on the seabed, e.g. **Figure 5-26**.

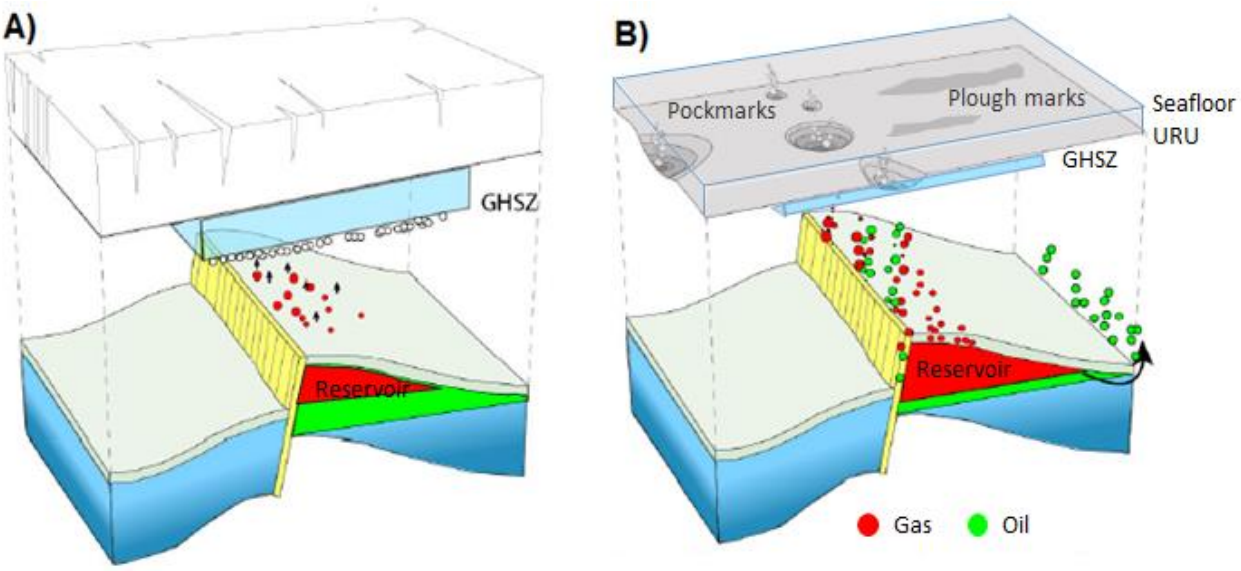

Figure 6-8 A) Glacial loading, pressure increase and gas going into solution. **B)** Glacial unloading, hydrocarbon migration through cap rock, along faults and over spill point. Modified from (Ostanin et al., 2017).

6.2 Leakage from reservoir, safe to store CO_2?

This study indicates clear relationship between the observed bright spots in the shallow strata, and deeper structures in the Snøhvit field, and suggest that leakage has occurred from the reservoir. Regarding the safety of CO_2 sequestration, the study also suggests that most of the shallow gas was migrating in relation to the glaciation/deglaciation periods in the Cenozoic, through reactivated faults, supported by the conceptual model and other studies (Mohammedyasin et al., 2016; Ostanin et al., 2017; Ostanin et al., 2013).

Due to the CO_2 injection at the Snøhvit reservoir, it is important to know that the cap rock and faults intersecting the area are sealing. An analytical model was used to screen the potential of fluid leakage of the two faults located closest to the CO_2 injector, Fault 1 and Fault 2 **(Figure 4-6).** The leak off factor is found in **Table 5-1** and shows that the faults are tight. It was also shown that the leak off coefficient decreases with increased distance to the injector. The results of this study therefore suggests that faults further away from the injector has less flow potential than F1 and F2.

The sensitivity study gave an insight in the most important parameters when it comes to leakages of CO_2 through faults. The study identified the importance of the reservoir permeability, the fault permeability and the thickness of the reservoir. The most important parameter seems to be the reservoir permeability, where it is indicated a significant risk of injecting CO_2 in a low permeable reservoir with an overlaying caprock with high permeability. For reservoirs with low permeability it seems like reservoir thickness can be a compensating factor. It is also suggested that the fault permeability becomes less important if the overlaying aquifer has low permeability and hence low flow potential.

This study suggests that a better understanding of the behavior of CO_2 leakage can mitigate the risk of storing carbon dioxide in the subsurface. This is essential for the widespread implementation of carbon capture and storage.

7 Conclusion

The aim of this thesis was to map and interpret fluid features above the Snøhvit field to obtain a better understanding of the processes controlling the fluid flow, the provenance of the gas and the interplay between shallow fluid accumulations and deep hydrocarbon reservoir. Many fluid flow phenomena occur in the study area. Pockmarks, gas chimneys and high amplitude anomalies was mapped out together with deep seated and shallow faults (F1 – F7) found in the data set. Four amplitude anomalies (A1 – A4) have been described and interpreted as potential accumulations of shallow gas. These anomalies were discussed in relation to deep seated faults penetrating the reservoir and a theory of gas migrating pathways was made.

It is suggested that the deep-seated faults played a key role in transporting the gas to shallower depths, via reactivated faults, into the late Cretaceous strata known as the Knurr – Kolmule Formation, where it migrated further via the polygonal and shallow faults until it hit impermeable rock. When it comes to timing it was found that most of the leakage took place during the cycles of glacial loading and unloading in the Cenozoic. During the loading the gas in the reservoir went into solution as the overburden pressure increased. Some of the fluid was potentially lost due to capillary leakage through the caprock. Due to favorable pressure and temperature conditions gas hydrates formed below the ice sheet. The following deglaciation events removed weight from the reservoir. As a result the gas came out of solution, expanded and migrated along migrated faults. Some oil also spilled from the structure as a result of gas expansion. Methane, liberated from the gas hydrate deposits because of decreased pressure and increased temperature, formed pockmarks on the seabed.

Another essential element was to investigate the leakage potential from the reservoir today, as CO_2 is injected into the Snøhvit reservoir for storage. An analytical model was carried out, showing that the leakage potential for two faults located 600 and 1800 meters from the injector was low. It was also showed that the leakage potential decreased the further away from the injection point the faults were located. A sensitivity study was carried out too give an insight in the most important parameters influencing leakage through faults. The parameters identified was the reservoir permeability, the fault permeability and the leakage through faults. To minimize the risk of fluid leakage, it is suggested in this study that it is important to understand the drive mechanisms of fluid migration and understand how and when fluid leakage from the reservoir occur. Monitoring the fluid flow by 4D-seismic is important, together with measurements of the pressure and injection volume of the CO_2 injector.

To summarize – there has been fluid leakage from the Snøhvit reservoir into the overburden in the past, but there is no evidence of leakage in the present. Nevertheless, future leakage from the reservoir cannot be excluded, but it is not going to happen in the next 100-1000 years which is the criterion for a secure storage site.

References

Ablard, P., Bell, C., Cook, D., Fornasier, I., Poyet, J.-P., Sharma, S., Fielding, K., Lawton, L., Haines, G., & Herkommer, M. A. (2012). The expanding role of mud logging. *Oilfield Review, 24*(1), 24-41.

Aboholi, E. M. (Producer). (2016). Youtube: Oil & Well Kick. Retrieved from https://www.youtube.com/watch?v=816YoGEAtM4

Andersen, L. B. (1998). Stochastic modelling for the analysis of blowout risk in exploration drilling. *Reliability Engineering & System Safety, 61*(1-2), 53-63.

Andreassen, K. (2009). *GEO-3123 Marin Geophysics Kompendium*. Retrieved from Tromsø:

Andreassen, K., Nilssen, E. G., & Ødegaard, C. M. (2007, 4 5). Analysis of shallow gas and fluid migration within the Pilo-Pleistocene sedimentary succession of the SW Barents Sea continental margin using 3D seismic data. *Geo-Mar Lett*, 155-171.

Apps, J. A., & van de Kamp, P. C. (1993). Energy gases of abiogenic origin in the Earth's crust. *US Geol Surv Prof Paper, 1570*, 81-132.

Badley, M. E. (1985). Practical seismic interpretation.

Beard, D., & Weyl, P. (1973). Influence of texture on porosity and permeability of unconsolidated sand. *AAPG bulletin, 57*(2), 349-369.

Bennison, G. M., Olver, P. A., & Moseley, K. A. (2013). *An introduction to geological structures and maps*: Routledge.

Benson, S. M., & Orr, F. M. (2008). Carbon dioxide capture and storage. *Mrs Bulletin, 33*(4), 303-305.

Berglund, L., Augustson, J., Færseth, R., Gjelberg, J., & Ramberg-Moe, H. (1986). The evolution of the Hammerfest Basin. *Habitat of Hydrocarbons on the Norwegian Continental Shelf. Graham & Trotman, London*, 319-338.

Berglund, L. T., Augustson, J., Færseth, R., & Ramberg-Moe, H. (1986). The evolution of the Hammerfest Basin. *Habitat of Hydrocarbons on the Norwegian Continental Shelf. Graham & Trotman, London*, 319-338.

Berndt, C. (2005). Focused fluid flow in passive continental margins. *Philosophical Transactions of the Royal Society of London A: Mathematical, Physical and Engineering Sciences, 363*(1837), 2855-2871.

Berndt, C., Bünz, S., & Mienert, J. (2003). Polygonal fault systems on the mid-Norwegian margin: a long-term source for fluid flow. *Geological Society, London, Special Publications, 216*(1), 283-290.

Biddle, K. T., & Wielchowsky, C. C. (1994). Hydrocarbon Traps. In L. B. Magoon & W. G. Dow (Eds.), *The Petroleum System - From source to trap* (pp. 219-235): American Association of Petroleum Geologists.

Bilat, J. (2005). *Some considerations on the interpretation of seabed images based on commercial 3D seismic in the Faroe-Shetland Channel*. Retrieved from Edinburgh:

Bjørlykke, K. (2010). Petroleum Migration. *Springer - Petroleum Geoscience,* 349-360.

Breivik, A. J., Faleide, J. I., & Gudlaugsson, S. T. (1998). Southwestern Barents Sea margin: late Mesozoic sedimentary basins and crustal extension. *Tectonophysics, 293*(1-2), 21-44.

Brown, A. R., Brown, A. R., Brown, A. R., Géophysicien, E.-U., & Brown, A. R. (1996). Interpretation of three-dimensional seismic data.

Bryan, G. M. (1974). In situ indications of gas hydrate. In *Natural gases in marine sediments* (pp. 299-308): Springer.

Buller, A. T., Bjørkum, P. A., Nadeau, P., & Walderhaug, O. (2005). *Distribution of hydrocarbons in sedimentary basins - the importance of temperature*. Retrieved from

Bünz, S., Mienert, J., & Berndt, C. (2003). Geological controls on the Storegga gas-hydrate system of the mid-Norwegian continental margin. *Earth and Planetary Science Letters, 209*(3-4), 291-307.

Carstens, H. (2005). Fra problem - til mulighet.

Cartwright, J. (2011). Diagenetically induced shear failure of fine-grained sediments and the development of polygonal fault systems. *Marine and Petroleum Geology, 28*(9), 1593-1610.

Cartwright, J., Huuse, M., & Aplin, A. (2007). Seal bypass systems. *AAPG bulletin, 91*(8), 1141-1166.

Cartwright, J., & Santamarina, C. (2015). Seismic characteristics of fluid escape pipes in sedimentary basins: Implications for pipe genesis. *Elsevier - Marine and Petroleum Geology, 65*, 126-140.

Cathles, L. M., Su, Z., & Chen, D. (2010). The physics of gas chimney and pockmark formation, with implications for assessment of seafloor hazards and gas sequestration. *Elsevier - Marine and Petroleum Geology, 27*(1), 82-91.

Cavanagh, A. J., Di Primio, R., Scheck-Wenderoth, M., & Horsfield, B. (2006). Severity and timing of Cenozoic exhumation in the southwestern Barents Sea. *Journal of the Geological Society, 163*(5), 761-774.

Claypool, G. E., & Kaplan, I. (1974). The origin and distribution of methane in marine sediments. In *Natural gases in marine sediments* (pp. 99-139): Springer.

Crémière, A., Lepland, A., Chand, S., Sahy, D., Condon, D. J., Noble, S. R., Martma, T., Thorsnes, T., Sauer, S., & Brunstad, H. (2016). Timescales of methane seepage on the Norwegian margin following collapse of the Scandinavian Ice Sheet. *Nature communications, 7*, 11509.

Dalland, A. (1988). A lithostratigraphic scheme for the Mesozoic and Cenozoic succesion offshore Norway north of 62° N. *Norw. Petrol. Dir. Bull.*

Davies, R. J., & Ireland, M. T. (2011). Initiation and propagation of polygonal fault arrays by thermally triggered volume reduction reactions in siliceous sediment. *Marine Geology, 289*(1-4), 150-158.

Davis, A. M. (1992, 10). Shallow gas: an overview. *Elsevier - Continental Shelf Research*, 1077-1079.

Demaison, G., & Huizinga, B. J. (1991). Genetic classification of petroleum systems (1). *AAPG bulletin, 75*(10), 1626-1643.

Dewhurst, D. N., Cartwright, J. A., & Lonergan, L. (1999). The development of polygonal fault systems by syneresis of colloidal sediments. *Marine and Petroleum Geology, 16*(8), 793-810.

Dimakisa, P., Braathenb, B. I., Falaidec, J. I., Elverhøid, A., & Gudlaugssone, S. T. (1998, 12 31). Cenozoic erosion and the preglacial uplift of the Svalbard–Barents Sea region. *Elsevier - Tectonophysics*, 311-327.

Doré, A., Scotchman, I., & Corcoran, D. (2000). Cenozoic exhumation and prediction of the hydrocarbon system on the NW European margin. *Journal of Geochemical Exploration, 69*, 615-618.

Dore, A. G. (1995). *Barents Sea Geology, Petroleum Resources and Commercial Potential*. Retrieved from Stavanger:

Doré, A. G. (2002). *Exhumation of the North Atlantic margin: timing, mechanisms and implications for petroleum exploration*.

Dorè, A. G., & Jensen, L. N. (1996). The impact of late Cenozoic uplift and erosion on hydrocarbon. *Elsevier - Global and Planetary Change*, 415-436.

Dow, W. G. (1974). Application of oil-correlation and source-rock data to exploration in Williston Basin. *AAPG bulletin, 58*(7), 1253-1262.

Duran, E. R., Primio, R. d., Anka, Z., Stoddart, D., & Horsfield , B. (2013a). 3D-basin midelling of the Hammerfest Basin (southwestern Barents Sea): A quantitative assesment of petroleum generation, migration and leakage. *Elsevier - Marine and Petroleum Geology*, 281-303.

Duran , E. R., Primio, R. d., Anka, Z., Stoddart, D., & Horsfield, B. (2013b). Petroleum system analysis of the Hammerfest Basin (southwestern Barents Sea): comparison of basin modelling and geochemical data. *Elsevier - Organic Geochemestry*, 105-121.

Earle, S. (2015). *Physical Geology*. Gabriola Island: BC Open Textbook Project.

England, W., Mackenzie, A., Mann, D., & Quigley, T. (1987). The movement and entrapment of petroleum fluids in the subsurface. *Journal of the Geological Society, 144*(2), 327-347.

Equinor. (2018). Snøhvit. Retrieved from https://www.equinor.com/no/hva-vi-gjoer/norwegian-continental-shelf-platforms/snohvit.html

Etiope, G., & Lollar, B. S. (2013, 6 26). Abiotic methane on Earth. *Reviews of geophysics*, 276-299.

Faleide, J. I., Gudlaugsson, S. T., & Jacquart, G. (1984a). Evolution of the western Barents Sea. *Marine and Petroleum Geology, 1*(2), 123-150.

Faleide, J. I., Gudlaugsson, S. T., & Jacquart, G. (1984b). Evolution of the western Barents Sea. *Elsevier - Marine and Petroleum Geology, 1*(2), 123-150.

Faleide, J. I., Tsikalas, F., Breivik, A. J., Mjelde, R., Ritzmann, O., Engen, O., Wilson, J., & Eldholm, O. (2008). Structure and evolution of the continental margin off Norway and the Barents Sea. *Episodes, 31*(1), 82-91.

Faleide, J. I., Vågnes, E., & Gudlaugsson, S. T. (1993). *Late Mesozoic-Cenozoic evolution of the south-western Barents Sea in a regional rift-shear tectonic setting*. Retrieved from Oslo:

Floodgate, G. D., & Judd, A. G. (1992, 15 1). The origins of shallow gas. *Continental Shelf Reseach*, 1145-1156.

Fossen, H., & Gabrielsen, R. (2005). Strukturgeologi. *Fagbokforlaget, Bergen*.

Furre, A.-K., Eiken, O., Alnes, H., Vevatne, J. N., & Kiær, A. F. (2017). 20 Years of Monitoring CO2-injection at Sleipner. *Energy Procedia, 114*, 3916-3926.

Gabrielsen, R. H., Faerseth, R. B., Jensen, L. N., Kalheim, J. E., & Riis, F. (1990). *Structural Elements of the Norwegian Continental Shelf. Pt. 1. The Barents Sea Region*: Norwegian Petroleum Directorate.

Gay, A., Lopez, M., Cochonat, P., Séranne, M., Levaché, D., & Sermondadaz, G. (2006). Isolated seafloor pockmarks linked to BSRs, fluid chimneys, polygonal faults and stacked Oligocene–Miocene turbiditic palaeochannels in the Lower Congo Basin. *Marine Geology, 226*(1-2), 25-40.

Goulty, N. (2008). Geomechanics of polygonal fault systems: a review. *Petroleum Geoscience, 14*(4), 389-397.

Grinrod, M., Haaland, O., & Ellingsen, B. (1988). *A shallow gas research program.* Paper presented at the SPE/IADC Drilling Conference.

Groshong Jr, R. H. (2006). *3-D structural geology*: Springer.

Gudlaugsson, S. T., Faleide, I. J., & Breivik, A. J. (1998). Late Palaeozoic structural development of the South-western Barents Sea. In *Marine and Petroleum Geology* (pp. 73-102). Oslo: Elsevier.

Gudmundsson, A. (2011). *Rock fractures in geological processes*: Cambridge University Press.

Gussow, W. C. (1954, 5). Differential entrapment of oil and gas: a fundamental principle. *Bulletin of the American Association of Petroleum Geologists,* 816-853.

Guzzetta, G., & Cinquergrana, R. E. (1987, 5 5). "Fluid tectonics": a little appreciated facet of buoyancy tectonics. *Elsevier - Tectonophysics,* 321-324.

Hammerschmidt, E. G. (1934). Formation of gas hydrates in natural gas transmission lines. *Industrial & Engineering Chemistry, 26*(8), 851-855.

Hansen, J., Sato, M., Ruedy, R., Lacis, A., & Oinas, V. (2000). *Global warming in the twenty-first century: An alternative scenario*. Retrieved from New York:

Hansen, O., Eiken, O., Østmo, S., Johansen, R. I., & Smith, A. (2011). Monitoring CO2 injection into a fluvial brine-filled sandstone formation at the Snøhvit field, Barents Sea. In *SEG Technical Program Expanded Abstracts 2011* (pp. 4092-4096): Society of Exploration Geophysicists.

Hansen, O., Gilding, D., Nazarian, B., Osdal, B., Ringrose, P., Kristoffersen, J.-B., Eiken, O., & Hansen, H. (2013). Snøhvit: The history of injecting and storing 1 Mt CO2 in the fluvial Tubåen Fm. *Energy Procedia, 37*, 3565-3573.

Henriet, J., De Batist, M., De Bruyne, H., Heldens, P., Huylebroeck, J., Mostaert, F., Sevens, E., Auffret, J., & D'OLIER, B. (1989). Preliminary seismic-stratigraphic maps and type sections of the Paleogene deposits in the Southern Bight of the North Sea. *The Quaternary and Tertiary Geology of the Southern Bight, North Sea. Belgian Geological Survey, Ministry Economic Affairs (Brussels)*, 29-44.

Henriksen, E., Ryseth, A., Larssen, G., Heide, T., Rønning, K., Sollid, K., & Stoupakova, A. (2011). Tectonostratigraphy of the greater Barents Sea: implications for petroleum systems. *Geological Society, London, Memoirs, 35*(1), 163-195.

Herzog, H., & Golomb, D. (2004). Carbon capture and storage from fossil fuel use. *Encyclopedia of energy, 1*(6562), 277-287.

Hindle, A. D. (1997). Petroleum migration pathways and charge concentration: A three-dimensional model. *AAPG bulletin, 81*(9), 1451-1481.

Hovland, M. (1982). Pockmarks and the recent geology of the central section of the Norwegian trench. *Elsevier - Marine Geology, 47*, 283-301.

Hovland, M., & Judd, A. (1988). *Seabed pockmarks and seepages: impact on geology, biology, and the marine environment*: Springer.

Hovland, M., & Judd, A. G. (1988). *Seabed Pockmarks and Seepages*. Retrieved from London:

Hubbert, M. K. (1940). The theory of ground-water motion. *The Journal of Geology, 48*(8, Part 1), 785-944.

Hubbert, M. K. (1956). Darcy's law and the field equations of the flow of underground fluids.

Hustoft, S., Mienert, J., Bünz, S., & Nouzé, H. (2007). High-resolution 3D-seismic data indicate focussed fluid migration pathways above polygonal fault systems of the mid-Norwegian margin. *Marine Geology, 245*(1-4), 89-106.

Hyndman, R., Foucher, J., Yamano, M., & Fisher, A. (1992a). Deep sea bottom-simulating-reflectors: calibration of the base of the hydrate stability field as used for heat flow estimates. *Earth and Planetary Science Letters, 109*(3-4), 289-301.

Hyndman, R. D., & Davis, E. E. (1992b). A mechanism for the formation of methane hydrate and seafloor bottom-simulating reflectors by vertical fluid expulsion. *Journal of Geophysical Research: Solid Earth, 97*(B5), 7025-7041.

Jenden, P., Kaplan, I., Hilton, D., & Craig, H. (1993). Abiogenic hydrocarbons and mantle helium in oil and gas fields. *United States Geological Survey, Professional Paper;(United States), 1570*.

Judd, A., & Hovlan, M. (2007). *Seabed Fluid Flow: The impact on Geology, Biology and the Marine Environment*: Cambridge University Press.

Judd, A., & Hovland, M. (1992). The evidence of shallow gas in marine sediments. *Continental Shelf Research, 12*(10), 1081-1095.

Kanestrøm, R., Skålnes, Å., Riste, P., Eide, T., & Strandenes, S. (1990). Prediction of Shallow Gas from Seismic Data. *Norsk Hydro A/S, reseach Centre*, 211-232.

Kearey, P., Brooks, M., & Hill, I. (2002). *An Introduction to Geophysical Exploration*: Blackwell Science Ltd.

King, L. H., & MacLEAN, B. (1970). Pockmarks on the Scotian shelf. *Geological Society of America Bulletin, 81*(10), 3141-3148.

Knies, J., Matthiessen, J., Vogt, C., Laberg, J. S., Hjelstuen, B. O., Smelror, M., Larsen, E., Andreassen, K., Eidvin, T., & Vorren, T. O. (2009). The Plio-Pleistocene glaciation of the Barents Sea–

Svalbard region: a new model based on revised chronostratigraphy. *Quaternary Science Reviews, 28*(9), 812-829.

Kvenvolden, K. A. (1993). Gas hydrates—geological perspective and global change. *Reviews of geophysics, 31*(2), 173-187.

Kvenvolden, K. A. (1993b). A primer on gas hydrates. *US Geological Survey professional paper, 1570*, 279-292.

Kvenvolden, K. A., & McMenamin, M. A. (1980). Hydrates of natural gas: a review of their geologic occurrence.

Laberg, J. S., Andreassen, K., Knies, J., Vorren, T. O., & Winsborrow, M. (2010). Late Pliocene–Pleistocene development of the Barents Sea ice sheet. *Geology, 38*(2), 107-110.

Laberg, J. S., Andreassen, K., & Vorren, T. O. (2012). Late Cenozoic erosion of the high-latitude southwestern Barents Sea shelf revisited. *Bulletin, 124*(1-2), 77-88.

Larsen, R. M., Fjæran, T., & Skarpnes, O. (1993). Hydrocarbon potential of the Norwegian Barents Sea based on recent well results. In *Norwegian Petroleum Society Special Publications* (pp. 321-331): Elsevier.

Larssen, G., Elvebakk, G., Henriksen, L. B., Kristensen, S., Nilsson, I., Samuelsberg, T., Svånå, T., Stemmerik, L., & Worsley, D. (2002). Upper Palaeozoic lithostratigraphy of the Southern Norwegian Barents Sea. *Norwegian Petroleum Directorate Bulletin, 9*, 76.

Ligtenberg, J. (2005). Detection of fluid migration pathways in seismic data: implications for fault seal analysis. *Basin Research, 17*(1), 141-153.

Lin, D. A. T. (2012). Seismic Stratigraphy. In. Taoyuan City: National Central Univ., Department of Earth Sciences.

Linjordet, A., & Olsen, R. G. (1992). The Jurassic Snohvit Gas Field, Hammerfest Basin, Offshore Northern Norway: Chapter 22.

Lonergan, L., & Cartwright, J. A. (1999). Polygonal faults and their influence on deep-water sandstone reservoir geometries, Alba Field, United Kingdom central North Sea. *AAPG bulletin, 83*(3), 410-432.

Løseth, H., Gading, M., & Wensaas, L. (2009). Hydrocarbon leakage interpreted on seismic data. *Elsevier - Marine and Petroleum Geology, 26*(7), 1304-1319.

Løtveit, I. F. (2009). Analytical and numerical studies of fluid reservoirs and fracture development in heterogeneous rocks.

Magoon, L. B. (1988). The petroleum system—a classification scheme for research, exploration, and resource assessment. *Petroleum systems of the United States: US Geological Survey Bulletin, 1870*, 2-15.

Magoon, L. B., & Beaumont, E. A. (1999). Petroleum Systems. In E. A. Beaumont & N. H. Foster (Eds.), *Exploring for Oil and Gas Traps* (pp. 3-34): American Association of Petroleum Geologists.

Magoon, L. B., & Dow, W. G. (1994). The petroleum system: chapter 1: Part I. Introduction.

Makagon, Y. F. (2010). Natural gas hydrates – A promising source of energy. *Elsevier - Journal of Natural Gas Science and Engineering, 2*(1), 49-59.

Mansfield, C., & Cartwright, J. (1996). High resolution fault displacement mapping from three-dimensional seismic data: evidence for dip linkage during fault growth. *Journal of Structural Geology, 18*(2-3), 249-263.

Meldahl, P., Heggeland, R., Bril, B., & de Groot, P. (2001). Identifying faults and gas chimneys using multiattributes and neural networks. *The Leading Edge, 20*(5), 474-482.

Metz, B. (2005). *Carbon dioxide capture and storage: special report of the intergovernmental panel on climate change*: Cambridge University Press.

Miljødirektoratet. (2016). *Vedtak om tillatelse til lagring av CO2 på Snøhvitfeltet*. Retrieved from

Miller, S. L. (1974). The nature and occurrence of clathrate hydrates. In *Natural Gases in Marine Sediments* (pp. 151-177): Springer.

Mohammedyasin, S., Lippard, S., Omosanya, K., Johansen, S., & Harishidayat, D. (2016). Deep-seated faults and hydrocarbon leakage in the Snøhvit Gas Field, Hammerfest Basin, southwestern Barents Sea. *Marine and Petroleum Geology, 77*, 160-178.

Moore, J. C. (1989). Tectonics and hydrogeology of accretionary prisms: role of the décollement zone. *Journal of Structural Geology, 11*(1-2), 95-106.

Müller, S., Reinhardt, L., Franke, D., Gaedicke, C., & Winsemann, J. (2018). Shallow gas accumulations in the German North Sea. *Elsevier - Marine and Petroleum Geology, 91*, 139-151.

Nadeau, P. H. (2011). *Earth's energy "Golden Zone": a synthesis from mineralogical research*. Retrieved from Aberdeen:

ndla (Producer). (2017). BOP (Blow Out Preventer). Retrieved from https://ndla.no/nb/node/162400?fag=137414

Negrescu, M. (2008). Economic Modeling of an Oil and Gas Project Involving Carbon Capture and Storage: Snohvit LNG Field (Barents Sea, Norway). *SPE Projects, Facilities & Construction, 3*(02), 1-15.

Nilsen, K. T., Vendeville, B. C., & Johansen, J.-T. (1995). Influence of regional tectonics on halokinesis in the Nordkapp Basin, Barents Sea.

NPD (Producer). (2017). FactMaps, Norwegian Petroleum Directorate. Retrieved from http://www.npd.no/no/Kart/Faktakart/

Ohm, S. E., Karlsen, D. A., & Austin, T. (2008). Geochemically driven exploration models in uplifted areas: Examples from the Norwegian Barents Sea. *AAPG bulletin, 92*(9), 1191-1223.

Ostanin, I., Anka, Z., & di Primio, R. (2017). Role of Faults in Hydrocarbon Leakage in the Hammerfest Basin, SW Barents Sea: Insights from Seismic Data and Numerical Modelling. *Geosciences, 7*(2), 28.

Ostanin, I., Anka, Z., di Primio, R., & Asdrùbal, B. (2013). Hydrocarbon plumbing system above the Snøhvit gas field: Structural control and implications for thermogenic methane leakage in the Hammerfest basin, SW Barents Sea. *Marine and Petroleum Geology*.

Ostanin, I., Anka, Z., di Primio, R., & Bernal, A. (2012). Identification of a large Upper Cretaceous polygonal fault network in the Hammerfest basin: Implications on the reactivation of regional faulting and gas leakage dynamics, SW Barents Sea. *Marine Geology, 332*, 109-125.

Parson, E. A., & Keith, D. W. (1998). Fossil fuels without CO2 emissions. In: American Association for the Advancement of Science.

Pecher, I. A., Minshull, T. A., Singh, S. C., & von Huene, R. (1996). Velocity structure of a bottom simulating reflector offshore Peru: Results from full waveform inversion. *Earth and Planetary Science Letters, 139*(3-4), 459-469.

Pegaz-Fiornet, S., Carpentier, B., Michel, A., & Wolf, S. (2012). Comparison between the different approaches of secondary and tertiary hydrocarbon migration modeling in basin simulators.

Perrodon, A. (1983). *Dynamics of oil and gas accumulations* (Vol. 5): Editions TECHNIP.

Perrodon, A. (1992). Petroleum systems: models and applications. *Journal of Petroleum Geology, 15*(3), 319-325.

Peters, K. E., Curry, D. J., & Kacewicz, M. (2012). An overview of basin and petroleum system modeling: Definitions and concepts.

Petracchini, L., Antonellini, M., Billi, A., & Scrocca, D. (2015). Syn-thrusting polygonal normal faults exposed in the hinge of the Cingoli anticline, northern Apennines, Italy. *Frontiers in Earth Science, 3*, 67.

PSA (Producer). (2007). Better overview over shallow incidents. Retrieved from http://www.ptil.no/news/better-overview-over-shallow-gas-incidents-article3146-878.html

PSA, P. S. A. N.-. (2007). *Shallow gas events 1984 - 2006 in the Norwegian Sector*. Retrieved from

Rice, D. D., & Claypool, G. E. (1981). Generation, accumulation, and resource potential of biogenic gas. *AAPG bulletin, 65*(1), 5-25.

Rise, L., Valèrie, B. K., Chand, S., & Bøe, R. (2015). *Pockmarks in the southwestern Barents Sea and Finnmark fjords*. Retrieved from Trondheim:

Rutter, E., Holdsworth, R., & Knipe, R. (2001). The nature and tectonic significance of fault-zone weakening: an introduction. *Geological Society, London, Special Publications, 186*(1), 1-11.

Schmidt, V., & Mcdonald, D. A. (1979). Texture and recognition of secondary porosity in sandstones.

Schowalter, T. T. (1979). Mechanics of secondary hydrocarbon migration and entrapment. *AAPG bulletin, 63*(5), 723-760.

Schroot, B. M., & Schüttenhelm, R. T. E. (2003). Shallow gas and gas seepage: expressions on seismic and other acoustic data from the Netherlands North Sea. *Journal of Geochemical Exploration*, 305-309.

Selley, R. C., & Sonnenberg, S. A. (2015). *Elements of Petroleum Geology*: Academic Press (an imprint of Elsevier).

Sheriff, R. (1985). Aspects of Seismic Resolution: Chapter 1.

Sheriff, R. E. (2002). *Encyclopedic dictionary of applied geophysics*: Society of exploration geophysicists.

Shipley, T. H., Houston, M. H., Buffler, R. T., Shaub, F. J., McMillen, K. J., Ladd, J. W., & Worzel, J. L. (1979). Seismic evidence for widespread possible gas hydrate horizons on continental slopes and rises. *AAPG bulletin, 63*(12), 2204-2213.

Sills, G. C., & Wheeler, S. J. (1992). The significance of gas for offshore operations *Continental Shelf Reseach*, 1239-1250.

Sloan, J., E. Dendy. (1998). Gas Hydrates: Review of Physical/Chemical Properties. *Energy & Fuels, 12*(2), 191-196.

Smelror, M., Petrov, O., Larssen, G. B., & Werner, S. (2009). *Geological history of the Barents Sea*. Trondheim: Geological Survey of Norway.

Smith, M., Harland, W., & Dowdeswell, E. (1988). Geological Evolution of the Barents Shelf Region.

Solheim, A., & Larsson, F. R. (1987). *Seismic indicators of shallow gas in the Northern Barents Sea*. Retrieved from Oslo:

Steeneveldt, R., Berger, B., & Torp, T. (2006). CO2 capture and storage: closing the knowing–doing gap. *Chemical Engineering Research and Design, 84*(9), 739-763.

Tasianas, A., Marens, I., Bünz, S., & Mienert, J. (2016). Mechanisms initiating fluid migration at Snøhvit and Albatross fields, Barents Sea.

Telford, W. M., Geldart, L. P., & Sheriff, R. E. (1990). *Applied Geophysics*: Cambridge University Press.

Tissot, B. P., & Welte, D. H. (1984). *Petroleum formation and occurance*. Berlin, Heidelberg, New York, Tokyo: Springer-Verlag.

Tvedt, A. B., Rotevatn, A., Jackson, C. A.-L., Fossen, H., & Gawthorpe, R. L. (2013). Growth of normal faults in multilayer sequences: a 3D seismic case study from the Egersund Basin, Norwegian North Sea. *Journal of Structural Geology, 55*, 1-20.

Twiss, R. J., & Moores, E. M. (1992). *Structural geology*: Macmillan.

Twiss, R. J., & Moores, E. M. (2006). *Structural Geology* (2 ed.): W.H Freeman Co Ltd.

Vadakkepuliyambatta, S., Bünz, S., Mienert, j., & Chand, S. (2013). Distribution of subsurface fluid-flow systems in the SW Barents Sea. *Elsevier - Marine and Petroleum Geology*, 208-221.

Vadakkepuliyambatta, S., Chand, S., & Bünz, S. (2017). The history and future trends of ocean warming-induced gas hydrate dissociation in the SW Barents Sea. *Geophysical Research Letters, 44*(2), 835-844.

Vilarrasa, V., Silva, O., Carrera, J., & Olivella, S. (2013). Liquid CO2 injection for geological storage in deep saline aquifers. *International Journal of Greenhouse Gas Control, 14*, 84-96.

Vorren, T. O., Richardsen, G., Knutsen, S.-M., & Henriksen, E. (1991). Cenozoic erosion and sedimentation in the western Barents Sea. *Marine and Petroleum Geology, 8*(3), 317-340.

Warren, J., & Root, P. J. (1963). The behavior of naturally fractured reservoirs.

Worsley, D. (2008). The post-Caledonian development of Svalbard and the western Barents Sea. *Polar Research, 27*(3), 298-317.

Zahasky, C., & Benson, S. M. (2014). A simple approximate semi-analytical solution for estimating leakage of carbon dioxide through faults. *Energy Procedia, 63*, 4861-4874.

Zou, C. (2017). *Unconventional petroleum geology*: Elsevier.

Appendix A

Zahasky et al. (2014) derived a semi-analytical model for estimating the leakage of carbon dioxide through faults. Their derivation of the leak off equation is found below. All parameters used in Appendix A are listed in **Table A-0-1** at the end of the chapter.

The derivation begins by combining Darcy's Law (Equation 1) with the general pressure equation (Equation 2) to solve for flow rate in both linear (Equation 3) and radial (Equation 4) flow cases. The flow potential (Φ) is used to account for both the pressure due to injection and gravity (Equation 5). Equation 5 assumes a constant fluid density and an incompressible system.

$$\bar{u} = \frac{-\rho k}{\mu} \cdot \nabla \Phi \tag{1}$$

$$\nabla \cdot (k \nabla \rho \Phi) = 0 \tag{2}$$

$$q_l = \frac{-kwh\rho\Delta\Phi}{\mu l} \tag{3}$$

$$q_{rad} = \frac{-2\pi k h \rho}{\mu} \frac{\Phi_a - \Phi_b}{\ln(r_a / r_b)} \tag{4}$$

$$\Phi = \frac{p}{\rho} + gz \tag{5}$$

By using the linear (Equation 3) and radial (Equation 4) flow equations it is possible to quantify the flow rate for the reservoir (q_r – Equation 6), the flow rate through the fault (q_f – Equation 7) and the flow rate in the overlying aquifer (q_a – Equation 8).

$$q_r = \frac{2\pi k_r h_r \rho}{\mu} \frac{\Phi_a - \Phi_b}{\ln(r_{br} / r_a)} \tag{6}$$

$$q_f = \frac{-k_{fz} f_w f_l \rho}{\mu h_c} (\Phi_a - \Phi_f) \tag{7}$$

$$q_a = \frac{2\pi k_a h_a \rho}{\mu} \frac{\Phi_f - \Phi_b}{\ln((r_{ba} - r_a) / r_f)} \tag{8}$$

The schematic sketch given in **Figure A-0-1**is showing the pressures from fluid injection in the reservoir. The flow potential at the top of the faults is given by Φ_f, the flow potential at the base of the fault is given

by Φ_a and the pressure boundary where there is no pressure build up is given by p_b. The radius of influence in the aquifer is r_{ba} and the radius of influence of the pressure response due to injection in the reservoir is r_{br}. The extent of the pressure response can be estimated using the Theis solution (Equation 9) in an infinite acting reservoir and will be different in the reservoir and aquifer if the permeability values are different.

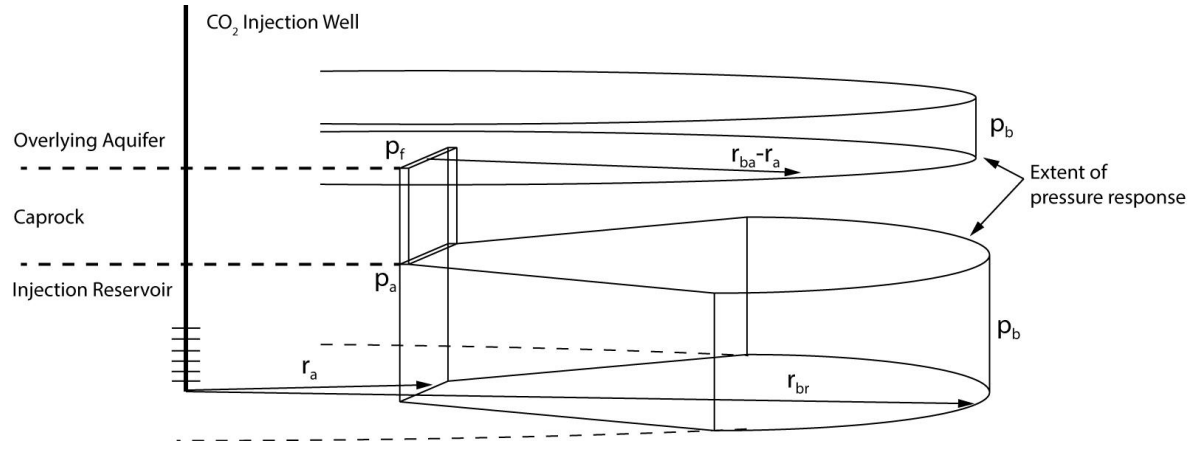

Figure A-0-1 Schematic sketch of pressure in the reservoir and overlying aquifer when the two units are hydraulically connected with a fault. From (Zahasky et al., 2014)

$$p_b = p_i + \frac{q\mu}{4\pi k_r h_r} W(u) \tag{9}$$

Equation 10 shows an approximation of the well function W(u) from the Theis solution.

$$W(u) = -0.5772 - \ln\left(\frac{\phi\mu c_t r_b^2}{4k_r t}\right) \tag{10}$$

By setting the well function equal to zero and solving for r_{br} an approximation for the radius of influence can be found (Equation 11). By replacing the reservoir permeability (k_r) with the aquifer permeability (k_a) the radius of influence in the aquifer (r_{ba}) is found.

$$r_{br} \approx \sqrt{\frac{2k_r t}{\phi\mu c_t}} \tag{11}$$

Three key assumptions are made in order to solve for flow in series in the fault and aquifer. First, the sum of the flow potential difference between the bottom of the fault Φ_a and the top of the fault Φ_f and the top of the fault and the system boundary Φ_b is equal to the difference between the bottom of the fault and the system boundary in the aquifer (Equation 12). This implies that the system has reached steady state, valid

after a long period of constant injection and nearly constant CO_2 leakage into the aquifer. Second, the flow rate into the aquifer is equal to the flow rate through the fault (Equation 13). This assumes that the rock in the fault and the fluid is incompressible. Third, a fault area balance equation gives the radius of the fault (r_f). The radius of the fault is determined such that the area of the circle defined by r_f is equal to the product of the fault width and the fault length (Equation 14 and Equation 15). This implies radial flow in the aquifer and is valid when the fault length is small relative to the size of the leakage plume in the overlaying aquifer.

$$(\Phi_a - \Phi_b) = (\Phi_a - \Phi_f) + (\Phi_f - \Phi_b) \tag{12}$$

$$q_f = q_a \tag{13}$$

$$\pi r_f^2 = f_w f_L \tag{14}$$

$$r_f = \sqrt{\frac{f_w f_L}{\pi}} \tag{15}$$

The fault and aquifer flow equations can be solved for flow potentials and combined into Equation 12.

$$(\Phi_a - \Phi_b) = \frac{q_a \mu h_c}{k_{fz} f_w f_l \rho} + \frac{q_a \mu}{2\pi k_a h_a \rho} \ln((r_{ba} - r_a)/r_f) \tag{16}$$

Further, the reservoir flow rate (Equation 6) is solved for flow potential and combined with Equation 16.

$$\frac{q_r \mu}{2\pi k_r h_r \rho} \ln(r_{br}/r_a) = \frac{q_a \mu h_c}{k_{fz} f_w f_l \rho} + \frac{q_a \mu}{2\pi k_a h_a \rho} \ln((r_{ba} - r_a)/r_f) \tag{17}$$

Next, solving for q_a and cancelling out the density and viscosity gives Equation 18.

$$q_a = \frac{q_r}{2\pi k_r h_r} \ln(r_{br}/r_a) \Bigg/ \left(\frac{h_c}{k_{fz} f_w f_l} + \frac{\ln((r_{ba} - r_a)/r_f)}{2\pi k_a h_a} \right) \tag{18}$$

The expression for the leakage fraction (L) is given by Equation 19.

$$L = \frac{q_a}{q_a + q_r} \tag{19}$$

Table A-0-1 Parameters included in the schematic sketch (**Figure A-0-1**) and equation 1-19 in **Appendix A**

q_a	flow rate into the aquifer (m/s)	k_a	permeability of the overlaying aquifer (m2)
q_r	flow rate of the injected fluid (m/s)	L	leak off fraction
h_r	height of the reservoir (m)	p_a	pressure at base of fault (Pa)
k_r	permeability in the reservoir (m^2)	p_f	pressure at the top of the fault (Pa)
r_{br}	extend of pressure response in reservoir (m)	p_b	pressure at model boundary (Pa
r_{ba}	extent of pressure response in aquifer (m)	Φ_b	flow potential at the system boundary (m^2/s^2)
r_a	fault distance for injection well (m)	Φ_f	flow potential at the top of the fault (m^2/s^2)
r_f	equivalent radius to fault (m)	Φ_a	flow potential at the bottom of the fault (m^2/s^2)
h_c	thickness of the cap rock (m)	c_t	compressibility factor (Pa^{-1})
k_{fz}	permeability in the fault zone (m2)	μ	viscosity (Pas)
f_w	fault width (m)	ϕ	porosity (-)
f_l	fault length (m)	ρ	fluid density (kg/m^3)
h_a	thickness of the overlaying aquifer (m2)	g	gravity (m/s^2)

Appendix B

Table B-1 Trip gas composition readings from **Figure 6-1**

Measured depth (m)	Total gas (%)	Methane C1 (ppm)	Ethane C2 ppm	Wetness (C1+C2)/C2
1005.00	0.40	46500	2500	19.60
1007.50	0.60	46500	2500	19.60
1010.00	1.40	51000	3000	18.00
1012.50	1.00	51000	3000	18.00
1015.00	0.80	51000	3000	18.00
1017.50	1.60	51500	3000	18.17
1020.00	0.90	51500	3000	18.17
1022.50	0.60	51000	3000	18.00
1025.00	0.50	51500	2700	20.07

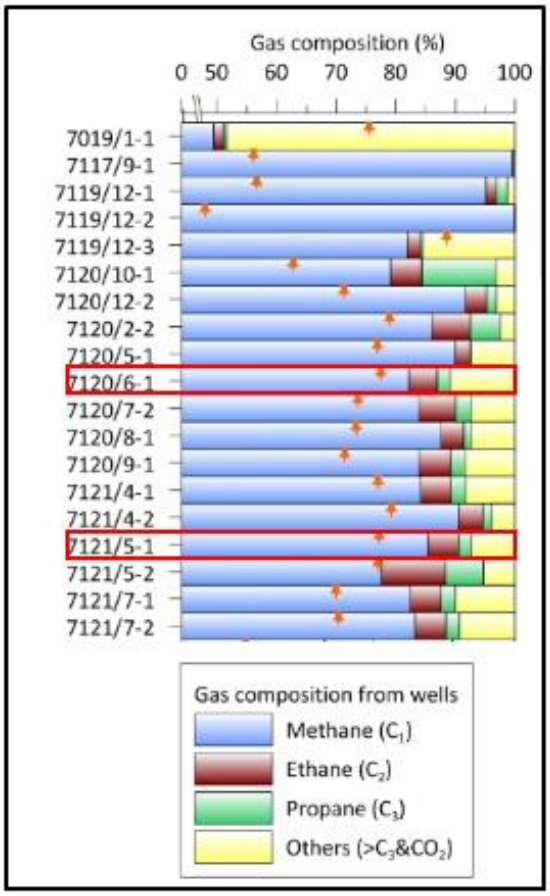

Figure B-0-1 Gas composition of some wells in the SW Barents Sea, well 7121/6-1 and 7121/5-1 marked in red rectangle.